Advances in Meteorology

Hydrometeorological Hazards: Monitoring, Forecasting, Risk Assessment, and Socioeconomic Responses

Guest Editors: Huan Wu, Maoyi Huang, Qiuhong Tang, Dalia B. Kirschbaum, and Philip Ward

Hydrometeorological Hazards: Monitoring, Forecasting, Risk Assessment, and Socioeconomic Responses

Advances in Meteorology

Hydrometeorological Hazards: Monitoring, Forecasting, Risk Assessment, and Socioeconomic Responses

Guest Editors: Huan Wu, Maoyi Huang, Qiuhong Tang, Dalia B. Kirschbaum, and Philip Ward

Editorial Board

Contents

Hindawi Publishing Corporation
Advances in Meteorology
Volume 2016, Article ID 2367939, 3 pages
http://dx.doi.org/10.1155/2016/2367939

Editorial

Hydrometeorological Hazards: Monitoring, Forecasting, Risk Assessment, and Socioeconomic Responses

Huan Wu,[1,2] Maoyi Huang,[3] Qiuhong Tang,[4] Dalia B. Kirschbaum,[2] and Philip Ward[5]

[1] *University of Maryland, College Park, MD, USA*
[2] *NASA Goddard Space Flight Center, Greenbelt, MD, USA*
[3] *Pacific Northwest National Laboratory, Richland, WA, USA*
[4] *Key Laboratory of Water Cycle and Related Land Surface Processes, Institute of Geographic Sciences and Natural Resources Research, Chinese Academy of Sciences, Beijing, China*
[5] *Vrije Universiteit, Amsterdam, Netherlands*

Correspondence should be addressed to Huan Wu; huanwu@umd.edu

Received 1 August 2016; Accepted 1 August 2016

Hydrometeorological hazards are caused by extreme meteorological and climate events, such as floods, droughts, hurricanes, tornadoes, or landslides. They account for a dominant fraction of natural hazards and occur in all regions of the world, although the frequency and intensity of certain hazards and society's vulnerability to them differ between regions. Severe storms, strong winds, floods, and droughts develop at different spatial and temporal scales, but all can become disasters that cause significant infrastructure damage and claim hundreds of thousands of lives annually worldwide. Oftentimes, multiple hazards can occur simultaneously or trigger cascading impacts from one extreme weather event. For example, in addition to causing injuries, deaths, and material damage, a tropical storm can also result in flooding and mudslides, which can disrupt water purification and sewage disposal systems, cause overflow of toxic wastes, and increase propagation of mosquito-borne diseases.

Particularly, floods and landslides caused more than 55% (2,000) of a total of 3,600 significant natural disasters worldwide during 2002–2011 [1], killing over 65,000 people and affecting over 1.1 billion people with an estimated cost of $280 billion (US dollars in 2011). The risks of flooding to population and infrastructure are continuing to increase due to the acceleration of the global water cycle [2] and rapid population growth. At the same time, populations and economic activities in floodplains around the world are growing rapidly, leading to a rapid increase in our socioeconomic exposure to floods [3, 4]. Monitoring and forecasting of the occurrence, intensity, and evolution of hydrometeorological extreme events have been critical components for a variety of humanitarian and government agencies in their efforts to prepare, mitigate, and manage responses to disaster, aiming at saving lives and limiting damage. Satellite remote sensing offers new opportunities to pursue flood estimation from regional to global scales, providing information of changes in surface water dynamics through direct observations using optical (e.g., [5, 6]) or Synthetic Aperture Radar (SAR) imagery (e.g., [7, 8]) and hydrological modeling with remote sensed information inputs such as precipitation, land cover, vegetation, topography, and hydrography (e.g., [9–11]). However, one of the major challenges faced by the flood community is the lack of ground truth data for validating or quantifying the uncertainty of historic and ongoing flooding events estimated by existing flood monitoring and forecasting systems, for example, the Dartmouth Flood Observatory (DFO, http://floodobservatory.colorado.edu/, [5]), NASA Near Real Time Global MODIS Flood Mapping (http://oas.gsfc.nasa.gov/floodmap/), the Global Flood Monitoring System (GFMS, http://flood.umd.edu/, [10, 11]), and Global Flood Awareness System (GloFAS, http://www.global-floods.eu/, [12]).

As a direct example, Figure 1 shows an example of how satellite precipitation can be used to drive a global hydrological model in terms of providing timely and relatively

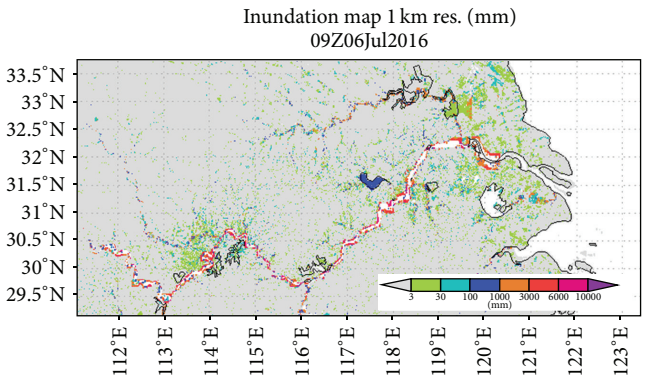

Figure 1: The GFMS calculated inundation map at 1 km resolution for the Yangtze River basin on July 6, 2016. More inundation maps and other data are available at http://flood.umd.edu/.

detailed flood information at 1 km resolution. Figure 1 shows results of the Global Flood Monitoring System (GFMS) for a widespread flooding situation that occurred in south China in July 2016. However, validation of such real time numerical model calculated flood information is challenging because of the availability of ground-based information. The comparison and integration of both model and remote sensing based flood information is vital to enhancing of the value of the flood information for better application by various users.

The papers collected in this special issue cover a wide range of research topics related to floods and landslides and shed light on some of recent progresses and ongoing researches in the field. In this special issue, G. J.-P. Schumann and K. M. Andreadis presented a method to infer the impact of a better Digital Elevation Model (DEM) on the prediction of flood risk over the Lower Zambezi basin in terms of the DEM's contribution to the overall accuracy of flood prediction. Their results highlight the notion that having higher resolution measurements would improve large-scale flood inundation prediction capabilities in the Lower Zambezi by at least 30% and significantly reduce the number of people affected as well as the economic loss associated with high magnitude flooding. The procedure developed by them is straightforward and has the potential to be applied to other regions where high quality topographic and hydrodynamic data are currently unavailable as in many cases of GFMS.

Remote controlled boats equipped with an Acoustic Doppler Current Profiler (ADCP) can be extremely valuable for obtaining flood information, for example, water discharge and velocity profile for ongoing flood events, as an important complementary tool to satellite and air based sensors. They have advantages of high productivity, fast measurements, operator safety, and high accuracy. J. Lee et al. developed the methods for better controlling and operating a remote boat in the rapid flow condition during flood events and successfully achieved high accuracy discharge measurement through the distance made good (DMG) modification of the boat path.

A reliable historic flood event archive will have great value in many cases for both science and applications, and therefore it is on the top of the wish list of many hydrologists, along with accurate DEM and precipitation datasets. W. T. L. Chow et al. developed a multimethod approach combining station precipitation data with archival newspaper and governmental records into a comprehensive local flood inventory, in which changes in flash floods frequencies and reported impacts of floods towards Singapore society were well documented. W. T. L. Chow et al. assessed that Singapore has relatively lower vulnerability to floods than other regional cities due to consistent and successful infrastructural development, widespread flood monitoring, and effective advisory platforms. However, the flood inventory they created indicated significant increases in reported flash flood frequency occurred in contemporary (post-2000) relative to historic (1984–1999) periods and storms in recent years are more intense and frequent, which indicates a future with increasing vulnerabilities. Such flood inventory not only formed the fundamental database for investigation of flooding patterns in Singapore, but also can be a local reference or complementary for the global flood inventory compiled by DFO which has showed great values in global flood model validation [10, 11] and other applications. To demonstrate and assess the new features and trends of flood risk in urbanized areas, it is also important to reasonably define the flood threshold with consideration of damage. C. Li et al. proposed S-shaped function of return period and damage which is tested in the Taihu River basin and can be utilized for timely and effective flood damage assessment and prediction. Several global scale flood risk models are now also available for assessing the impacts of floods on people and societies (e.g., [3, 13–18]), and they also have the same needs of high quality data for model validation [19].

Y. Park et al. proposed an urban landslide vulnerability assessment methodology considering urban social and economic aspects, based on the landslide susceptibility maps that the Korean Forest Service utilizes to identify landslide source areas. The physical and socioeconomic vulnerability levels analysis for Seoul, Korea, using the method indicates that the higher population density areas located downstream of mountainous areas tend to be more vulnerable than the areas in opposite conditions.

This special issue does not feign to address all challenges in monitoring and modeling of hydrometeorological hazards, however. Rather, we hope it serves as valuable asset for the physical and social scientists who work on topics related to hydrometeorological hazards in finding means to integrate modeling and remote sensing approaches that are complementary to each other for providing accurate forecasts, issuing timely warnings, monitoring ongoing hazards, reducing vulnerabilities, and building resilience for future.

Acknowledgments

We thank all the authors who contributed to this issue and all the reviewers who provide valuable, constructive comments

to the manuscripts and help to improve the quality of these papers published in this issue.

Huan Wu
Maoyi Huang
Qiuhong Tang
Dalia B. Kirschbaum
Philip Ward

References

[1] World Disasters Report, *International Federation of Red Cross and Red Crescent Societies*, 2012.

[2] P. J. Webster, G. J. Holland, J. A. Curry, and H.-R. Chang, "Changes in tropical cyclone number, duration, and intensity in a warming environment," *Science*, vol. 309, no. 5742, pp. 1844–1846, 2005.

[3] Y. Hirabayashi, R. Mahendran, S. Koirala et al., "Global flood risk under climate change," *Nature Climate Change*, vol. 3, no. 9, pp. 816–821, 2013.

[4] H. C. Winsemius, J. Aerts, L. van Beek et al., "Global drivers of future river flood risk," *Nature Climate Change*, vol. 6, no. 4, pp. 381–385, 2015.

[5] R. Brakenridge and E. Anderson, "MODIS-based flood detection, mapping and measurement: the potential for operational hydrological applications," in *Transboundary Floods: Reducing Risks Through Flood Management*, J. Marsalek, G. Stancalie, and G. Balint, Eds., vol. 72 of *Nato Science Series: IV: Earth and Environmental Sciences*, pp. 1–12, Springer, New York, NY, USA, 2006.

[6] C. Ordoyne and M. A. Friedl, "Using MODIS data to characterize seasonal inundation patterns in the Florida Everglades," *Remote Sensing of Environment*, vol. 112, no. 11, pp. 4107–4119, 2008.

[7] M. S. Horritt, D. C. Mason, D. M. Cobby, I. J. Davenport, and P. D. Bates, "Waterline mapping in flooded vegetation from airborne SAR imagery," *Remote Sensing of Environment*, vol. 85, no. 3, pp. 271–281, 2003.

[8] D. C. Mason, I. J. Davenport, J. C. Neal, G. J.-P. Schumann, and P. D. Bates, "Near real-time flood detection in urban and rural areas using high-resolution synthetic aperture radar images," *IEEE Transactions on Geoscience and Remote Sensing*, vol. 50, no. 8, pp. 3041–3052, 2012.

[9] M. S. Shrestha, G. A. Artan, S. R. Bajracharya, and R. R. Sharma, "Using satellite-based rainfall estimates for streamflow modelling: Bagmati Basin," *Journal of Flood Risk Management*, vol. 1, no. 2, pp. 89–99, 2008.

[10] H. Wu, R. F. Adler, Y. Hong, Y. Tian, and F. Policelli, "Evaluation of global flood detection using satellite-based rainfall and a hydrologic model," *Journal of Hydrometeorology*, vol. 13, no. 4, pp. 1268–1284, 2012.

[11] H. Wu, R. F. Adler, Y. Tian, G. J. Huffman, H. Li, and J. Wang, "Real-time global flood estimation using satellite-based precipitation and a coupled land surface and routing model," *Water Resources Research*, vol. 50, no. 3, pp. 2693–2717, 2014.

[12] L. Alfieri, P. Burek, E. Dutra et al., "GloFAS—global ensemble streamflow forecasting and flood early warning," *Hydrology and Earth System Sciences*, vol. 17, no. 3, pp. 1161–1175, 2013.

[13] N. W. Arnell and S. N. Gosling, "The impacts of climate change on river flood risk at the global scale," *Climatic Change*, vol. 134, no. 3, pp. 387–401, 2016.

[14] CIMA Foundation, *Improvement of the Global Flood Model for the GAR15. Background Paper prepared for the 2015 Global Assessment Report on Disaster Risk Reduction*, UNISDR, Geneva, Switzerland, 2015.

[15] F. Dottori, P. Salamon, A. Bianchi, L. Alfieri, F. A. Hirpa, and L. Feyen, "Development and evaluation of a framework for global flood hazard mapping," *Advances in Water Resources*, vol. 94, pp. 87–102, 2016.

[16] C. C. Sampson, A. M. Smith, P. B. Bates, J. C. Neal, L. Alfieri, and J. E. Freer, "A high-resolution global flood hazard model," *Water Resources Research*, vol. 51, no. 9, pp. 7358–7381, 2015.

[17] P. J. Ward, B. Jongman, F. S. Weiland et al., "Assessing flood risk at the global scale: model setup, results, and sensitivity," *Environmental Research Letters*, vol. 8, no. 4, Article ID 044019, 2013.

[18] H. C. Winsemius, L. P. H. Van Beek, B. Jongman, P. J. Ward, and A. Bouwman, "A framework for global river flood risk assessments," *Hydrology and Earth System Sciences*, vol. 17, no. 5, pp. 1871–1892, 2013.

[19] P. J. Ward, B. Jongman, P. Salamon et al., "Usefulness and limitations of global flood risk models," *Nature Climate Change*, vol. 5, no. 8, pp. 712–715, 2015.

Hindawi Publishing Corporation
Advances in Meteorology
Volume 2016, Article ID 4572498, 13 pages
http://dx.doi.org/10.1155/2016/4572498

Research Article

Development and Application of Urban Landslide Vulnerability Assessment Methodology Reflecting Social and Economic Variables

Yoonkyung Park,[1] Ananta Man Singh Pradhan,[2] Ungtae Kim,[3] Yun-Tae Kim,[2] and Sangdan Kim[4]

[1]*Division of Earth Environmental System Science, Pukyong National University, 45 Yongso-ro, Nam-gu, Busan 48513, Republic of Korea*
[2]*Department of Ocean Engineering, Pukyong National University, 45 Yongso-ro, Nam-gu, Busan 48513, Republic of Korea*
[3]*Civil and Environmental Engineering, Cleveland State University, Cleveland, OH 44115, USA*
[4]*Department of Environmental Engineering, Pukyong National University, 45 Yongso-ro, Nam-gu, Busan 48513, Republic of Korea*

Correspondence should be addressed to Sangdan Kim; skim@pknu.ac.kr

Received 23 December 2015; Revised 29 March 2016; Accepted 7 June 2016

Academic Editor: Philip Ward

An urban landslide vulnerability assessment methodology is proposed with major focus on considering urban social and economic aspects. The proposed methodology was developed based on the landslide susceptibility maps that Korean Forest Service utilizes to identify landslide source areas. Frist, debris flows are propagated to urban areas from such source areas by Flow-R (flow path assessment of gravitational hazards at a regional scale), and then urban vulnerability is assessed by two categories: physical and socioeconomic aspect. The physical vulnerability is related to buildings that can be impacted by a landslide event. This study considered two popular building structure types, reinforced-concrete frame and nonreinforced-concrete frame, to assess the physical vulnerability. The socioeconomic vulnerability is considered a function of the resistant levels of the vulnerable people, trigger factor of secondary damage, and preparedness level of the local government. An index-based model is developed to evaluate the life and indirect damage under landslide as well as the resilience ability against disasters. To illustrate the validity of the proposed methodology, physical and socioeconomic vulnerability levels are analyzed for Seoul, Korea, using the suggested approach. The general trend found in this study indicates that the higher population density areas under a weaker fiscal condition that are located at the downstream of mountainous areas are more vulnerable than the areas in opposite conditions.

1. Introduction

In South Korea, there has been continuous interest in reducing landslide or debris flow damage because about 70% of the Korean territory is covered with mountainous areas. Many researchers have analyzed the factors causing landslides [1, 2]. Landslide susceptibility maps have been built on the mainland across South Korea by Korea Forest Service (KFS) and have been used as the basis for the studies to predict landslides or reduce the damage. The resolution of KFS landslide susceptibility maps is 10 m by 10 m, and the maps are classified into 5 grades according to the probability of landslides. Since the maps were developed to limit the mountain areas, the impacts of landslides on the downstream side are not reflected or evaluated. The Mt. Umyeon landslide that occurred in Seoul, South Korea, in July 2011 suggested that the impact of mountain landslides on the downstream city should be considered in the landslide and debris flow information system. From the lessons of Mt. Umyeon landslide, this study was planned to evaluate the landslide vulnerability to reflect the impact on the urban areas under the mountains.

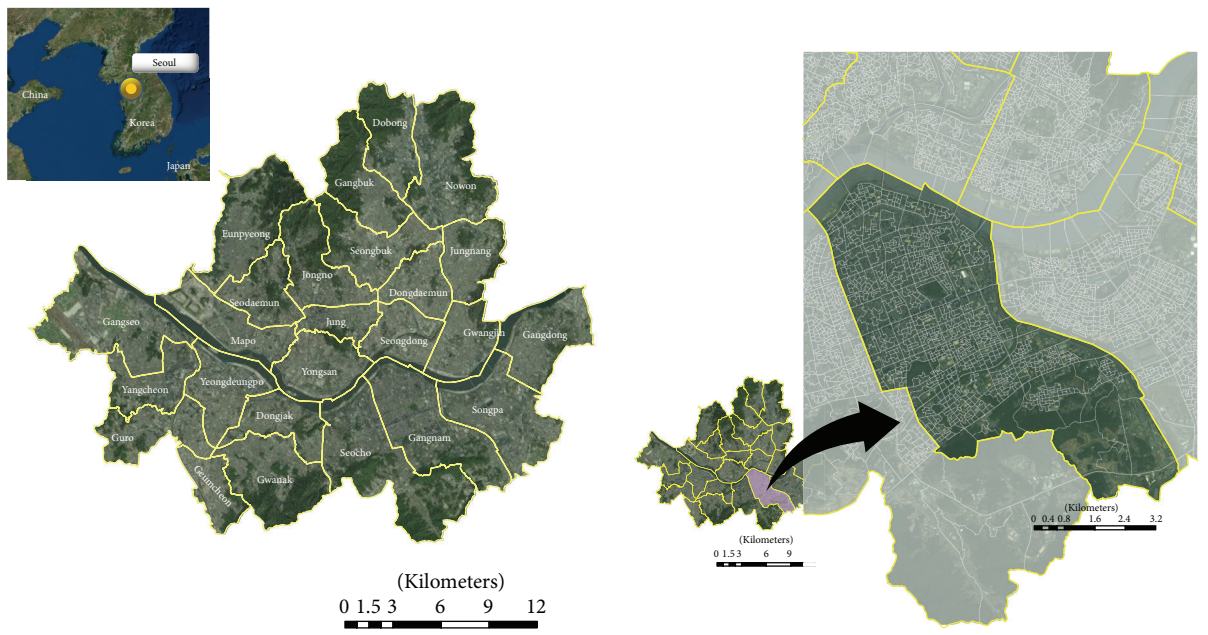

(a) Boroughs in Seoul

(b) Census output area of Gangnam in Seoul

Figure 1: Study area, Seoul, South Korea, with Census Output Area.

In view of this, the damage type classification proposed by Smith and Ward [3] provides important insights in the vulnerability assessment framework configuration. They classified the types of damage from natural disasters into direct and indirect damage. Representative examples of the direct damage is the damage of life and property. On the other hand, examples of the indirect damage can be the intangible damage caused by traffic disruptions. In order to evaluate properly the urban vulnerability to natural disasters, various types of damage should be reflected in the vulnerability assessment framework [4].

Although many studies have evaluated the damage of buildings due to a landslide [5–7], studies evaluating the damage of life or secondary damage are not sufficient to provide a guideline. In recent years, however, some studies on the socioeconomic vulnerability assessment considering the damage of life or secondary damage have been attempted [8–11]. Those studies mainly focused on evaluating the vulnerability in terms of sensitivity to natural disasters and ability to respond to them.

In this study, a combined methodology for evaluating the urban physical and socioeconomic vulnerability to landslides is proposed. Urban landslide vulnerability is assessed by two categories; physical and socioeconomic aspect. The damage of buildings by landslides is considered to be a proxy variable representing the physical vulnerability. On the other hand, the socioeconomic vulnerability is evaluated using a number of proxy variables that can explain the exposure degree of vulnerable people in landslide disasters, factors causing a variety of secondary damage, and disaster preparedness of local governments.

2. Study Area and Scale

The study area is Seoul, the capital of South Korea, which has a complicated socioeconomic infrastructure and a high population density. In countries most of the critical national infrastructure is highly concentrated in one single city (such as South Korea), and the vulnerability evaluation methods applied to many cities by previous studies are not suitable to the current study area. In order to properly evaluate the vulnerability of a large metropolitan area, it should be evaluated in much higher spatial resolution.

Korea National Statistical Office (KNSO) has set up "Census Output Area (COA)" as a minimal spatial scale to publish national standard statistical data in South Korea [12]. The size is determined by the amount of people and the social homogeneity resulting in an average population size of about 500 people per COA. Therefore the COA level was considered the basic mapping unit for the vulnerability assessment in this study. Seoul is composed of 16,230 COAs. The area of COAs ranges from 0.00012 km^2 to 10.10 km^2 (average 0.037 km^2). Figure 1 shows the locations of Seoul with 25 boroughs and COAs constituting the Gangnam region in the boroughs. Other boroughs also show similar COA distribution to Gangnam.

3. Urban Landslide Vulnerability Assessment

The proposed urban landslide vulnerability assessment process consists of three steps. The first step is to identify potential landslide hazard areas, which can be carried out by combining landslide susceptibility maps and Flow-R model [13]. The second step is to assess separately physical and

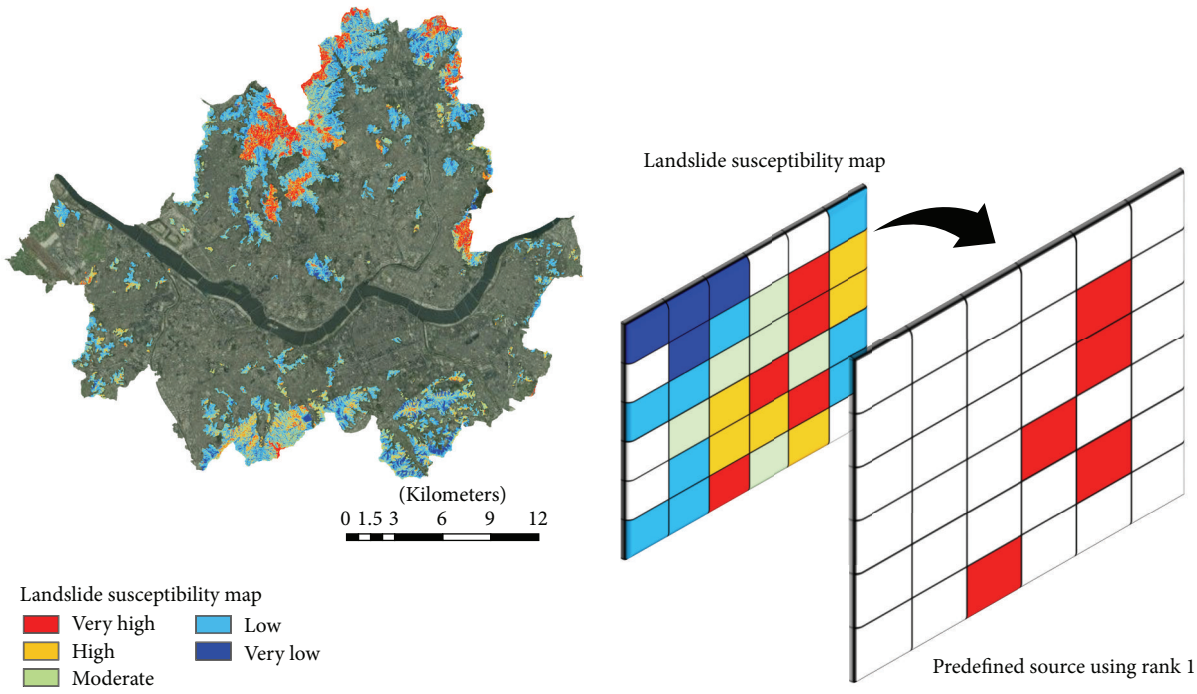

Figure 2: Identification of predefined source areas using landslide susceptibility map.

socioeconomic vulnerability based on identified potential landslide susceptibility areas. As a final step, the urban landslide vulnerability is generated by combining physical and socioeconomic vulnerability.

3.1. Potential Landslide Areas Identification. Vulnerability assessment under landslide disaster requires information on the propagation extent and intensity by debris flows. Such information on debris flow susceptibility mapping can be obtained by regional scale runout simulation. Since landslides are caused by various natural factors, landslide analysis in regional scale is difficult. Horton et al. [13] developed a distributed empirical model, Flow-R, for flow path assessment of gravitational hazards at a regional scale. The model is available free of charge at http://www.flow-r.org/. One advantage of this model is that the amount of data required for the simulation is small. A Digital Elevation Model (DEM) may be sufficient to identify potential landslide source areas and to process the propagation. Data such as slope, curvature, and flow accumulation are required for more accurate analysis.

This study applies Flow-R to obtain two landslide characteristics: spreading probability and impact pressure. DEM and predefined sources are used for Flow-R simulation. Predefined source is potential grids where landslide may occur. The predefined source used in this study is obtained by using landslide susceptibility maps. The maps developed by KFS are displayed by classifying the landslide probability to five ranks. Rank 1 areas in the maps have the highest probability of landslide occurrence.

In other words, landslide event is the most frequent in the area. This study is the first step in South Korea about urban landslide vulnerability. It is necessary to study the extreme cases. "Predefined source" is defined by rank 1 area in the map to apply extreme case (red grids in Figure 2). The resolution of DEM and predefined source areas is 10 m by 10 m.

Table 1: Selected landslide disaster algorithms of Flow-R.

Propagation routine	Applied method
Spreading algorithm	
Flow direction algorithm	Holmgren [14] modified
Persistence function	Inertial parameter
Friction law	Simplified friction-limited model

Flow-R provides a variety of algorithms to analyze debris flow. Table 1 shows the algorithms applied to analyze landslide disaster in this study. Spreading algorithms control the path and the spreading of debris flow. Friction law determines the runout distance. All algorithms in Flow-R are described in detail by Horton et al. [13]. The parameters for simulating Flow-R have to be calibrated and verified using actual data. But such data set is not provided in Seoul. So this study has no choice but to use the reference values from Horton et al. [13].

The result of Flow-R simulation is the total area that can be potentially propagated by debris flows with an associated susceptibility value and kinetic energy. The resolution of the output is the same as that of the input data. The susceptibility value is used to extract COAs which are influenced by landslide runout. Equation (1) is used to estimate the impact pressure (p, kPa) in each grid [15]:

$$\text{impact pressure } (p) = \frac{\sqrt{2E_{\text{kin}}}\rho_b}{1000}, \quad (1)$$

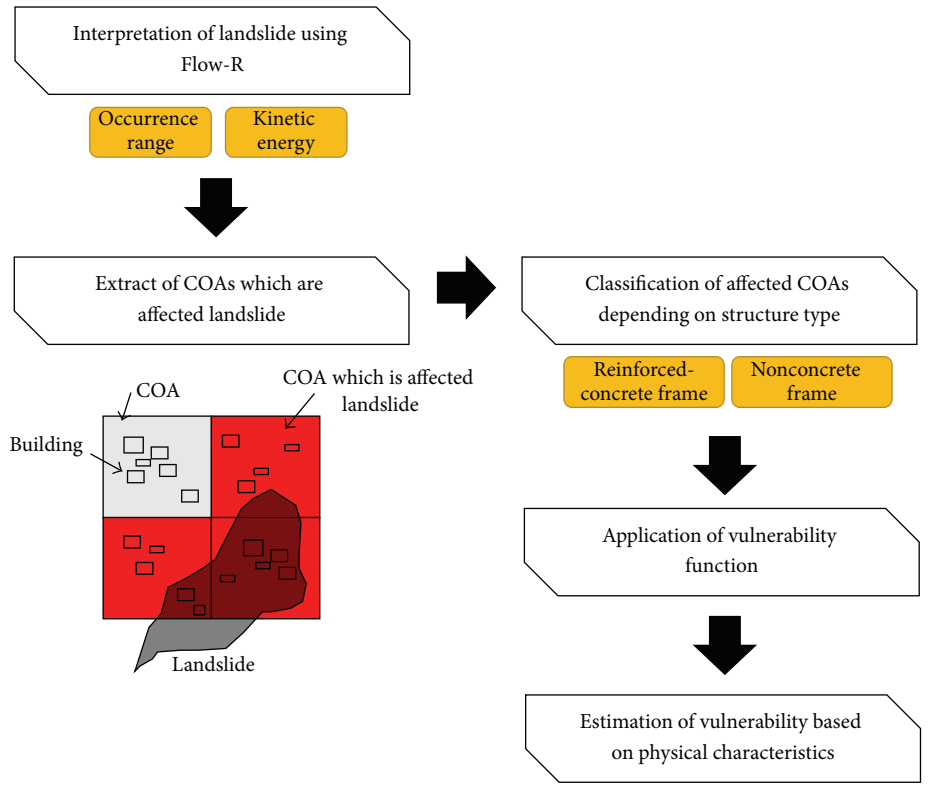

Figure 3: Procedure of physical vulnerability assessment.

where E_{kin} is the kinetic energy calculated by Flow-R internally and ρ_b is the bulk density of debris flow (2,239.17 kg/m^3 was used in this study). If the impact pressure of landslide exceeds about 34 kPa, houses built with bricks or woods would be destroyed completely [6].

3.2. Physical Landslide Vulnerability Assessment. When a landslide occurs, the physical characteristics such as velocity, depth, and impact pressure are determining the level of damage of buildings. Many studies have been conducted to find the relationship between physical characteristics and the damage of various structures [16–18]. These previous studies mainly focused on creating a vulnerability curve by correlating the relationship between landslide characteristics and the damage of buildings. Based on those findings, this study developed vulnerability curves for two different structure types in the study area, and then the curves were used to assess physical vulnerability. Figure 3 shows the procedure of the physical vulnerability assessment.

The first stage of the physical vulnerability assessment is to identify COAs affected by landslides using Flow-R simulations and to calculate the spatially averaged impact pressure in identified COAs. The second stage is to classify the buildings in an identified COA into two categories: non-reinforced concrete (non-RC) frame and reinforced-concrete (RC) frame. Finally, the physical vulnerability assessment is to calculate the physical vulnerability by linking the spatially averaged impact pressure in the identified COA and vulnerability curves.

Table 2: Vulnerability functions [6].

Frame type	Vulnerability function
Non-RC frame	$V = 1 - e^{-0.0010p^{2.227}}$
RC frame	$V = 1 - e^{-0.0005p^{1.690}}$

Note. V: physical vulnerability; p: impact pressure (kPa).

Two kinds of vulnerability curves, which have been developed by Kang and Kim [6], are applied in accordance with each of the two building structure types (Figure 4). The physical vulnerability therefore ranges from 0 (the lowest vulnerability) to 1 (the highest vulnerability) as shown in Table 2. The highest vulnerability (value equals 1) means buildings are broken down completely when landslide event happens.

3.3. Socioeconomic Vulnerability Assessment. Socioeconomic vulnerability aims to evaluate the social and economic factors that may be affected by landslides. Socioeconomic vulnerability should be evaluated by a variety of factors with various perspective. This can be carried out using an index-based model [8]. In this study, the modified version to match the conditions in Korea based on the socioeconomic vulnerability assessment framework of landslides developed

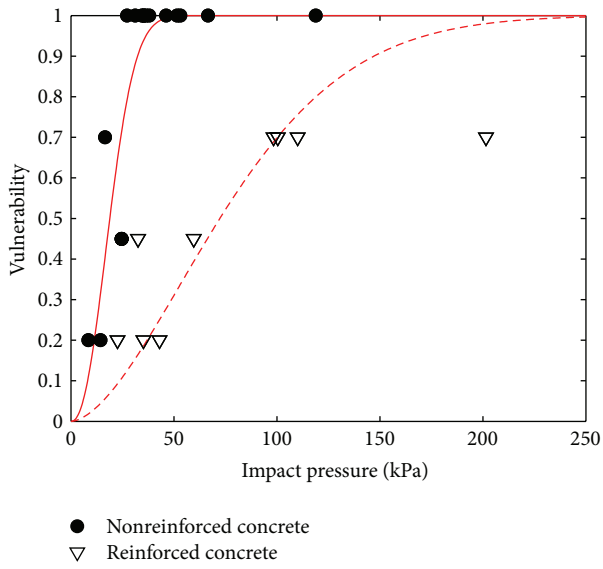

Figure 4: Vulnerability curves depending on impact pressure [6].

by Safeland [19] is proposed. The proposed model can evaluate demographic factors, economic factors, and landslide disaster preparedness and response capabilities. The potential proxy variables are identified as age distribution, population density, housing type, personal assets, risk perception, the presence of disaster warning system, and so on. Those variables are mainly selected by a literature review and expert interviews. The procedure of socioeconomic vulnerability assessment is shown in Figure 5.

The model is composed of a total of three subindexes: Demographic and Social Index (DSI), Secondary-Damage-Triggering Index (STI), and Preparation and Response Index (PRI). DSI is evaluated by six population-related and social variables that may be affected by natural disasters. For example, "age distribution" is classified into vulnerable people group. The children or elderly people are more vulnerable than young people. It is the reason to select "age distribution" as proxy variable in DSI (Table 4). "Population density" influences vulnerability. If landslide event happens in high population density area, it will caused heavy casualties. Therefore, "population density" can be used as proxy variable to assess socioeconomic vulnerability.

STI is an index to evaluate the indirect damage caused by natural disasters. For instance, when roads are malfunctioning, damage such as traffic jam and destruction of many life lines is caused [20]. Public office becomes control tower in emergency situation. Damage in public office causes secondary damage due to absence of control systems in emergency situation such as landslide event. For this reason, "the number of public offices" is selected as proxy variable of STI (Table 5).

PRI assesses the ability to prevent and respond to natural disasters. All used proxy variables and subindexes are listed in Table 3. Statistical data that used in this study are obtained from KOSIS (Korea Statistical Information Service). Statistics used in this study were compiled in 2010 as a base year,

Table 3: Proxy variables and their weights in socioeconomic vulnerability assessment model.

Social-economic vulnerability index	Weights
DSI (demographic and social index): 31%	
Age distribution	13.8%
Number of workers who may be exposed to disasters	26.4%
Population density	24.4%
Foreigner ratio	6.8%
Education level	9.4%
Housing type	19.2%
STI (secondary-damage-triggering index): 34%	
Number of public offices	14.7%
Road area ratio	25.8%
Number of electronic supply facilities	28.2%
School area ratio	11.4%
Commercial and industrial area ratio	19.9%
PRI (preparation and response index): 35%	
Disasters frequency	12.4%
Internet penetration rate	8.6%
Number of disaster prevention facilities	25.8%
Perceived safety	27.8%
Number of medical doctors	13.2%
Financial independence of the borough	12.2%

and the spatial resolution of the data is COA. However, the resolution of the proxy variables for PRI is a borough (Table 6). Application of PRI is suitable in borough scale because disaster response system of South Korea is the local government.

The structure of the socioeconomic vulnerability is modified to be suitable in South Korea using the result of them [21].

Tables 4, 5, and 6 show the suggested socioeconomic vulnerability assessment model with proposed proxy variables and criteria for ranking of the variables. These variables have been used in many previous researches (see citations in Tables 4, 5, and 6).

Finally, the socioeconomic vulnerability index is calculated by weighted average of quantified proxy variables ranks (using (2)). The weights are determined after extensive expert survey based on the analytic hierarchy process developed by Saaty [22, 23]. The weights can be found in Table 3. Consider

$$\text{Total vulnerability score value} = \frac{\sum \text{Weighted vulnerability score}}{\sum \text{Weight}}. \quad (2)$$

To assess the socioeconomic vulnerability to landslide disasters, exposure information of landslide should be combined. By applying the proposed methodology to the COAs identified from previous Flow-R simulation, the vulnerability is evaluated for each COA. The vulnerability of the COAs identified as nonaffected areas is assigned to be 0.

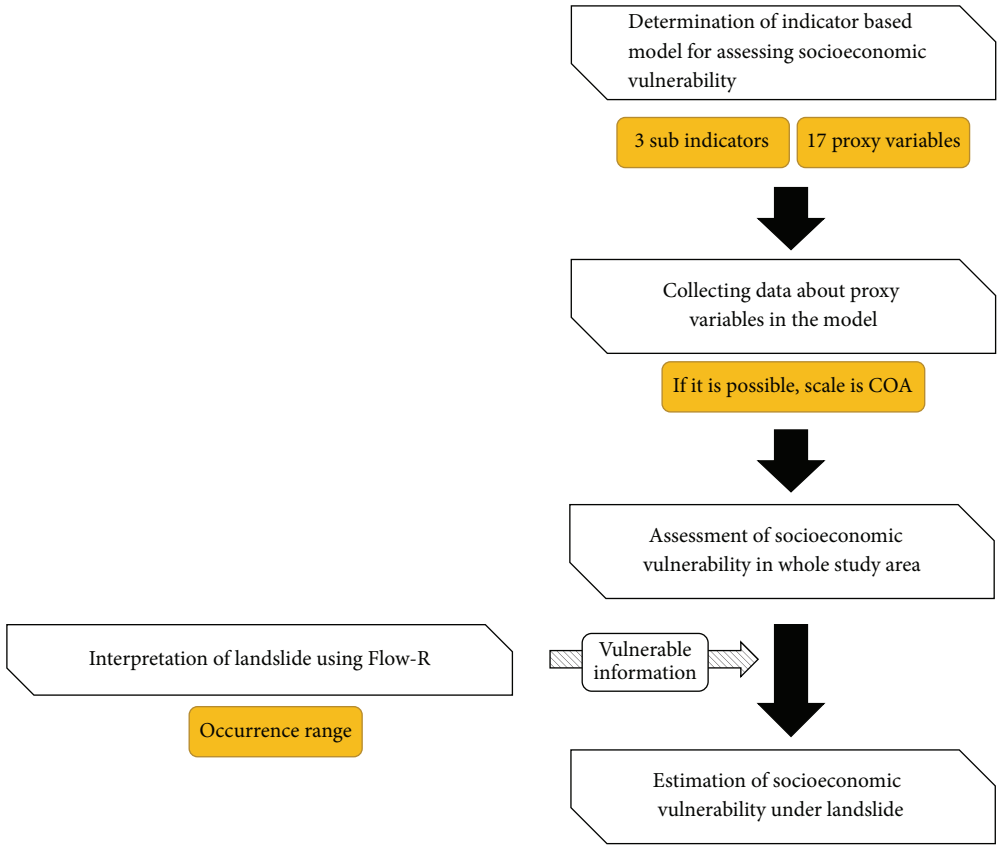

Figure 5: Procedure of socioeconomic vulnerability assessment.

4. Results and Discussion

4.1. Physical Vulnerability Assessment. Landslide affected COAs were identified by Flow-R simulation, and the corresponding impact pressure for each identified COA was estimated. Figure 6 shows the spatial distribution of identified landslide affected regions and the corresponding impact pressure. The impact pressure was not calculated for the COAs that are not affected by landslide disasters. The number of identified COAs is 2,249 and the maximum average impact pressure is estimated to be 37 kPa.

The physical vulnerability index is calculated by combining the impact pressure presented in Figure 6(b) and vulnerability functions (Table 2) developed by Kang and Kim [6]. In this study, two patterns of vulnerability functions were applied to two building structure types, non-RC and RC. It is noted that the average physical vulnerability is estimated to be 0.96 in the case that the impact pressure 37 kPa is applied to non-RC, while it is 0.20 for the RC case. Figure 7 shows the landslide physical vulnerability assessment map calculated by the proposed methodology.

If physical vulnerability in a certain COA is estimated to be 1, it means that the buildings in the area are completely destroyed when landslide event happens. Therefore, a high physical vulnerability range (e.g., from 0.841 to 0.960 in Figure 8) means that the buildings in the area are damaged severely by landslide event.

It can be observed that the COAs located below the mountainous areas with denser residential areas are more vulnerable to landslide disasters in physical aspect than the nonmountainous or less dense.

However, there are clear limitations to the use of the regional scale Flow-R model for obtaining quantitative output that can be used in combination with physical vulnerability curves. The Flow-R is an empirical model, which does not take into account source volume, entrainment, or rheology. In further research, a regional scale model that can calculate the volume of landslide should be applied [27, 28].

4.2. Socioeconomic Vulnerability Assessment. Socioeconomic vulnerability is evaluated by three detailed subindexes (Table 3) and the results of each vulnerability assessment are presented in Figure 8.

DSI is a vulnerability assessment subindex related to the population. In general, it can be seen that COAs where the population density is high are more vulnerable (Figure 8(a)). STI is a vulnerability assessment subindex related to the impact on other areas of the occurrence of a disaster event at a COA. In general, it can be seen that COAs including major urban areas are more vulnerable (Figure 8(b)). PRI is a vulnerable assessment subindex related to preparedness and ability to respond to disasters in a borough (Figure 8(c)). This vulnerability index is inversely proportional to the fiscal

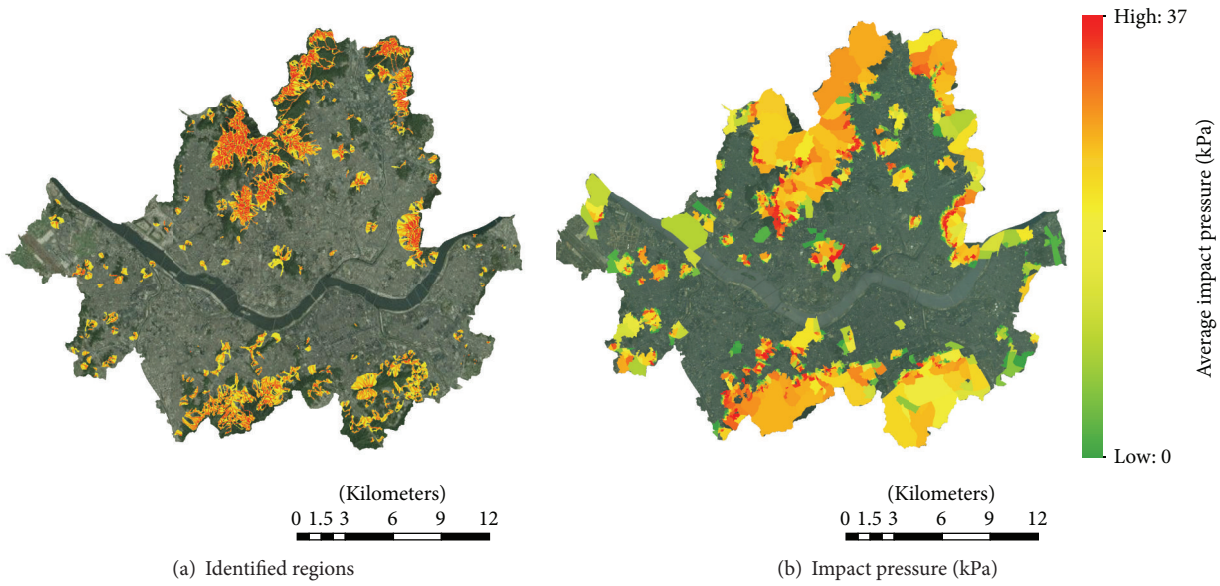

(a) Identified regions (b) Impact pressure (kPa)

Figure 6: Results of Flow-R simulation.

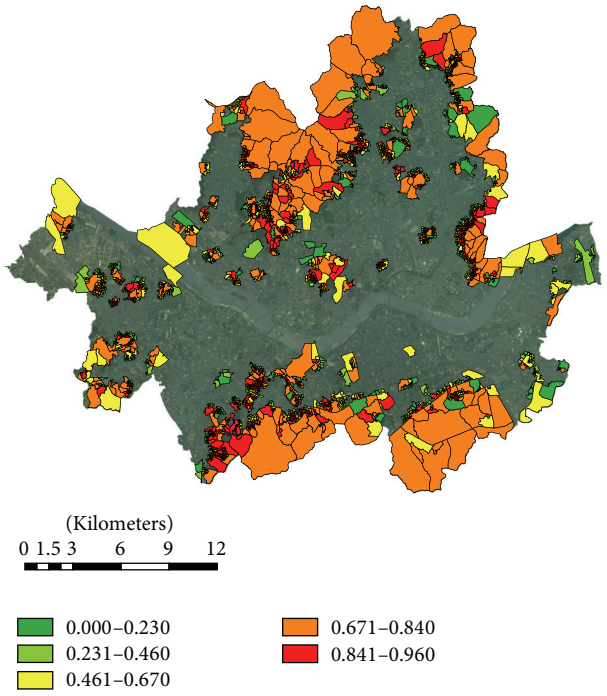

Figure 7: Physical vulnerability to landslide disaster.

health of local governments. Therefore, the boroughs in a weak fiscal condition (northwestern and southeastern regions of the study area, Seoul) are classified as a lack of preparedness and ability to respond to disasters. Socioeconomic vulnerability assessment calculated by the weighted average of three detailed subindexes is shown in Figure 8(d). Overall, the southern region in Seoul is more vulnerable against the disaster in a socioeconomic perspective. The results shown in Figure 8(d) assume that natural disasters have occurred uniformly throughout the whole study area, Seoul.

To evaluate the vulnerability to landslides specifically for COAs, Figures 8(d) and 6(a) should be combined. The combined landslide vulnerability assessment in a socioeconomic aspect is shown in Figure 9 as a result. It is suitable

Table 4: Criteria for ranking of proxy variables of DSI.

Proxy variable	Ranking criteria	
	Rank	Description
Age distribution [4, 11, 19, 20, 24]	1	Less than 20% of population is either between 0 and 4 years or over 65 years
	2	20–30% of population is either between 0 and 4 years or over 65 years
	3	30–40% of population is either between 0 and 4 years or over 65 years
	4	40–50% of population is either between 0 and 4 years or over 65 years
	5	Over 50% of population is either between 0 and 4 years or over 65 years
Number of workers who may be exposed to disasters [4, 19, 20, 24]	1	Less than 10 workers work in either agriculture, forestry, mining, transportation, or construction
	2	10–20% of workers work in either agriculture, forestry, mining, transportation, or construction
	3	20–30% of workers work in either agriculture, forestry, mining, transportation, or construction
	4	30–40% of workers work in either agriculture, forestry, mining, transportation, or construction
	5	Over 40% of workers work in either agriculture, forestry, mining, transportation, or construction
Population density [19, 20]	1	Population density is less than 100 people/km^2
	2	Population density is between 100 and 150 people/km^2
	3	Population density is between 150 and 300 people/km^2
	4	Population density is between 300 and 600 people/km^2
	5	Population density is over 600 people/km^2
Foreigner ratio [4, 19, 20]	1	Foreigner ratio is less than 1%
	2	Foreigner ratio is between 1 and 3%
	3	Foreigner ratio is between 3 and 4%
	4	Foreigner ratio is between 4 and 5%
	5	Foreigner ratio is over 5%
Education level [4, 19–21]	1	Over 30% of population have attended or are attending a postsecondary education
	2	20–30% of population have attended or are attending a postsecondary education
	3	10–20% of population have attended or are attending a postsecondary education
	4	5–10% of population have attended or are attending a postsecondary education
	5	Less than 5% of population have attended or are attending a postsecondary education
Housing type [19–21]	1	Over 45% of housing type is apartment
	2	40–45% of housing type is apartment
	3	35–40% of housing type is apartment
	4	30–35% of housing type is apartment
	5	Less than 30% of housing type is apartment

to apply quantitative characteristics of landslide events. But this study overlaid susceptibility map from Flow-R due to lack of quantitative data about landslide event. If the quantitative assessment is able to analyze landslide in regional scales [27, 28], more accurate socioeconomic vulnerability about landslide can be obtained.

The biggest difference between Figures 8(d) and 9 is observed in southwestern Seoul. In fact, the southwest area of Seoul is a very high likelihood of a flood disaster area. Therefore, although this region has higher vulnerability to common natural disasters, the region may not have high vulnerability to landslide.

4.3. Urban Landslide Vulnerability. Urban characteristics were reflected in vulnerability assessment under landslide disaster by combining physical and socioeconomic vulnerabilities. For the combination of the two vulnerability assessments, the physical vulnerability region (Figure 7) was multiplied by the socioeconomic vulnerability region (Figure 9) and the region values were normalized between 0 and 1 as one urban vulnerability to landslide. The urban vulnerability index can be classified into five categories as very low, low, moderate, high, and very high. The result of the integrated urban landslide vulnerability assessment is shown in Figure 10.

Table 5: Criteria for ranking of proxy variables of STI.

Proxy variable	Ranking criteria	
	Rank	Description
Number of public offices [4, 20, 25]	1	There are less than 5 public offices
	2	There are 5–10 public offices
	3	There are 10–15 public offices
	4	There are 15–20 public offices
	5	There are over 20 public offices
Road area ratio [20, 25]	1	Road area is less than 5%
	2	Road area is between 5 and 10%
	3	Road area is between 10 and 15%
	4	Road area is between 15 and 20%
	5	Road area is over 20%
Number of electronic supply facilities [11, 20, 25]	1	Less than 2 electronic supply facilities
	2	There are 2–4 electronic supply facilities
	3	There are 4–6 electronic supply facilities
	4	There are 6–8 electronic supply facilities
	5	There are over 8 electronic supply facilities
School area ratio [20]	1	School area is less than 5%
	2	School area is between 5 and 10%
	3	School area is between 10 and 15%
	4	School area is between 15 and 20%
	5	School area is over 20%
Commercial and industrial area ratio [4, 20]	1	Commercial and industrial area is less than 0.5%
	2	Commercial and industrial area is between 0.5–1%
	3	Commercial and industrial area is between 1 and 2%
	4	Commercial and industrial area is between 2 and 3%
	5	Commercial and industrial area is over 3%

Figure 10 indicates that 50% or more of COAs affected by landslides (Figure 7) have an urban vulnerability of less than 0.3 (urban vulnerability is very low or low). This means that these COAs are likely to be in a landslide damage but relatively less vulnerable. The size of these COAs varies ($0.00046\,km^2$–$7.52\,km^2$, average $0.11\,km^2$). On the other hand, the size of very vulnerable COAs where the urban vulnerability is at least 0.6 is small ($0.0047\,km^2$–$2.24\,km^2$, average $0.046\,km^2$). The size of a COA is mainly determined by the population and their socioeconomic homogeneity. When the size of a COA is very small, the COA has a very high population density and is highly urbanized. If landslides occurred in these COAs, the damage caused by the landslides would be amplified. Therefore, these COAs are extremely vulnerable to the landslide disaster, and disaster mitigation measures must be taken first in these priority areas.

5. Summary and Conclusion

For suitable vulnerability assessment of natural disasters including landslides, this study showed that both direct damage and indirect damage should be considered in the vulnerability assessment processes. In this study, vulnerability assessment for landslides among various natural disasters was conducted. In particular, the proposed methodology properly reflects the urban characteristics in terms of vulnerability to natural disasters. Therefore, the results of this study can be directly utilized for setting the priority of various landslide damage reduction projects in urban areas.

In the proposed methodology, the possible landslide source areas were first identified using existing landslide susceptibility maps. Flow-R simulation provided the extents and impact pressure of debris flow routed from the identified sources areas of landslide. The outcomes were served as landslide exposure information for physical and socioeconomic vulnerability assessment.

Direct damage due to landslide disasters was considered by physical vulnerability. Vulnerability functions quantifying the degree of damage of buildings were applied to evaluate the physical vulnerability. By applying vulnerability functions to building information and impact pressure of each affected COA, the physical vulnerability index was estimated.

Table 6: Criteria for ranking of proxy variables of PRI.

Proxy variable	Ranking criteria	
	Rank	Description
Disasters frequency [20, 24, 26]	1	Over 1000 cases are disasters
	2	800–1000 cases are disasters
	3	600–800 cases are disasters
	4	400–600 cases are disasters
	5	Less than 400 are cases disasters
Internet penetration rate [20, 24]	1	Internet penetration rate is over 80%
	2	Internet penetration rate is 76–80%
	3	Internet penetration rate is 73–76%
	4	Internet penetration rate is 70–73%
	5	Internet penetration rate is less than 70%
Number of disaster prevention facilities [20]	1	There are over 200 disaster prevention facilities
	2	There are 150–200 disaster prevention facilities
	3	There are 100–150 disaster prevention facilities
	4	There are 50–100 disaster prevention facilities
	5	There are less than 50 disaster prevention facilities
Perceived safety [20, 24]	1	Over 20% of people feel very safe or safe regarding natural disaster
	2	18–20% of people feel very safe or safe regarding natural disaster
	3	16–18% of people feel very safe or safe regarding natural disaster
	4	14–16% of people feel very safe or safe regarding natural disaster
	5	Less than 14% of people feel very safe or safe regarding natural disaster
Number of medical doctors [19, 20]	1	There are over 8 medical doctors per 1,000 people
	2	There are 6–8 medical doctors per 1,000 people
	3	There are 4–6 medical doctors per 1,000 people
	4	There are 2–4 medical doctors per 1,000 people
	5	There are less than 2 medical doctors per 1,000 people
Financial independence of the borough [4, 20]	1	Financial independence is over 30%
	2	Financial independence is between 25 and 30%
	3	Financial independence is between 20 and 25%
	4	Financial independence is between 15 and 20%
	5	Financial independence is less than 15%

Socioeconomic vulnerability was applied to assess indirect damage caused by landslides. An index-based model was used to assess the socioeconomic vulnerability. The model was comprised of three subindexes and 17 proxy variables. Three subindexes were the demographic-social index, the secondary-damage-triggering index, and the preparation-response index. The socioeconomic vulnerability index calculated by the index-based model is applicable to common natural disasters. Although this study only demonstrated an example that the landslide exposure information obtained by Flow-R simulation is combined to assess the socioeconomic vulnerability of landslide disasters, the socioeconomic vulnerability of flood disasters can be assessed by combining with flood exposure information.

Finally, the urban landslide vulnerability was assessed by combining the physical vulnerability and socioeconomic vulnerability. The combined vulnerability therefore reflects both direct and indirect aspects of damage caused by landslides. The general trend of the findings in this study reveals that the higher population density areas under a weaker fiscal condition that are located at the downstream of mountainous areas are more vulnerable than the areas in opposite conditions. The framework and results of this study are expected to be used directly to prioritize the landslide damage reduction plans for the Seoul metropolitan area in South Korea.

The previous studies about landslide in South Korea were focused on mountainous areas. On the other hand, the influence of landslide in urban areas has not been analyzed. This study is prototype about assessing vulnerability in urban areas. The study area is Seoul, in South Korea. Therefore, this study has some limitations. One of limitations is that this study did not use quantitative output about landslide process. It is not the accurate landslide vulnerability assessment. However it is good enough as the first step for high quality landslide disaster vulnerability assessment in urban area including mountainous area.

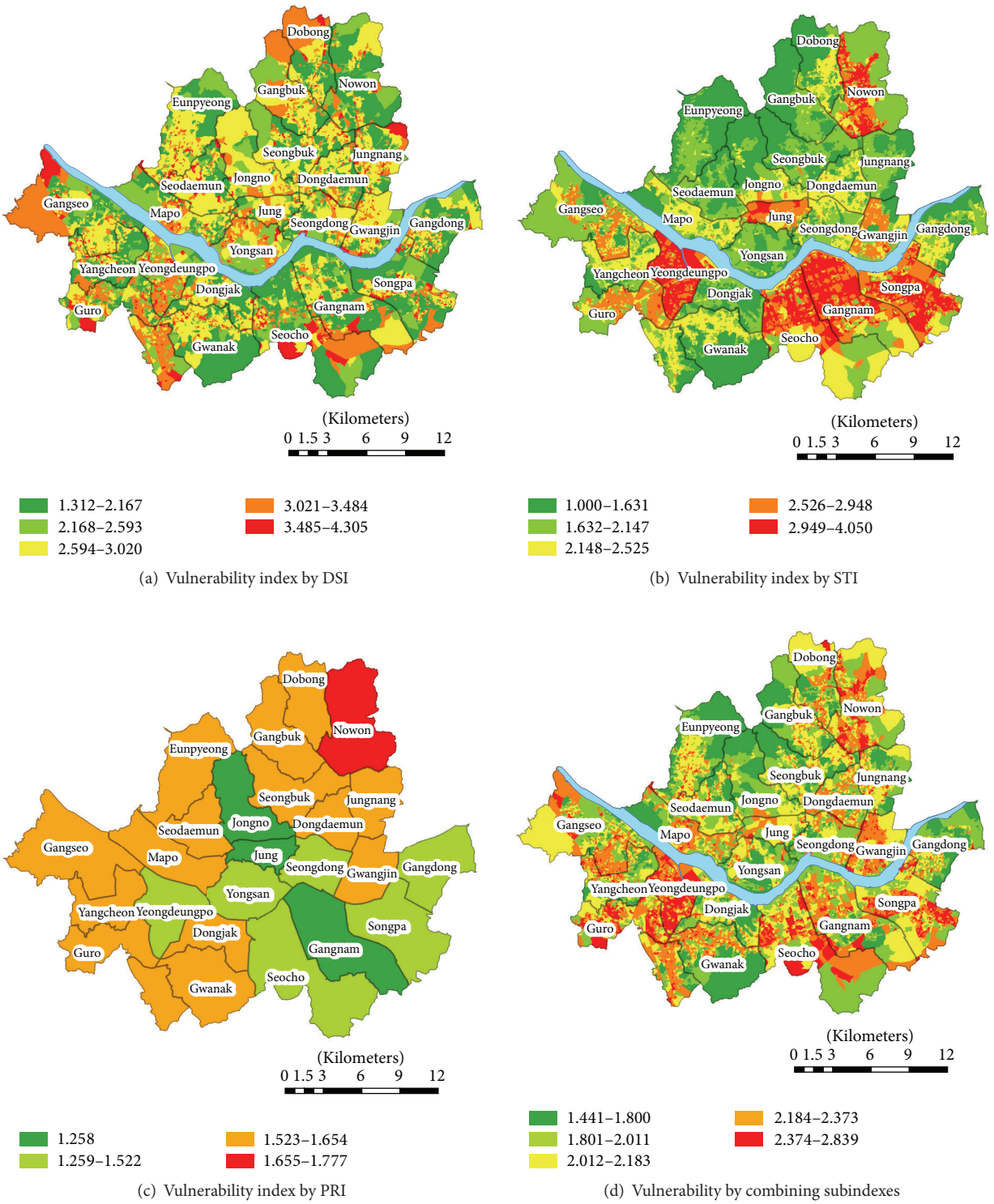

Figure 8: Result of socioeconomic vulnerability assessments.

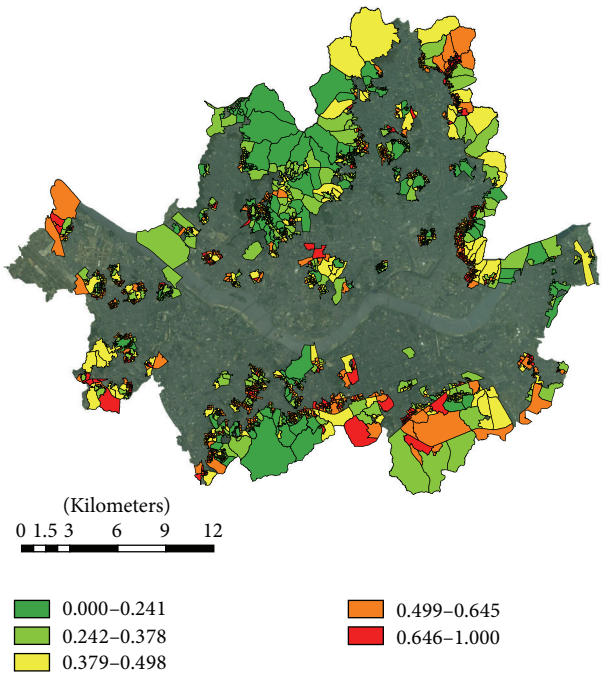

Figure 9: Socioeconomic vulnerability to landslide disaster.

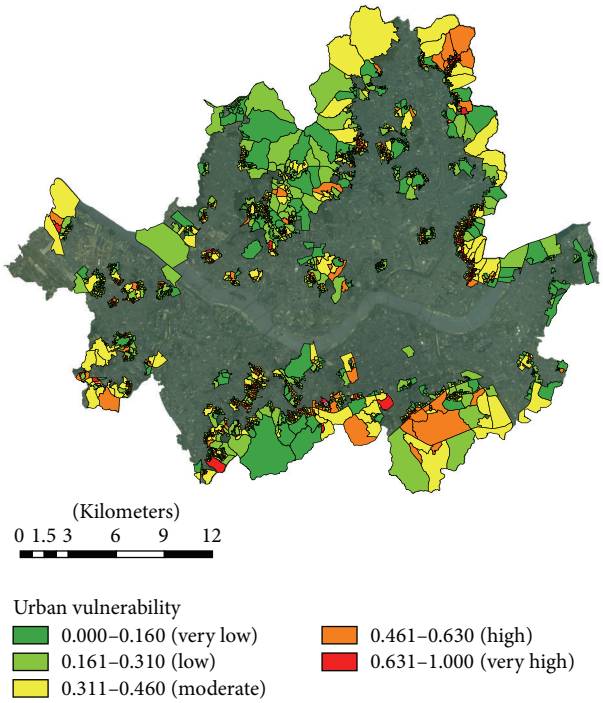

Figure 10: Urban vulnerability to landslide disaster.

Competing Interests

The authors declare that they have no competing interests.

Acknowledgments

This research was supported by a grant (13SCIPS04) from Smart Civil Infrastructure Research Program funded by Ministry of Land, Infrastructure and Transport (MOLIT) of Korea Government and Korea Agency for Infrastructure Technology Advancement (KAIA).

References

[1] S. Lee, J.-H. Ryu, J.-S. Won, and H.-J. Park, "Determination and application of the weights for landslide susceptibility mapping using an artificial neural network," *Engineering Geology*, vol. 71, no. 3-4, pp. 289–302, 2004.

[2] K.-Y. Song, H.-J. Oh, J. Choi, I. Park, C. Lee, and S. Lee, "Prediction of landslides using ASTER imagery and data mining models," *Advances in Space Research*, vol. 49, no. 5, pp. 978–993, 2012.

[3] K. Smith and R. Ward, *Floods: Physical Processes and Human Impacts*, John Wiley & Sons, Chichester, UK, 1998.

[4] S. L. Cutter, B. J. Boruff, and W. L. Shirley, "Social vulnerability to environmental hazards," *Social Science Quarterly*, vol. 84, no. 2, pp. 242–261, 2003.

[5] M. Galli and F. Guzzetti, "Landslide vulnerability criteria: a case study from Umbria, Central Italy," *Environmental Management*, vol. 40, no. 4, pp. 649–664, 2007.

[6] H. Kang and Y. Kim, "The physical vulnerability of different types of building structure to debris flow events," *Natural Hazards*, vol. 80, no. 3, pp. 1475–1493, 2016.

[7] Z. Li, F. Nadim, H. Huang, M. Uzielli, and S. Lacasse, "Quantitative vulnerability estimation for scenario-based landslide hazards," *Landslides*, vol. 7, no. 2, pp. 125–134, 2010.

[8] M. L. Carreño, O. D. Cardona, and A. H. Barbat, "A disaster risk management performance index," *Natural Hazards*, vol. 41, no. 1, pp. 1–20, 2007.

[9] A. Dwyer, C. Zoppou, O. Nielsen, S. Day, and S. Roberts, *Quantifying Social Vulnerability: A Methodology for Identifying Those at Risk to Natural Hazards*, Australian Government, Geoscience Australia, Symonston, Australia, 2004.

[10] Y. Park, S. Jeong, and S. Kim, "Natural disaster vulnerability assessment at boroughs and census output areas in seoul focusing on socio-economic perspective," *Journal of Korean Society of Hazard Mitigation*, vol. 14, no. 6, pp. 439–449, 2014.

[11] T. H. Siagian, P. Purhadi, S. Suhartono, and H. Ritonga, "Social vulnerability to natural hazards in Indonesia: driving factors and policy implications," *Natural Hazards*, vol. 70, no. 2, pp. 1603–1617, 2014.

[12] Statistical Geographic Information Service (SGIS), 2015, http://sgis.kostat.go.kr.

[13] P. Horton, M. Jaboyedoff, B. Rudaz, and M. Zimmermann, "Flow-R, a model for susceptibility mapping of debris flows and other gravitational hazards at a regional scale," *Natural Hazards and Earth System Science*, vol. 13, no. 4, pp. 869–885, 2013.

[14] P. Holmgren, "Multiple flow direction algorithms for runoff modelling in grid based elevation models: an empirical evaluation," *Hydrological Processes*, vol. 8, no. 4, pp. 327–334, 1994.

[15] Safeland, "Living with landslide risk in Europe: assessment, effects of global change, and risk management strategies," Deliverable D7.5 GIS-based training package on landslide risk assessment Work Package 7—Dissemination of project results, 2012.

[16] S. Fuchs, K. Heiss, and J. Hübl, "Towards an empirical vulnerability function for use in debris flow risk assessment," *Natural Hazards and Earth System Science*, vol. 7, no. 5, pp. 495–506, 2007.

[17] E. D. Haugen and A. M. Kaynia, "Vulnerability of structures impacted by debris flow," in *Landslides and Engineered Slopes*, Z. Chen, J. M. Zhang, K. Ho, F. Q. Wu, and Z. K. Li, Eds., pp. 381–387, Taylor & Francis, London, UK, 2008.

[18] B. Quan Luna, J. Blahut, C. J. van Westen, S. Sterlacchini, T. W. J. van Asch, and S. O. Akbas, "The application of numerical debris flow modelling for the generation of physical vulnerability curves," *Natural Hazards and Earth System Science*, vol. 11, no. 7, pp. 2047–2060, 2011.

[19] Safeland, "Living with landslide risk in Europe: assessment, effects of global change, and risk management strategies," Deliverable D2.6 Methodology for evaluation of the socio-economic impact of landslides (socio-economic vulnerability), 2012.

[20] Y. Park, J. Kim, D. J. Jo, and S. Kim, "Urban mud and debris flow disaster vulnerability assessment associated with landslide hazard map: application to Busan, Korea," *Journal of Korean Society of Hazard Mitigation*, vol. 15, no. 5, pp. 283–289, 2015.

[21] U. M. K. Eidsvig, A. McLean, B. V. Vangelsten et al., "Assessment of socioeconomic vulnerability to landslides using an indicator-based approach: methodology and case studies," *Bulletin of Engineering Geology and the Environment*, vol. 73, no. 2, pp. 307–324, 2014.

[22] T. L. Saaty, "A scaling method for priorities in hierarchical structures," *Journal of Mathematical Psychology*, vol. 15, no. 3, pp. 234–281, 1977.

[23] T. L. Saaty, "How to make a decision: the analytic hierarchy process," *European Journal of Operational Research*, vol. 48, no. 1, pp. 9–26, 1990.

[24] S. Tapsell, S. Tunstall, C. Green, and A. Fernandez, "Social indicator set," FLOODsite Report T11-07-01, 2005.

[25] A. Ebert, N. Kerle, and A. Stein, "Urban social vulnerability assessment with physical proxies and spatial metrics derived from air- and spaceborne imagery and GIS data," *Natural Hazards*, vol. 48, no. 2, pp. 275–294, 2009.

[26] A. Steinführer, B. De Marchi, C. Kuhlicke, A. Scolobig, S. Tapsell, and S. Tunstall, "Vulnerability, resilience and social constructions of flood risk in exposed communities," FLOODsite Report T11-07-12, 2009.

[27] B. Q. Luna, J. Blahut, C. Camera et al., "Physically based dynamic run-out modelling for quantitative debris flow risk assessment: a case study in Tresenda, northern Italy," *Environmental Earth Sciences*, vol. 72, no. 3, pp. 645–661, 2014.

[28] G. Gaprindashvili and C. J. Van Westen, "Generation of a national landslide hazard and risk map for the country of Georgia," *Natural Hazards*, vol. 80, no. 1, pp. 69–101, 2016.

Hindawi Publishing Corporation
Advances in Meteorology
Volume 2016, Article ID 6583906, 11 pages
http://dx.doi.org/10.1155/2016/6583906

Research Article

A Three-Parameter S-Shaped Function of Flood Return Period and Damage

Chaochao Li,[1,2] Xiaotao Cheng,[1] Na Li,[1] Zhongmin Liang,[2] Yanyan Wang,[1] and Song Han[1]

[1]*State Key Laboratory of Simulation and Regulation of Water Cycle in River Basin, Research Center on Flood & Drought Disaster Reduction of the Ministry of Water Resources, China Institute of Water Resources and Hydropower Research, Beijing 100038, China*
[2]*College of Water Conservancy and Hydropower Engineering, Hohai University, Nanjing 210098, China*

Correspondence should be addressed to Chaochao Li; lcc0828@gmail.com

Received 23 December 2015; Revised 19 April 2016; Accepted 19 May 2016

Academic Editor: Huan Wu

With growing flood risk due to increased urbanization, flood damage assessment and flood risk management must be reconsidered. To demonstrate and assess the new features and trends of flood risk in urbanized areas, a novel S-shaped function of return period and damage (*R-D*) is proposed. The function contains three parameters, which are defined as the maximum flood damage A, critical return period R_c, and integrated loss coefficient k. A basic framework for flood damage assessment was established to evaluate flood damage in the Taihu Basin under various scenarios. The simulation results were used to construct the flood *R-D* functions. The study results show that the flood *R-D* model based on the Gompertz function agrees well with the mutability of flood damage in the highly urbanized basin when the flood scale exceeds the defense capability. The *R-D* function can be utilized for timely and effective flood damage assessment and prediction. It can describe the impacts of socioeconomic development, urbanization degree, and flood control capability improvements well. The turning points of the function curve can be used as gradation criteria for rational strategy development associated with flood hazards.

1. Introduction

In modern society, with increasing population density and assets in flood control districts, under equivalent scales of flooding, flood damage is higher than it was in the past. To ensure security, a comprehensive system of flood control mechanisms has been built, and the flood control standard has been improved continuously. Disaster mitigation benefits can be achieved by optionally adopting flood control mechanisms. However, for events with extreme peak flows beyond design standards, the associated flood damage sharply increases [1, 2]. It is important to determine the evolutionary trends of flood risk in modern society. The formation mechanisms of chain reactions and mutability of floods provide the basis for predictive controls [3]. The relationship between flood return period and flood damage should be constructed based on a comprehensive consideration of the impacts of economic development, urbanization degree, and flood control capacity changes. Reasonable gradation criteria associated with flood hazards provide crucial information for strategy development and planning adaptation.

According to the *Atlas of Mortality and Economic Losses from Weather, Climate and Water Extremes 1970–2012*, storms and floods accounted for nearly 80 percent of all disasters due to weather, climate, and water extremes, resulting in nearly half of the related mortalities and over 80 percent of economic losses. As the population and wealth increase in urban areas, the flood risk also increases. Konrad reported that urbanization resulted in 2-year, 10-year, and 100-year flood peak increases by 100%~600%, 20%~300%, and 10%~250%, respectively [4]. Current assessments of flood damage mainly focus on direct economic loss. There are three main methods of flood damage assessment: (1) the traditional investigation method, (2) assessment models based on mathematical methods, and (3) integrated models based on geographic information system and remote sensing (GIS/RS). Investigation is the most basic method. The data integrity demand is high for this method. In the traditional investigation method, researchers

complete field investigations of property loss and casualties after disasters occur. It requires considerable manpower and is not suitable for predicting flood damage. Field survey and investigation data provide a foundation for flood damage assessment. Damage assessment models based on mathematical methods have been widely used. They can be divided into two types. One calculates flood damage by constructing flood loss rates for hazard-affected bodies. This type of model sets the water depth or submerged period as an independent variable and flood loss rate as a dependent variable. Then, regression equations of water depth or submerged period and flood loss rate are established [5]. For example, Penning-Rowsell and Chatterton [6] and Parker et al. [7] proposed 140 flood vulnerability curves. HAZUS-MH includes more than 900 damage curves for estimating damage to various types of buildings and infrastructures [8, 9]. Australia and Japan built vulnerability curves for damage estimation of different buildings [10]. The other type includes rapid assessment methods, such as fuzzy comprehensive evaluations, grey correlation analyses, genetic algorithms, and BP neural networks [11–16]. These methods require reliable historical flood data. China currently lacks a historical flood database. In addition, the reliability of socioeconomic and property loss data is poor. With the technological development of hydrologic models, hydraulic models, RS, and GIS, integrated models have been widely used in recent years. Flood inundation information is the input data used in these methods. Then, inundation information and socioeconomic information are analyzed by spatial overlay [17, 18]. Detailed geographic data are needed to construct integrated models based on GIS/RS. Therefore, mathematical methods and integrated models based on GIS/RS are combined to construct *R-D* function curves, which are established for rapid and effective flood damage assessment.

S-shaped growth curves are often utilized to describe variable growth processes such as slow growth, fast growth, and decay. Because hazard-affected bodies have defensive and recoverable capabilities, the flood damage development process will be bounded. In the initial phase, flood damage increases slowly because of resistance effects. Due to increasing flood or rainfall accumulation, the energy exceeds the defensive capability. Then, a rapid development phase occurs. Finally, with an energy release, the development process enters the attenuation phase. In previous studies, Li et al. found that the general type of damage loss mimics an S-shaped curve [19, 20]. Yu et al. developed direct economic loss curves for the minimum, maximum, and most likely floods based on a Monte Carlo method [21]. These loss curves are all S-shaped. Hence, it is reasonable to build S-shaped functional curves of flood damage.

Some studies have attempted to build damage functions by curve fitting. For example, Chen et al. established a water-induced disaster damage curve based on a hyperbolic tangent function [22]. However, the meanings of parameters in the S-shaped function were not defined according to their physical meanings. Additionally, the function curve cannot describe the impacts of socioeconomic development, urbanization, and flood control capability changes. Including flood protection mechanisms and urbanization in *R-D* functions is novel and can indicate resilience changes. In this paper, mathematical methods and integrated models based on GIS were combined to construct *R-D* function curves. They can be utilized for flood damage assessment and prediction. The chain reaction associated with a flood disaster was analyzed, and the mutability feature of flood damage was summarized. The Taihu Basin in China was taken as the study area. Several S-shaped functions were selected to construct the *R-D* functions, which can be used for rational strategy development.

2. Methods and Materials

2.1. The Study Area. The Taihu Basin, which is located in the estuary areas of the Yangtze and Qiantang Rivers, is one of the most important economic regions in China (Figure 1). The Taihu Basin has developed rapidly due to its various advantages, such as high agricultural production, a developed industry, a stable economic base, and a dense population. Because the basin is a phialiform region with a lower center and surrounding highlands, it is prone to serious flood disasters caused by plum rains, typhoons, and storm surges. Features of flood risk in the Taihu Basin are very sensitive to both climate changes and rapid urbanization [25]. The influence of urbanization is discussed in this paper.

Urbanized areas in the Taihu Basin increased by over four times from 1995 to 2010. Meanwhile, the cultivated area decreased by nearly 40 percent, and the population increased by 3.65 million in the past 10 years (Figure 2). The most serious flood disasters in the Taihu Basin occurred in 1954, 1991, and 1999. Since then, various flood control mechanisms have been built, such as dikes, sluices, polders, and pump stations. The evolutionary trends and key features of flood risk have changed in the urbanized basin. The main factors are rainfall, urbanization, and socioeconomic and flood control mechanisms.

2.2. Procedure. The flood risk assessment framework is adopted in this paper from the China/UK scientific cooperation project "*China-UK Scenario Analysis Technology for River Basin Flood Risk Management in the Taihu Basin*" [26]. The methodology contains a number of steps (Figure 3).

(1) Hydrological Data Collection and Frequency Analysis. The analysis results are used as inputs for hydraulic modelling and *R-D* modelling.

(2) Climate Input Analysis. The hydrological system is simulated using the distributed hydrological models. A variable infiltration capacity (VIC) model is used to model fluvial inflows, and the Soil Conservation Service Curve Number (SCS CN) method is applied to determine direct rainfall inputs [27].

(3) Broad-Scale Hydraulic Analysis. A hydrodynamic model (ISIS) is used to model the movements of water through the network of channels and flood storage cells in the basin [28].

(4) Economic Prediction. Future climate scenarios are generated using the Providing Regional Climates for Impacts

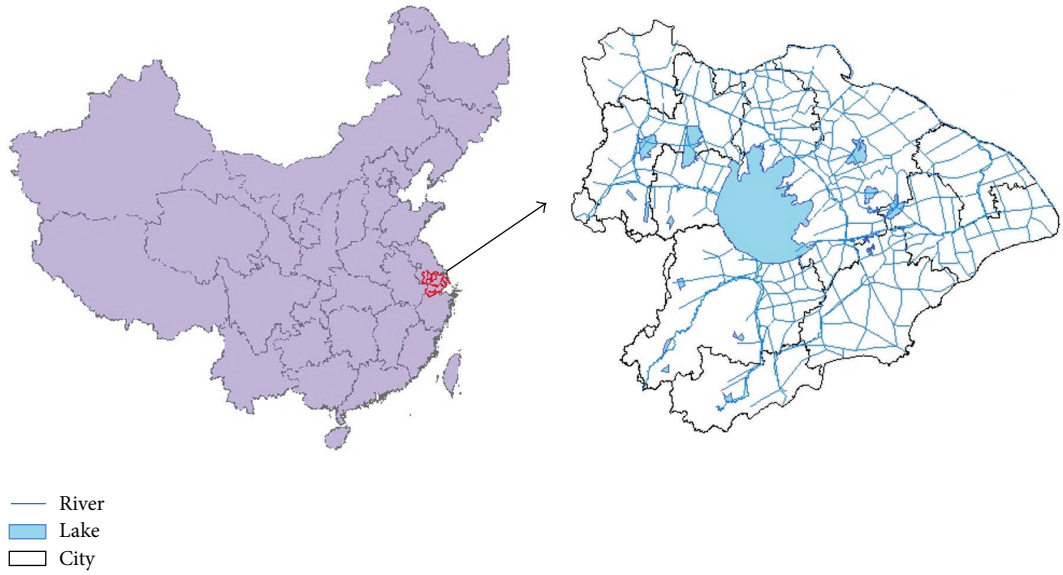

Figure 1: The location of the Taihu Basin.

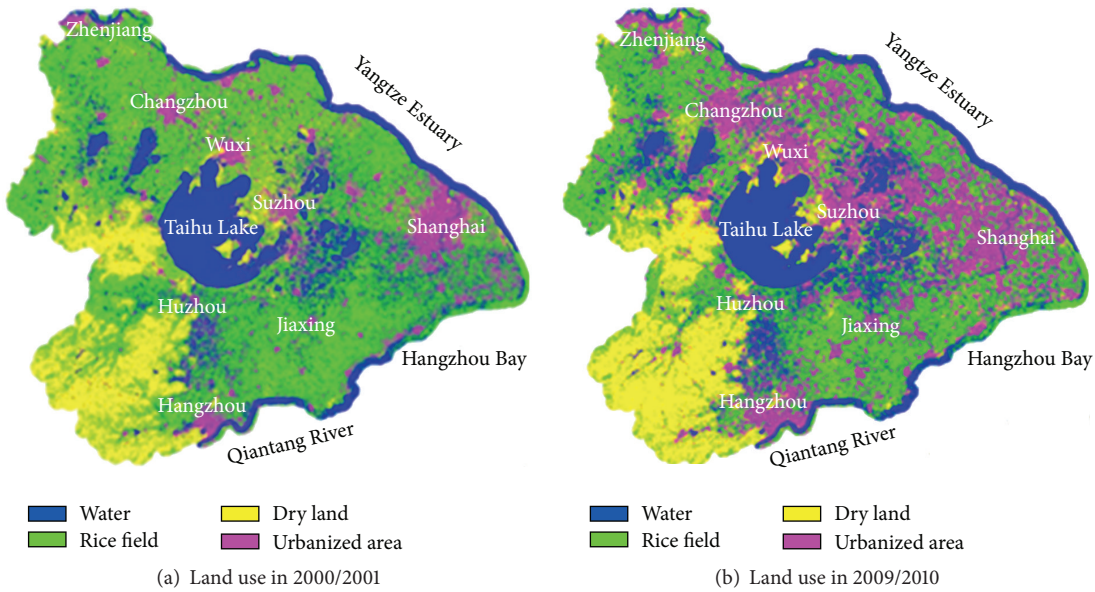

Figure 2: Changes in land use types from 2000 to 2010 in the Taihu Basin [23].

Studies (PRECIS) regional climate model. The downscaling method is used to predict economic factors. Details can be found in Penning-Rowsell et al. [29]. The economic index is predicted based on the population, economy, agricultural land, economic structure, urbanization rate, family properties, and so forth.

(5) Flood Damage Assessments. The Taihu Basin Risk Assessment System (TBRAS) risk analysis model is established to model inundation depths in the flood cells and calculate associated economic damage [30].

(6) Flood Damage Function Construction. The simulation results of flood damage assessment modelling are taken as samples to construct the flood *R-D* functions.

2.3. Data. Data were acquired from the China/UK scientific cooperation project. The 30-day design rainfalls with frequencies of 0.001, 0.002, 0.005, 0.01, 0.02, and 0.05 were used as flood hazard data. Socioeconomic and land use changes are considered in the future scenario. Societal development is established based on the statistical downscaling method

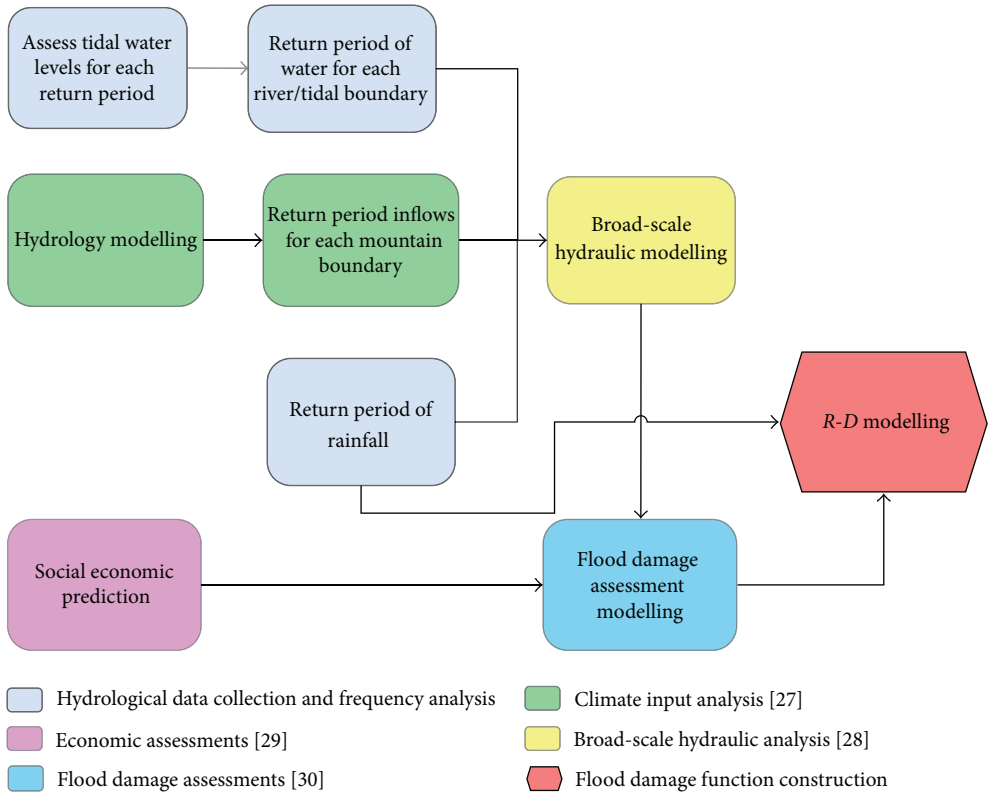

Figure 3: Basic framework of flood risk analysis [24].

according to the IPCC A2 emission scenario. The development of the world is uneven, and regional characteristics are enhanced. The economy develops at a medium speed. The population continues to grow. However, the agricultural land use pattern shows a rapid decline. The current data and predicted population and GDP results are shown in Table 1.

The hydrological model, hydrodynamic model, and flood loss assessment model were validated. The most serious flood disasters in the Taihu Basin occurred in 1991 and 1999. The surveyed flood damage cases were 141 million CNY in 1999. The scale of Taihu Basin flood in 1999 is over 100 years. According to studies by Liu et al. [27] and Wicks et al. [28], the hydrology-hydraulics model was evaluated against observations from 1999. The simulation results of flood damage are shown in Table 2. The simulated 100-year and 200-year flood damage cases in 1999 were 104 million and 176 million, respectively. The simulation value and survey value are of the same order of magnitude. With the consideration of uneven distributions of rainfall in time and space, the assessment of the flood return period may not be entirely consistent with the actual situation. However, the damage assessment results are reliable and can be utilized as samples for *R-D* function construction.

Table 1: Predicted results of GDP and population.

	1999	2005	2020 A2	2030 A2	2050 A2
GDP (100 million CNY)	10768	20216	38946	62008	108131
Population (million)	44.71	47.14	54.07	58.87	68.46

Table 2: Simulation results of flood damage (unit: 100 million CNY).

Return period (years)	Flood frequency	1999	2005	2030 A2	2050 A2
1000	0.001	312.0	457.3	1003.5	1556.3
500	0.002	291.0	427	939.09	1455.5
200	0.005	176.0	259.1	575.8	904.7
100	0.01	104.0	161.7	365.5	578
50	0.02	65.0	85.4	239.3	381.7
20	0.05	35.0	56.2	129.3	206.8
10	0.1	12.0	21.8	52.9	86.9
2	0.5	0.55	0.90	1.8	2.87

2.4. Characterizing Urbanized Area Floods. With basin urbanization, the flood risk shows new characteristics. In rural areas, the main economic losses associated with flood disasters are agricultural losses, and the affected area is equal to the inundated area. However, in urban areas, the economic losses are much higher, and the affected area is much larger than the inundated area. The indirect economic loss is even more than the direct economic loss. To reduce the flood risk in modern society effectively, the formation mechanisms

of flood-induced chain reactions and mutability must be researched intensively.

2.4.1. Chain Reaction of an Urban Flood Disaster. The chain reaction associated with a flood disaster is a series of lifeline system damage cases or failures that occur at the same time or in succession. After the key systems suffer damage due to flooding, the chain reaction forms, and the flood damage expands sharply. Lifeline systems include types of infrastructures that maintain normal operation in modern cities, such as traffic, communication, internet, water supply, power supply, gas supply, waste disposal, sewage treatment, and drainage systems. For example, during the "Beijing 21 July" urban storm event in 2012, some drainage pumps stopped running due to power system damage, and the waterlogged roads led to traffic gridlock. The most vulnerable systems can be identified and better protected through chain reaction analyses. Power supply systems may be the most vulnerable systems, and key facilities must be moved from low-lying areas to higher elevations or protected by special measures according to the risk analysis. Meanwhile, key link nodes can be found and cut off to stop further extension of the flood damage. After the drainage pump stations stop working due to power outages, the anticipatory standby generators or circuits for pumping stations can be started promptly to ensure normal operation of drainage systems during storm events. Flood chain reactions include both positive and negative feedback between floods and lifeline systems. Making full use of the negative feedback, we can minimize costs to obtain larger benefits of flood prevention. Furthermore, city landscapes and sports venues can be designed as parts of the flood regulation system with temporary rain storage functions.

2.4.2. Mutability of Urban Flood Damage. The mutability of flood damage is a phenomenon that occurs when the flood damage suddenly increases near a certain frequency or return period of a flood. In Beijing, the direct economic loss associated with flood disasters from 2006 to 2008 was about 20 million CNY. The flood disaster loss of the "23 June 2011" rainstorm was 13.83 billion CNY. The flood disaster loss of the "21 July 2012" rainstorm surged to 162.15 billion CNY. The maximum point rainfall in Beijing city was 460 mm (nearly a 500-year rainfall event), and the mean areal rainfall was 170 mm. The maximum point rainfall in the urban center was 328 mm (nearly a 100-year rainfall event), and the mean areal rainfall was 215 mm. The main rivers in Beijing are "protected" by 50-year to 100-year levees. According to the data, the flood disaster loss increased sharply in 2012, which proves the existence of mutability of urban flood damage. Within the flood control capacity, flood risk can be reduced effectively and the flood alleviation benefits are significant. After the flood magnitude exceeds the flood control standard, the loss will sharply increase and exhibit features of mutability. It is difficult to meet the increasing demand for flood control solely based on structural measures. Appropriate nonstructural measures provide sound strategies for sustainable development. Through studying the mutability phenomenon, the critical flood frequency or return period can be determined and used to classify the disaster grades.

2.5. The Construction of Flood Damage Functions

2.5.1. The Definition of Flood Risk Functions and Parameters. In recent years, a widely accepted concept in flood risk studies has been termed expected annual damage (EAD) [31–33]. It can be expressed as follows:

$$\text{Risk} = \int_0^1 D(p)\, dp, \tag{1}$$

where D is the damage of a given flood event and p is the probability of this flood event within a year.

The return period R is used instead of probability p and $p = 1/R$. The risk can then be expressed as follows:

$$\text{Risk} = \int_0^\infty D(R)\, dR. \tag{2}$$

$D(R)$ can be expressed as an S-shaped function according to the analysis above. R is an independent variable, and D is a dependent variable. A typical S-shaped function has three parameters. These parameters should describe the chain reaction and mutability features in an urbanized basin. The following assumptions are made. (1) The maximum value of flood damage A is associated with the socioeconomic indexes. (2) The abscissa of the inflection point is defined as the critical return period R_c, which is associated with the integrated flood control standard. (3) The slope of the function curve can be adjusted by the integrated loss coefficient k, which is associated with the flood vulnerability indexes.

2.5.2. The Determination Methods of Parameters. As shown in Figure 4, the flood R-D function curve is S-shaped. The characteristics of the $D(R)$ function are summarized as follows. (1) $D(R)$ monotonically increases. (2) The curve contains two key points: A and B. Point A is called the damage-arising point, and a rainfall event can lead to flood damage after point A. Point B is called the damage-ceasing point, when flood damage gradually approaches an extremum value. (3) Point C is the inflexion point, at which the rate of change in damage begins to decline. It is also called the damage transition point. These three points divide the $D_2(R)$ curve into four parts that can be used to determine standard grades of flood disaster damage. The four grades are small, medium, large, and larger.

Their corresponding values can be determined using function derivatives. Line $dD(R)/dR$ and line $dD^2(R)/dR^2$ are the first and second derivative curves of $D(R)$, respectively (Figure 5). The first derivative function indicates that the slope of the flood damage curve is highest when $R = R_c$. Point A and point B are the extreme points based on the slope change of curve, that is, the extreme points of the second derivative of the $D(R)$ function.

The maximum value of flood damage A, critical return period R_c, and integrated loss coefficient k are the three main parameters, which can be determined through experience, experimental simulations, or curve fitting. Historical data or simulation data can be utilized for curve fitting. Mathematical statistical analysis tools can be used to determine the values of the parameters and draw diagrams of R-D function curves.

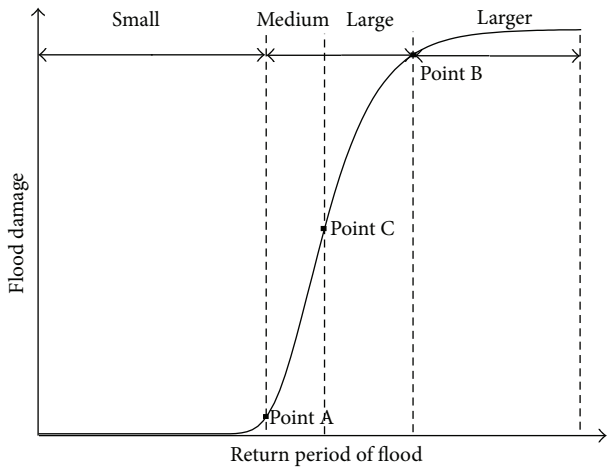

Figure 4: Flood *R-D* function curve.

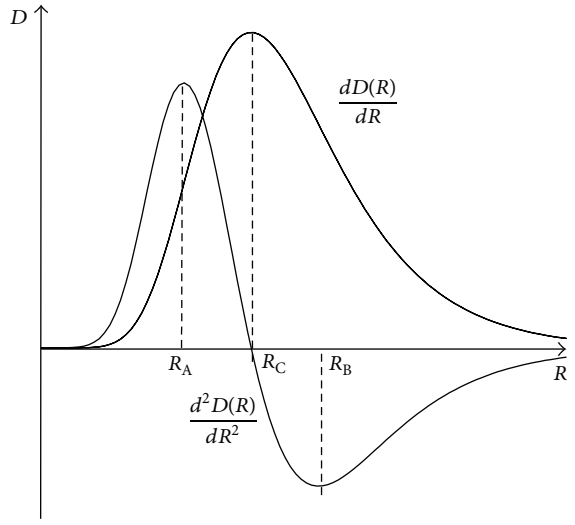

Figure 5: The first and second derivative curves of an *R-D* function.

Some commonly used tools include Origin, SPSS (Statistical Product and Service Solutions), and the MATLAB Curve Fitting Toolbox.

2.6. Conceptual Model. According to the chain reaction and mutability analysis of urban flood, *R-D* function variations are caused by socioeconomic, flood control capability, and flood vulnerability changes. Hence, four scenarios are assumed according to the impact factors.

Scenario 1 (undeveloped basin). The relationship between flood or rainfall return period and flood damage in an undeveloped state is illustrated by the black line. With increases in water depth and inundated area, the flood damage increases.

Scenario 2 (developed basin). Due to socioeconomic growth, the flood damage in a developed basin is larger than that in an undeveloped basin. The *R-D* function curve shifts upward.

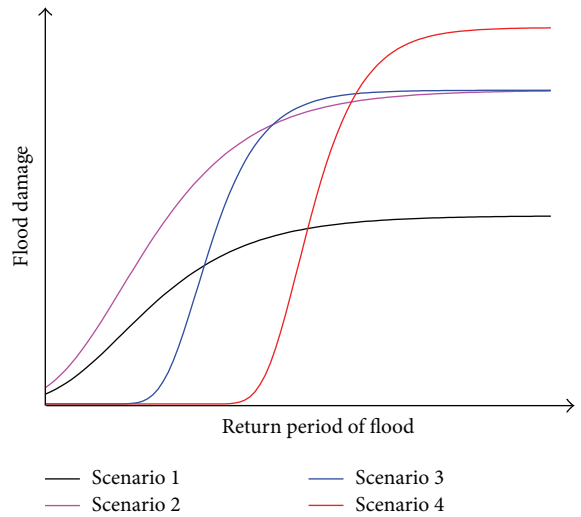

Figure 6: Conceptual *R-D* function curves.

Scenario 3 (protected basin). To prevent flood disasters, a flood control system is built. Within the flood control standard, the flood damage decreases significantly. The slope of the curve reaches a maximum value when the return period of the flood is near the flood control standard.

Scenario 4 (further developed and protected basin). With further improvement of the flood control standard and socioeconomic factors, the *R-D* function curve will shift to the upper right, as demonstrated by the red line in Figure 6.

2.7. Function Selection. In practice, some commonly used S-shaped curves are summed, such as the logistic curve, Gompertz curve, and Richards curve. According to the conceptual analysis of the flood *R-D* function, three S-shaped functions with three parameters were selected. The functions are the Gompertz function, logistics function, and hyperbolic tangent function.

(1) Gompertz Function. Consider

$$D = Ae^{-e^{-k(R-R_c)}}. \tag{3}$$

In (3), D is the flood damage, R is the return period of the flood, A is the maximum damage, R_c is the critical period, and k is the integrated loss coefficient. The function characteristics are as follows: the minimum value is zero, the maximum value is A, the abscissa of the critical point is R_c, and the maximum slope is Ak/e.

(2) Logistics Function. Consider

$$D = \frac{A}{1 + e^{-k(R-R_c)}}. \tag{4}$$

The function characteristics are as follows: the minimum value is zero, the maximum value is A, the abscissa of the critical point is R_c, and the maximum slope is Ak/e.

Table 3: Function fitting results in 1999.

Function	Parameter	Value	Standard error	Adj. R-squared
Gompertz	A (100 million)	306.08	11.86	0.99
	R_c (year)	120.53	11.33	
	k	0.0088	0.0011	
Logistics	A (100 million)	301.30	14.86	0.97
	R_c (year)	166.59	16.93	
	k	0.015	0.0025	
Hyperbolic tangent	A (100 million)	301.31	14.86	0.97
	R_c (year)	166.62	16.93	
	k	0.0074	0.0013	

Table 4: Function fitting results in 2005.

Function	Parameter	Value	Standard error	Adj. R-squared
Gompertz	A (100 million)	448.20	17.19	0.99
	R_c (year)	118.46	11.076	
	k	0.0088	0.0011	
Logistics	A (100 million)	441.53	21.90	0.97
	R_c (year)	164.58	16.91	
	k	0.015	0.0025	
Hyperbolic tangent	A (100 million)	441.56	21.90	0.97
	R_c (year)	164.63	16.91	
	k	0.0074	0.0013	

(3) Hyperbolic Tangent Function. Consider

$$D = \frac{A}{2}\left(\frac{e^{2k(R-R_c)} - 1}{e^{2k(R-R_c)} + 1} + 1\right). \quad (5)$$

The function characteristics are as follows: the minimum value is zero, the maximum value is A, the abscissa of the critical point is R_c, and the maximum slope is $Ak/2$.

3. Results and Discussion

3.1. Results of Status Scenarios. Data from 1999 and 2005 were used as a basic sample, and the fitting results of three functions are shown in Tables 3 and 4. The parameter values and standard errors of the logistics and hyperbolic tangent functions are almost the same. The maximum flood damage A values in 1999 and 2005 were 301 and 442 billion CNY, respectively. The standard errors of A in 1999 and 2005 were 14.86 and 21.90, respectively. The average critical return period is approximately 165.61 years. The ordinate of the inflection point is $A/2$, and the growth process is symmetrical. However, there is no such characteristic in the Gompertz function. The maximum flood damage A values are 306 and 448 billion, the standard errors of A are 11.86 and 17.19, and the average critical return period is approximately 120 years. The maximum flood damage A is larger, but its standard error is smaller than others, and the maximum flood damage A is much closer to the flood damage of a 1000-year flood. The adjusted R^2 is particularly useful in the feature selection stage of model building. The closer this value is to one, the better the model fit is. The Gompertz function best reflects flood damage compared to the estimates of the other functions. Therefore, the Gompertz function is selected for future scenario fitting. The fitting results of the Gompertz function are shown in Figure 7.

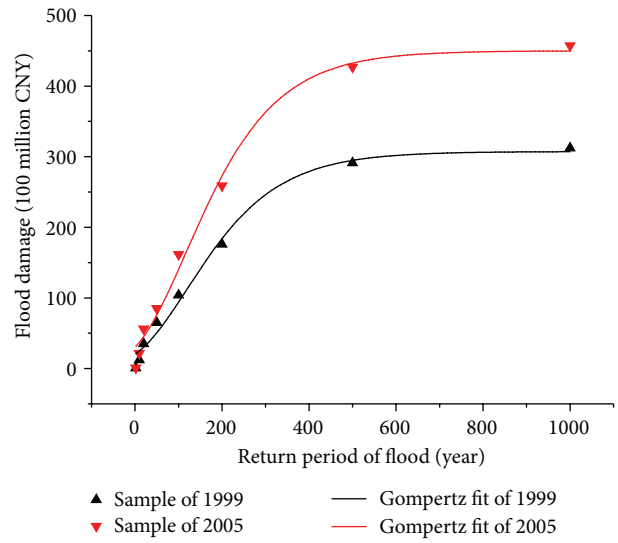

Figure 7: Gompertz function fitting results in 1999 and 2005.

The most serious flood disasters in the Taihu Basin occurred in 1991 and 1999. The surveyed flood damage cases were 113 and 141 million. The maximum 30 d rainfall in 1991 was 502 mm, which is nearly equivalent to an 80-year return period flood. The average areal rainfall in 1999 over various characteristic periods (7 d, 30 d, 60 d, and 90 d) was close to or over the 100-year level [34]. The R-D curve of the Taihu Basin in 1999 is shown in Figure 7. The 100-year and 200-year flood damage cases in 1999 simulated by the R-D curve are 112 million and 183 million, respectively. The simulated and surveyed values of flood damage are of the same order of magnitude. Due to uneven distributions of rainfall in time and space, the estimated rainfall return periods are very different. The flood R-D curve is reliable for damage assessment.

3.2. Results of Future Scenarios. The Gompertz function is chosen for flood damage prediction. According to the fitting results of the Gompertz function, the mean value of the critical return period R_c is 119.5 years, and the result is rounded up to 120 years. The mean value of the integrated loss rate k is 0.0088. The linear relationship between GDP and flood damage is established based on a 1000-year return period. The values of maximum flood damage A are shown in Table 5. The Gompertz function fitting result of future scenarios is shown in Figure 8. The curve fitting results and example data match well. The flood R-D models of 2030 and 2050 based on the Gompertz function exhibit good agreement with the mutability of flood damage in highly

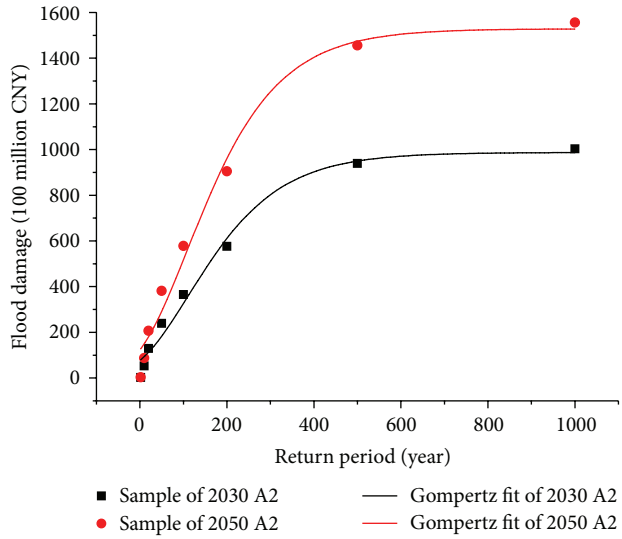

Figure 8: Gompertz function fitting results in 2030 and 2050.

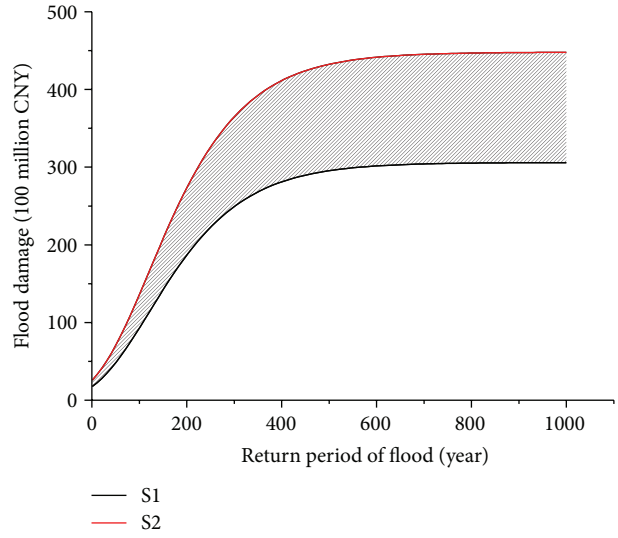

Figure 9: The impact of economic development.

Table 5: The values of the maximum flood damage A (100 million).

Year	1999	2005	2030 A2	2050 A2
A	306	448	980	1566

urbanized basins when the scale of a flood exceeds the defense capability.

3.3. Discussion. The most serious flood disasters in the Taihu Basin occurred in 1954, 1991, and 1999. These flood events were mainly caused by plum rains. According to the statistical data associated with plum rains in Taihu basin from 1954 to 2009, the average onset and end dates of plum rains are 15 June and 8 July, respectively. Thus, 30 days is chosen as the characteristic period in this study. With the extension of the characteristic period, the total rainfall increases. Thus, the flood damage also increases. If the characteristic period increases (e.g., 3 d, 7 d, 60 d, or 90 d), the function curve will shift upward; however, the overall shape of the function will not change. In the Taihu Basin, the characteristic period of 30 days approximates the average period of the plum rain season. It is suitable for flood damage assessment in large-scale basins.

The evolutionary trends of flood risk in urbanized basins change. Flood damage assessments should describe the impacts of socioeconomic development, urbanization, and flood control capability improvements. *R-D* function curves are used as effective evaluation methods for flood damage assessment and prediction. Compared with mathematical evaluation methods, *R-D* functions do not require many historical flood disaster data. The data used to construct *R-D* functions are the simulation results of flood damage assessment models based on GIS. Flood *R-D* functions can convert these discrete points into continuity equations. Assessment and prediction of flood damage for any flood return period can be quickly acquired by consulting figures. The applicability is more extended than those in previous studies. It can be utilized to estimate urbanization impacts and alleviation benefits.

3.3.1. The Evolutionary Trends of Future Flood Risk. According to the results of future scenarios, *R-D* functions can demonstrate the evolutionary tendencies of flood risk due to economic growth. The maximum flood damage A is related to GDP. The flood damage function curve in 1999 is taken as inherent characteristic curve S1, for which $D_1(R) = 306e^{-e^{-0.0088(R-120)}}$. The flood damage function curve in 2005 is taken as economic development curve S2, for which $D_2(R) = 448e^{-e^{-0.0088(R-120)}}$. The maximum flood damage A increases from 306 to 448 million CNY. The impact of economic development can be computed by finding the difference between the S2 and S1 integral areas, which is shown as the shaded area in Figure 9. Due to urbanization and economic development, the flood risk increases by 46.6% from 1999 to 2005 in the Taihu Basin, and it will increase by 59.8% from 2030 to 2050. The impact of increased economic development on flood risk will increase in the future.

Flood control capability development curve S3 is given by $D_3(R) = 448e^{-e^{-0.0088(R-240)}}$. It is assumed that the flood control standard has improved. The critical return period R_c increases from 120 to 240 years. The benefits of flood control mechanisms can be expressed as the difference between the S2 and S3 integral areas, which is shown as the shaded area in Figure 10. If the flood control standard increases by a factor of two, the flood risk will decrease by 14.54%.

Flood vulnerability change curve S4 is given by $D_4(R) = 448e^{-e^{-0.0176(R-240)}}$. The integrated loss coefficient k increases from 0.009 to 0.018. The intersection point of S3 and S4 is (R_i, D_i). When $0 < R < R_i$, the flood damage decreases. When $R > R_i$, the flood damage increases. With changes in

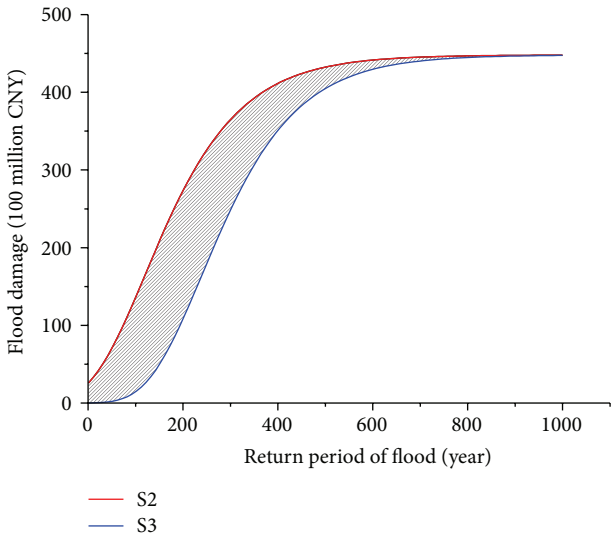

Figure 10: The impact of flood control capability development.

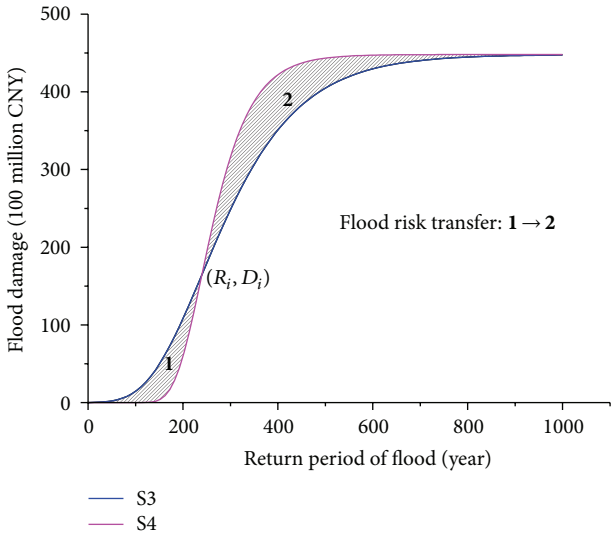

Figure 11: The impact of flood vulnerability change.

flood vulnerability, the flood risk shifts from shaded area **1** to shaded area **2**, which is shown in Figure 11:

$$I_{\text{decrease}} = \frac{\int_0^{R_i} D_3(R) - D_4(R)\,dR}{\int_0^{R_i} D_3(R)\,dR} = 48.1\%,$$
$$I_{\text{increase}} = \frac{\int_{R_i}^{1000} D_4(R) - D_3(R)\,dR}{\int_{R_i}^{1000} D_3(R)\,dR} = 6.7\%. \quad (6)$$

3.3.2. The Index of Urban Flood Control Management. As shown in Figure 12, $D_2(R)$ is the function curve of 2005. $D_2'(R)$ and $D_2^{(2)}(R)$ are the first and second derivative curves of the flood *R-D* function, respectively, and the parameters are $R_A = 10$ years, $R_C = 120$ years, and $R_B = 230$ years. Point A is the damage-arising point, point B is the damage-ceasing

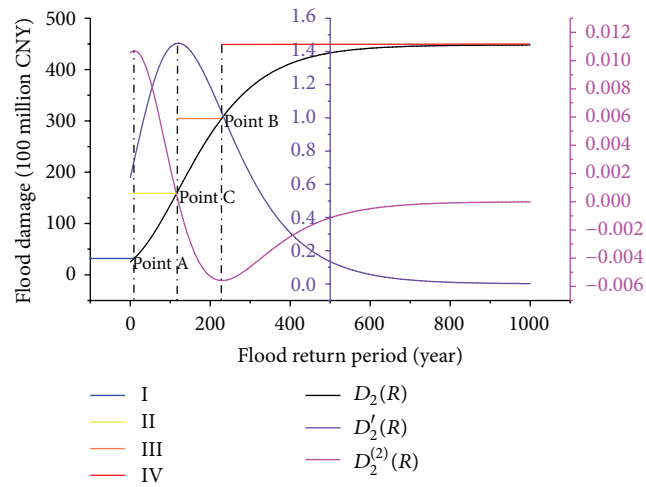

Figure 12: The turning points and derivative curves of the *R-D* function (2005). Labels "I, II, III, and IV" represent four grades of flood damage: small, medium, large, and larger, respectively. They correspond with Figure 4 and Table 6.

point, and point C is the damage transition point. These three points divide the $D_2(R)$ curve into four parts that can be used to determine standard grades of flood disaster damage. The four grades are I small, II medium, III large, and IV larger. Flood grade division can be utilized to develop flood control standards and flood control planning.

Damage transition point C corresponds to parameter R_c (critical return period), which is associated with the integrated flood defense capability or flood control standard of the basin. Resistance is related to the system's ability to prevent floods, while resilience determines the ease with which the system recovers from floods [35]. Thus, the demarcation line of these two processes is the integrated standard of flood control mechanisms or flood defense capability. Within the defense standard, the flood control mechanisms operate well. Resistance strategies are aimed at flood prevention. When the flood scale exceeds the defense capability, the situation becomes out of control. The resilience strategy aims to minimize the flood impacts and enhance the recovery from those impacts. Different strategies are designed for different grades of flood hazards (Table 6).

4. Conclusion

China is in a stage of rapid urbanization and has huge potential for economic growth. Because the pressure associated with flood risk caused by urbanization is still increasing, flood risk management must be reconsidered. The S-shaped function of the flood return period and damage can describe the impacts of socioeconomic development, urbanization degree, and flood control capability improvements very well. The main advantage of this model is that its application is not restricted by the scale of the study area. It can be utilized for flood damage assessment and prediction. Three conclusions can be drawn from this research.

(1) Due to urbanization and economic development, the flood risk increased by 46.6% from 1999 to 2005 in the Taihu

Table 6: The grades of flood hazards and main strategies.

Grade	Return period	Flood damage	Turning point	Physical meaning	Main strategy
I	$0 < R \leqslant R_A$	Small	Point A	Damage-arising point	Resistance strategy
II	$R_A < R \leqslant R_C$	Medium	Point A	Damage-arising point	
			Point C	Damage transition point	
III	$R_A < R \leqslant R_B$	Large	Point C	Damage transition point	Resilience strategy
			Point B	Damage-ceasing point	
V	$R \geqslant R_B$	Larger	Point B	Damage-ceasing point	

Basin, and it will increase by 59.8% from 2030 to 2050. The impact of increased economic development on flood risk will increase in the future. When the flood control standard increased by a factor of two in 2005, the flood risk decreased by 14.54%. It is difficult to meet the increasing demand for flood control solely using structural measures. If the flood vulnerability changes, the flood risk will not increase but will transfer. A flood vulnerability method should be provided to effectively decrease the flood risk in future studies.

(2) The turning points of R-D functions provide an important basis for flood risk management. The critical return period R_c is 120 years in the Taihu Basin. It describes the composite flood control standard. This paper discusses the damage transition point as the boundary between the resistance strategy and resilience strategy in flood risk management systems.

(3) The model accuracy can be improved by verifying more data. Considering the limitations of historical flood data, only the 1999 Taihu Basin flood was used to verify the simulation models. The relationship between the maximum flood damage A and socioeconomic development has been proven. In the future, the relationships between other parameters and meaningful statistical data should be verified. In addition, accurate simulations of flood control mechanisms should be provided using hydraulic models, and reasonable assessment indexes of flood control capability and flood vulnerability should be created. The rationality of parameters R_c and k will be verified in further studies.

Competing Interests

The authors declare that there is no conflict of interests regarding the publication of this paper.

Acknowledgments

The work described in this paper was supported by the following: (1) Key Projects in the National Science & Technology Pillar Program during the Twelfth Five-Year Plan Period (no. 2012BAC21B02) and (2) Public Welfare Special Research Projects of Ministry of Water Resources (nos. 201401038 and 201501014).

References

[1] X.-T. Cheng, "Strategic demand for enhancing flood and drought management and investigation on policies of water governance," *Journal of Hydraulic Engineering*, vol. 39, no. 10, pp. 1197–1203, 2008 (Chinese).

[2] H. Wang, C.-Z. Li, and X.-T. Cheng, "Quantitative analysis of storm water management strategies in the process of watershed urbanization," *Journal of Hydraulic Engineering*, vol. 46, no. 3, pp. 271–279, 2015 (Chinese).

[3] X.-T. Cheng and C.-C. Li, "The evolutionary trend, key features and countermeasures of urban flood risk," *China Flood & Drought Management*, vol. 25, no. 3, pp. 6–9, 2015 (Chinese).

[4] C. P. Konrad, "Effects of urban development on floods," U.S. Geological Survey Fact Sheet 076-03, 2003, http://pubs.usgs.gov/fs/fs07603/.

[5] S. Das and R. Lee, "Nontraditional methodology for flood stage-damage calculations," *Journal of the American Water Resources Association*, vol. 24, no. 6, pp. 1263–1272, 1988.

[6] E. C. Penning-Rowsell and J. B. Chatterton, "The benefits of flood alleviation: a manual of assessment techniques," *Geographical Journal*, vol. 145, no. 3, pp. 951–952, 1977.

[7] D. J. Parker, C. H. Green, and P. M. Thompson, *Urban Flood Protection Benefits: A Project Appraisal Guide*, Gower Technical Press, England, UK, 1987.

[8] C. Scawthorn, N. Blais, H. Seligson et al., "HAZUS-MH flood loss estimation methodology. I: overview and flood hazard characterization," *Natural Hazards Review*, vol. 7, no. 2, pp. 60–71, 2006.

[9] C. Scawthorn, P. Flores, N. Blais et al., "HAZUS-MH flood loss estimation methodology. II. Damage and loss assessment," *Natural Hazards Review*, vol. 7, no. 2, pp. 72–81, 2006.

[10] M. Hürlimann, D. Rickenmann, V. Medina, and A. Bateman, "Evaluation of approaches to calculate debris-flow parameters for hazard assessment," *Engineering Geology*, vol. 102, no. 3-4, pp. 152–163, 2008.

[11] H.-Y. Liao, T.-H. Chang, A.-P. Wang, and B.-W. Cheng, "Fuzzy comprehensive assessment of typhoon flood," *WSEAS Transactions on Environment and Development*, vol. 4, no. 3, pp. 257–266, 2008.

[12] Y. Chen, H. Zhou, H. Zhang, G. Du, and J. Zhou, "Urban flood risk warning under rapid urbanization," *Environmental Research*, vol. 139, no. 5, pp. 3–10, 2015.

[13] J.-W. Lin, C.-W. Chen, and C.-Y. Peng, "Potential hazard analysis and risk assessment of debris flow by fuzzy modeling," *Natural Hazards*, vol. 64, no. 1, pp. 273–282, 2012.

[14] M. Karamouz and S. Nazif, "Reliability-based flood management in urban watersheds considering climate change impacts," *Journal of Water Resources Planning and Management*, vol. 139, no. 5, pp. 520–533, 2013.

[15] J. Yazdi and S. A. A. S. Neyshabouri, "A simulation-based optimization model for flood management on a watershed scale," *Water Resources Management*, vol. 26, no. 15, pp. 4569–4586, 2012.

[16] L. Song, S. Zhao, W. Liao, and Z. Wang, "Neural network application based on GIS and Matlab to evaluation of flood risk," in *Proceedings of the International Conference on Remote Sensing, Environment and Transportation Engineering (RSETE '13)*, pp. 296–299, Nanjing, China, July 2013.

[17] Z.-X. Ding, J.-R. Li, and L. Li, "Method for flood submergence analysis based on GIS grid model," *Journal of Hydraulic Engineering*, no. 6, pp. 56–60, 2004 (Chinese).

[18] H. Qi, P. Qi, and M. S. Altinakar, "GIS-based spatial Monte Carlo analysis for integrated flood management with two dimensional flood simulation," *Water Resources Management*, vol. 27, no. 10, pp. 3631–3645, 2013.

[19] J. X. Li and S. L. Su, "Calculation model of water pollution induced economic loss for river basin," *Journal of Hydraulic Engineering*, vol. 34, no. 10, pp. 68–74, 2003 (Chinese).

[20] J. R. Li, Z. X. Ding, S. F. Huang, and Y. L. Hu, "Research of flood and waterlogging loss assessment model based on spatial distribution social-economic database," *Journal of China Institute of Water Resources and Hydropower Research*, vol. 1, no. 2, pp. 104–110, 2003 (Chinese).

[21] J. J. Yu, X. S. Qin, and O. Larsen, "Joint Monte Carlo and possibilistic simulation for flood damage assessment," *Stochastic Environmental Research and Risk Assessment*, vol. 27, no. 3, pp. 725–735, 2013.

[22] M. Chen, F. Zhou, J. Ma, G. Chen, H. Ni, and Y. Hu, "Water-induced disaster damage function and flood and water-logging damage assessment," *Journal of Hydraulic Engineering*, vol. 46, no. 8, pp. 883–891, 2015.

[23] P. P. Pan, G.-S. Yang, W.-Z. Su, and X.-X. Wang, "Impact of land use change on cultivated land productivity in Taihu Lake Basin," *Scientia Geographica Sinica*, vol. 35, no. 8, pp. 990–998, 2015 (Chinese).

[24] X. Jiabi, P. Sayers, S. Dongya, and Z. Hanghui, "Broad-scale reliability analysis of the flood defence infrastructure within the Taihu Basin, China," *Journal of Flood Risk Management*, vol. 6, no. 1, pp. 42–56, 2013.

[25] X. B. Xu and G. S. Yang, "Spatial and temporal changes of multiple cropping index in 1995–2010 in Taihu Lake Basin, China," *Transactions of the Chinese Society of Agricultural Engineering*, vol. 29, no. 3, pp. 148–155, 2013 (Chinese).

[26] X. T. Cheng, E. P. Evans, H. Y. Wu et al., "A framework for long-term scenario analysis in the Taihu Basin, China," *Journal of Flood Risk Management*, vol. 6, no. 1, pp. 3–13, 2013.

[27] L. Liu, Z. X. Xu, N. S. Reynard, C. W. Hu, and R. G. Jones, "Hydrological analysis for water level projections in Taihu Lake, China," *Journal of Flood Risk Management*, vol. 6, no. 1, pp. 14–22, 2013.

[28] J. M. Wicks, C. Hu, M. Scott, L. Chen, and X. Cheng, "A broad scale model for flood simulation in the Taihu Basin, China," *Journal of Flood Risk Management*, vol. 6, no. 1, pp. 33–41, 2013.

[29] E. C. Penning-Rowsell, W. Yanyan, A. R. Watkinson, J. Jiang, and C. Thorne, "Socioeconomic scenarios and flood damage assessment methodologies for the Taihu Basin, China," *Journal of Flood Risk Management*, vol. 6, no. 1, pp. 23–32, 2013.

[30] C. Q. Yu, J. W. Hall, X. T. Cheng, and E. P. Evans, "Broad scale quantified flood risk analysis in the Taihu Basin, China," *Journal of Flood Risk Management*, vol. 6, no. 1, pp. 57–68, 2013.

[31] J. W. Hall, R. J. Dawson, P. B. Sayers, C. Rosu, J. B. Chatterton, and R. Deakin, "A methodology for national-scale flood risk assessment," *Proceedings of the Institution of Civil Engineers: Water & Maritime Engineering*, vol. 156, no. 3, pp. 235–247, 2003.

[32] O. Hoes and W. Schuurmans, "Flood standards or risk analyses for polder management in the Netherlands," *Irrigation & Drainage*, vol. 55, supplement 1, pp. S113–S119, 2006.

[33] J. Hall and D. Solomatine, "A framework for uncertainty analysis in flood risk management decisions," *International Journal of River Basin Management*, vol. 6, no. 2, pp. 85–98, 2008.

[34] Y.-L. Ou and H.-Y. Wu, *The Taihu Lake Basin Flood in 1999*, China Water Power Press, Beijing, China, 2001 (Chinese).

[35] K. M. De Bruijn, "Resilience and flood risk management," *Water Policy*, vol. 6, no. 1, pp. 53–66, 2004.

Hindawi Publishing Corporation
Advances in Meteorology
Volume 2016, Article ID 6408319, 8 pages
http://dx.doi.org/10.1155/2016/6408319

Research Article

A Method to Assess Localized Impact of Better Floodplain Topography on Flood Risk Prediction

Guy J.-P. Schumann[1,2] and Konstantinos M. Andreadis[3]

[1]*Remote Sensing Solutions, Inc., Monrovia, CA 91016, USA*
[2]*School of Geographical Sciences, University of Bristol, Bristol BS8 1SS, UK*
[3]*NASA Jet Propulsion Laboratory, California Institute of Technology, Pasadena, CA 91109, USA*

Correspondence should be addressed to Guy J.-P. Schumann; gjpschumann@gmail.com

Received 23 January 2016; Revised 3 May 2016; Accepted 17 May 2016

Academic Editor: Maoyi Huang

Many studies have highlighted the need for a higher accuracy global digital elevation model (DEM), mainly in river floodplains and deltas and along coastlines. In this paper, we present a method to infer the impact of a better DEM on applications and science using the Lower Zambezi basin as a use case. We propose an analysis based on a targeted observation algorithm to evaluate potential data acquisition subregions in terms of their impact on the prediction of flood risk over the entire study area. Consequently, it becomes trivial to rank these subregions in terms of their contribution to the overall accuracy of flood prediction. The improvement from better topography data may be expressed in terms of economic output and population affected, providing a multifaceted assessment of the value of acquiring better elevation data. Our results highlight the notion that having higher resolution measurements would improve our current large-scale flood inundation prediction capabilities in the Lower Zambezi by at least 30% and significantly reduce the number of people affected as well as the economic loss associated with high magnitude flooding. We believe this procedure to be simple enough to be applied to other regions where high quality topographic and hydrodynamic data are currently unavailable.

1. Introduction

Topographic information in the form of a digital elevation model (DEM) is required for many environmental process models and applications. In many cases, the accuracy of a DEM is determining the performance of the model applied and the success of the application. Different technologies exist to acquire land elevation, often with varying degrees of accuracy and precision depending on the technology and resolution used. Remote sensing is commonly used to measure topography and instruments typically include altimeters (radar or LiDAR), synthetic aperture radar (SAR) interferometry, and photogrammetry from optical imagery; even unmanned aerial vehicles (UAV) are being used more recently to acquire DEMs. Vertical errors can range from several meters, typical for satellite DEM technology, for example, from the Shuttle Radar Topography Mission (SRTM, http://www2.jpl.nasa.gov/srtm/) or ASTER, down to the decimeter in the case of airborne LiDAR, airborne photogrammetry, and also novel airborne single-pass SAR interferometry as recently demonstrated by Schumann et al. [1].

Although accurate topography is desirable and in many cases a prerequisite for successful modeling, it is often not available at the required accuracy level and resolution for many areas around the world. As argued by Schumann et al. [2], there is a need for a higher accuracy (LiDAR-type) global DEM than currently available, particularly for mapping and predicting natural hazards such as flooding in developing countries that are often deprived but in need of a high quality DEM.

For instance, Mozambique (SE Africa) comprises a large flood-prone region in the downstream part of the Zambezi River Basin (ZRB), including a vast delta ecosystem and a number of important wetlands. Human activities, mostly related to hydroelectric power generation and agriculture,

have led to considerable alteration of the basin's hydrology and (natural) flooding pattern [3]. High magnitude flooding in the region happens regularly in the monsoon season but in some cases the impact is exacerbated through dam release operations such as, for instance, during the devastating floods of 2000. According to EM-DAT (http://www.emdat.be/, the Centre for Research on the Epidemiology of Disasters' Emergency Events Database), over the last 20 years (1995–2015), there have been more than 150 flood occurrences within the ZRB, affecting over 17 million people in total and causing total damage of over $1 billion US dollars, with single events being able to affect more than a million people at a time and many millions of US dollars in damage. These figures are alarming, even more so since many ZRB countries do not have any effective flood risk management plan in place and do only have very limited flood forecasting capabilities [4], and hence setting up some capabilities to improve current flood risk management in the ZRB countries, albeit with limited means and considerable efforts, is desperately needed.

In this context, Schumann et al. [5] demonstrated the value of remotely sensed data to build, calibrate, and validate a large-scale 2D hydrodynamic LISFLOOD-FP model (operating on a regular grid where water flow is simulated by solving the inertial momentum equation through a single explicit finite difference scheme; see [6]) forced with forecast flood flows to predict floodplain inundation depth and extent in the Lower Zambezi. In conclusion, they noted that although first efforts are encouraging, considerable improvements in the modeling, forcing data, and boundary conditions are needed to achieve greater forecasting capabilities, among which collecting finer resolution and better accuracy floodplain topography was considered particularly important. About 1000 km of river flow length and a floodplain area of around 40,000 km^2 were considered in this study (Figure 1). According to a simulation with the LISFLOOD-FP model of Schumann et al. [5], a 1 : 10,000 return period flow event estimated at ~30,000 m^{3}s^{-1} [7] would inundate approximately 8,000 km^2 of floodplain. These are large areas to cover with any airborne platform for high resolution topographic mapping which may render the cost of aircraft operation and data acquisition and processing prohibitive. However, the acquisition of better floodplain topography in the lower portion of the ZRB has the potential to significantly improve prediction and management of flood hazard and risk in the region, particularly Mozambique. Consequently, prioritization of the areas of data acquisition would help optimize operations such as flight lines and management of resources.

In this paper, we present a method to objectively identify areas for DEM acquisition based on floodplain hydrodynamics. We demonstrate that the method intrinsically pinpoints locations where a (flood forecasting) model would benefit most from better boundary condition data, in this case higher resolution floodplain topography. We further illustrate that, by including auxiliary datasets such as economic and population data, one can improve not only the selection of areas but potentially also flood risk management for those locations.

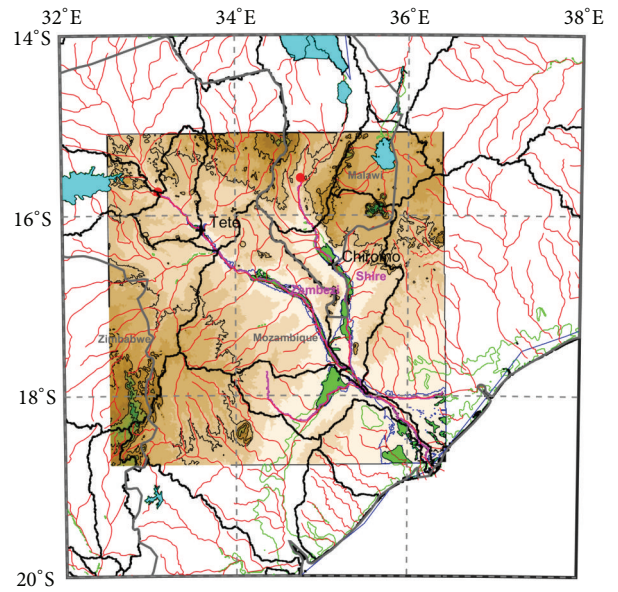

Figure 1: Map of modeling domain. Land elevations from SRTM are shown in shades of brown, the two main rivers (Zambezi and Shire) are shown in pink, and the inflow locations are depicted by red dots. The flooded area outline of the 1 : 10,000 year event is shown in blue. Large reservoirs are colored with cyan, wetlands are in green, and other rivers in the region are in red.

In the next section, we describe the method, followed by a brief section of results and discussion and finally a conclusion section.

2. Methods

2.1. Estimating the Impact of Better Topography on Flood Hazard Prediction. The impact of better floodplain topography, for example, acquired, for instance, by airborne LiDAR or InSAR as opposed to SRTM, on the estimation of flood hazard variables (e.g., flooded area) can be assessed using the targeted observation method proposed by Andreadis and Schumann [8]. This involves the ingestion of measurements or observations over a "targeted area" into a hydrodynamic model and the estimation of flooded area (in our case) without rerunning the model. An optimal estimation algorithm (1) exploits the statistical relationships between variables to make a prediction. The cost function that measures the reduction in the prediction error due to the assimilation of new measurements, that is, the measurement impact, is defined as

$$J = \frac{1}{2}\left(e_{t|0}^{T} e_{t|0} - e_{t|-1}^{T} e_{t|-1}\right), \quad \text{where } e_{t|0} = \overline{x}_{t|0}^{f} - \overline{x}_{t}^{a},\ e_{t|-1} = \overline{x}_{t|-1}^{f} - \overline{x}_{t}^{a}. \tag{1}$$

The cost functional J is the difference of the squared errors between the model run that benefits from the new measurements and the model that does not benefit from any new measurements being assimilated. Variable $\overline{x}_{t|-1}^{f}$ is the model prediction without any assimilation and $\overline{x}_{t|0}^{f}$ is the prediction

with the new measurement assimilated. The verification $\overline{x}_t^a$ at time t can be either an actual measurement or the analysis at time t, implicitly assumed to be more accurate than both model runs. Applying the Local Ensemble Transform Kalman Filter (LETKF) analysis formulation after Hunt et al. [9], the cost functional J can be computed to represent the sensitivity of a prediction skill to the measurements being assimilated. For more details on the derivation of J in a LETKF sensitivity experiment, the reader is referred to Andreadis and Schumann [8] as well as Liu and Kalnay [10].

In our case, applying this method means that the impact (expressed by J) of higher resolution topography on the simulated flooded area can be estimated. Since better topography measurements have not actually been acquired (yet) over the Lower Zambezi, the impact assessment is simulated. Assuming that the 1 km resolution inundation forecast model by Schumann et al. [5] represents current modeling capabilities at large scales (see also Sampson et al. [11] for a state-of-the-art global simulation of inundation based on the same model type) and that existing elevation datasets over large scales can be obtained at a spatial resolution of 90 m or less, we ran a 2D LISFLOOD-FP simulation using the 90 m SRTM-DEM in order to emulate the minimum difference that a higher resolution floodplain topography would most likely achieve.

Since the amount and timing of floodplain inundation are largely determined by in-channel water level and floodplain topography controls floodplain flow and thus inundation extent, we sampled water levels from the 90 m model output (based on subreaches determined from a first-order hydraulic analysis; see Section 3 for more details) and assimilated those in the 1 km baseline model. Note that better topography would of course also improve the estimation of river bank heights which control the timing and location of flood waters overtopping, particularly in the 1 km model version since LISFLOOD-FP SGC inverts bank heights to estimate channel bathymetry using hydraulic geometry [12].

We then use the simulated flooded area from the 1 km model (before and after assimilation) and compare that to the inundated area of the 90 m model which represents the verification. In other words, for the experimental design, both model versions are based on the SRTM-DEM topography but at two different spatial resolutions: (i) the 1 km resolution model that represents the "open-loop" simulation as well as the resulting model after assimilation and (ii) the 90 m model resolution that serves as the "verification" model for the 1 km models. Following this setup, the proposed targeted observation algorithm allows estimating the flooded area over the entire model reach that would be produced by a model utilizing better topography over the particular subregion (i.e., location of assimilation) only, and J is a direct measure of the improvement in prediction achieved.

2.2. Estimating the Associated Socioeconomic Impact. Estimating the actual costs related to flood risk, that is, flood economic impact combined with flood hazard, may prove difficult in regions that have only limited amounts of relevant local data available, such as stage-damage curves and information on residential and nonresidential building, agricultural and industrial activities, and transportation. The unavailability and/or the poor quality of such socioeconomic data, primarily in developing countries, is often hindering efforts to understand and link environmental disasters to actual impacts on economy and society. Nonetheless, a number of approaches have been proposed more recently that use other measurements as proxies for economic statistics. One promising approach uses satellite-based luminosity, which measures nighttime lights to statistically characterize population, poverty, and economic productivity (e.g., [13–15]). Measurements of nighttime lights are acquired from satellite sensors at relatively high spatial resolutions (1 km) globally and have been successfully used in the aforementioned studies showing strong correlations with economic activity, measured by the Gross Domestic Product (GDP), for instance. Here, we used nighttime image data from the US Department of Defense satellites for 2012 (most recently available) that contain lights from cities, towns, and locations with permanent lighting.

GDP data over the Lower Zambezi region were obtained from the G-Econ project (http://gecon.yale.edu/), which provides global economic data at ~100 km resolution. Although these data are valuable, their coarse resolution can make the economic analysis of flood impacts difficult. Therefore, the GDP data were downscaled using the much finer resolution luminosity data. The latter were first aggregated to a 100 km grid to match the resolution of the GDP data grid, and then a ratio of GDP to luminosity was calculated. This ratio was then downscaled to 1 km by using a nearest-neighbor interpolation, and finally a fine resolution GDP value was calculated by multiplying the downscaled ratio with the original 1 km luminosity data.

Additionally, data on population density for 2015 (at a ~4 km resolution) were acquired from the NASA Socioeconomic Data and Applications Center (SEDAC, http://sedac.ciesin.columbia.edu/) and integrated with the overall analysis, which as a result now provides a multifaceted assessment (i.e., physical and socioeconomic) of the full value of acquiring better elevation data.

3. Results and Discussion

As described in Section 2, we simulated flood inundation in the Lower Zambezi with a 1 km resolution LISFLOOD-FP hydrodynamic model. This model is identical to that of Schumann et al. [5] and we assume for the purpose of this study that it represents current flood modeling capabilities at large scales. The model is LISFLOOD-FP [6] in subgrid channel (SGC) mode [12] forced with forecast flood flows for the Zambezi and Shire Rivers simulated by the Variable Infiltration Capacity (VIC) distributed hydrology model, which is conditioned on meteorological ensemble forecast (ENS) data from ECMWF. For the complete setup, modeling chain, and model calibration, the reader is referred to Schumann et al. [5]. As in their study, we simulated the 2007 flood event and validation with a Landsat image shows a flood edge agreement to within one model resolution (mean distance to observed flood edge: ~1.5 km).

As outlined in Section 2, we build a 90 m version of a LISFLOOD-FP model that served as verification of the

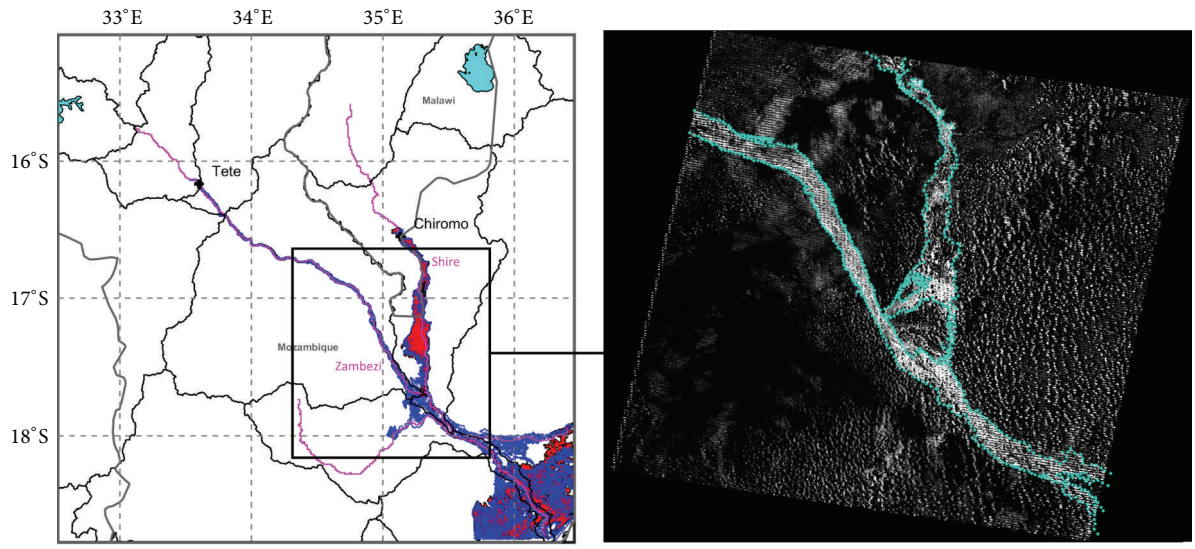

(a) (b)

Figure 2: Map of the area (a) shows the flooded area simulated by the 1 km baseline model (red) and the 90 m verification model (blue). (b) depicts the corresponding Landsat image (of the 2007 flood event shown in white) and derived flood edge (depicted by blue dots).

targeted observation algorithm. For this model, we used the 90 m SRTM and deepened the channel area by interpolating the bathymetry simulated by the 1 km SGC model, allowing a full 2D inundation simulation at 90 m resolution. Figure 2 shows the flooded area from both models for the 2007 event as well as the Landsat image used for validation. Unsurprisingly, the extent of the 90 m model matches the Landsat flood edge more closely than that of the 1 km model with a mean distance to flood edge of ~220 m, at least four orders of magnitude better than the 1 km model.

For the targeted observation analysis, we simulated the 1 : 10,000 year event shown in Figure 1 to ensure we inundate most of the rivers' natural floodplains. Furthermore, since airborne data acquisition is likely to cover a spatial extent smaller than that of the entire floodplain area in the domain shown in blue in Figure 1, we defined a regional sampling strategy based on first-order in-channel hydraulics. We define a subreach based on bank height variations from the 90 m SRTM-DEM for a channel length (in flow distance) of constant river width taken from Andreadis et al. [16]. In addition, we computed the linear gradient of the SRTM-derived thalweg (i.e., the kinematic wave form) and compared this to subreach characteristics (Figure 3), which constitutes a first step at understanding reach behavior and can help interpret the results of our targeted observation analysis.

Figure 3 shows the result of the first-order in-channel hydraulic analysis. Figure 3(a) shows the SRTM bank height variations along the river chainage and their deviation from a linear approximation of each subreach (red dashed lines). Also shown is a kinematic wave form along the entire main stem analyzed (blue line). Figure 3(b) shows for each subreach the deviation from this simple kinematic flow line. Interesting to note is that we can now observe those subreaches that exhibit a more diffusive channel flow behavior, that is, those that have a standard deviation from the kinematic wave approximation (along the entire river) greater than 2σ (two standard deviations), for instance.

Of course, only subreaches with an associated inundation area (according to the 1 : 10,000 year event) are used (Figure 4) to set the sampling location of in-channel water levels from the 90 m model to be assimilated in the 1 km flood model.

Subsequently, we applied (1) to assess the impact better measurements of a river and floodplain subreach will have on the overall (global) reach being considered. Table 1 shows the results of the targeted observation analysis along with the associated economic costs of flood loss and monetary value gained from higher resolution (topography) measurements.

Each row in Table 1 corresponds to an individual region being the only one measured. The global improvement in flooded area is the improvement in prediction of flooded area for the entire model domain, while the regional improvement is the flooded area estimation improvement achieved localized for that region. For example, if better topography measurements were only acquired over subregion 1 and less accurate topography (i.e., SRTM-DEM) was used for the rest of the basin, there would be a 24% improvement in flooded area prediction relative to only using SRTM data. Moreover, the improvement that would be achieved for subregion 1 is 77.8% in terms of flooded area. It can be deduced that the percentage of improvement essentially describes the extent to which more accurate flooded area prediction is governed by topography, with the remainder being attributed to other hydraulic controls such as boundary conditions, for example, inflows. If all the latter were known and accurate, the regional error in flooded area prediction can be expected to reduce significantly.

Our analysis shows that having better topography measurements even only for a limited number of regions would improve prediction of flood hazard along the entire Zambezi main stem considerably, albeit with some uncertainty.

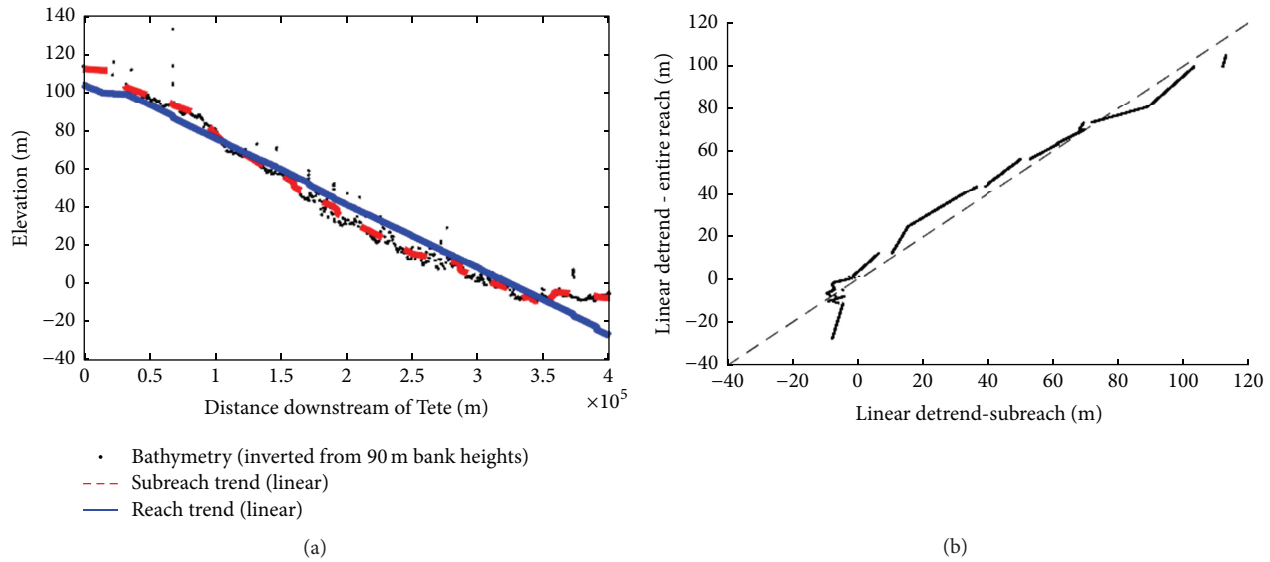

FIGURE 3: The graph (a) shows SRTM bank height variations (at 90 m resolution) along the river chainage, their deviation from a subreach linear approximation (red dashed line), and the kinematic wave along the entire main stem of the Zambezi River (blue line). The plot (b) illustrates the deviation of each subreach from the kinematic wave flow profile.

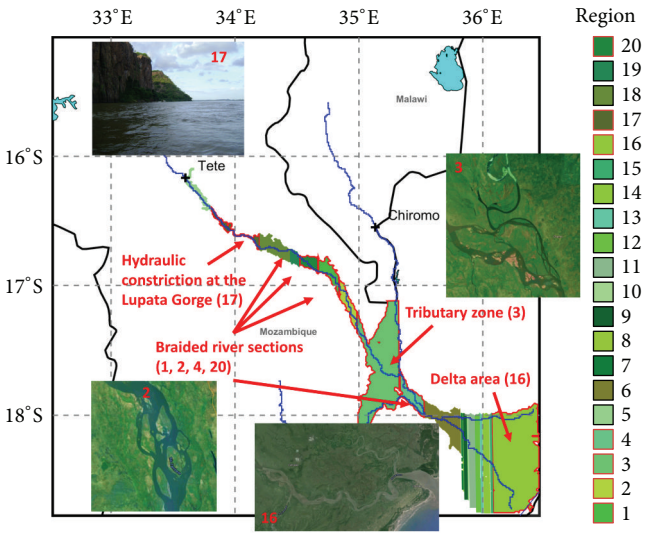

FIGURE 4: Map of individual subreaches and their floodplains, that is, regions of assimilation (colors are at random). Subreaches of hydraulic complexity (defined as $>2\sigma$ from the kinematic wave form; see text for details) are depicted with a red outline and annotated. Note that the flooded area shown for each subreach is based on a 1 : 10,000 year flow return flood simulation, overlain as a blue outline on the SRTM topography in Figure 1. Photos are taken from Google Earth.

Unsurprisingly, subreaches in which flow is more complex, that is, sections with a high standard deviation from the kinematic wave form (as defined earlier), all yield regional and global improvements much greater than 20% in flooded area prediction, if better measurements became available for those regions. The only region that achieves only minimal improvement is region 17, which is expected since this subreach runs through the Lupata Gorge (see Figure 4) and hence better height measurements would only marginally improve predictions in this river section.

The significance of these results is further reinforced by the socioeconomic analysis conducted (Table 1) that highlights the notion that obtaining better measurement for each region results in a total global improvement (i.e., along the entire river) of 30% in flooded area prediction. As a direct consequence, a difference of more than 150,000 in people affected can be achieved and economic losses can be reduced by nearly $2 billion (for a 1 : 10,000 year event), contingent of course on the accuracy of the socioeconomic input data used. Nonetheless, to put these numbers in context, the devastating 2000 flood events (orders of magnitude smaller than the 1 : 10,000 year event simulated here) caused total damage of $0.5 billion and affected more than 5 million people in both the ZRB and Limpopo basin, according to EM-DAT.

An important point of this study is that although the targeted observation analysis (as proposed by Andreadis and Schumann [8]) can be used to assess the impact new measurements of important variables have on the prediction of flood hazard and although we showed how inclusion of socioeconomic data can augment that analysis, there is the substantial caveat that the verification model in our case was only based on higher resolution (90 m) SRTM topography and not on high accuracy elevation data, for example, from LiDAR or new InSAR technology [1]. Nevertheless, we believe this analysis to be worthwhile and suggest this type of study to be repeated for other large river areas in particular in countries deprived of high resolution floodplain DEMs so that the case for a better global DEM [2] can be supported.

As a final note, an analysis such as the one presented here should be combined with industry standard guidelines for LiDAR-type DEM acquisition. Having LiDAR-type floodplain height data over flood-prone areas would allow

Table 1: Results of the proposed targeted observation analysis. Note that the analysis is based on a 1 : 10,000 year event. Furthermore, we wish to note that the economic impact analyzed here is only from inundation differences and does not include any other changes with potential economic impact such as infrastructure planning or climate change adaptation strategies, for instance.

Region of assimilation	Area (km^2)	Global improvement in flooded area prediction	Regional improvement in flooded area prediction	Population (2015 UN adjusted)	Difference in people affected	Regional loss of economic cost (2005 GDP in billion USD)	Global economic gain from better regional flood prediction (2005 GDP in billion USD)
01	237.6	24.0%	77.8%	4,324	3,364	0.000	1.511
02	233.9	25.3%	40.0%	7,581	3,032	0.400	1.593
03	2,441.3	29.1%	44.6%	167,029	74,495	0.103	1.832
04	309.1	27.7%	0.5%	6,819	34	1.511	1.744
05	123.3	25.8%	28.4%	23,037	6,542	0.896	1.624
06	553.4	13.1%	14.3%	7,600	1,087	0.144	0.825
07	25.1	30.4%	17.8%	494	88	0.000	1.914
08	60.7	18.1%	30.6%	1,070	327	0.000	1.139
09	138.5	32.5%	32.0%	2,462	788	0.000	2.046
10	101.2	26.0%	32.0%	1,906	610	0.000	1.637
11	348.4	27.1%	65.7%	7,233	4,752	1.670	1.706
12	240.9	22.5%	29.1%	4,950	1,441	1.571	1.417
13	99.4	30.7%	43.6%	2,317	1,010	0.000	1.933
14	357.2	24.7%	38.5%	7,508	2,890	0.000	1.555
15	79.3	26.0%	26.6%	1,619	431	0.000	1.637
16	3,237.5	23.3%	48.4%	98,560	47,703	0.000	1.467
17	165.5	3.4%	26.5%	3,825	1,014	0.000	0.214
18	294.8	13.6%	60.5%	7,967	4,820	0.000	0.856
19	71.9	25.3%	47.8%	2,332	1,115	0.000	1.593
20	154.2	30.6%	44.9%	2,394	1,075	0.000	1.926
Total	*9,273.1*	*30.8%*	*N/A*	*361,027*	*156,618*	*6.295*	*1.939 (average)*

building a better 2D flood inundation model, at least for targeted regions of interest, thereby allowing more detail in the following:

(i) Understanding of local to regional floodplain-channel water storage and fluxes (including wetlands) and timing of flood wave thus achieving better flood forecasting.

(ii) Flood hazard/risk mapping for agricultural and urban areas.

(iii) Flood zone mapping associated with return period flows for assisting urban and infrastructure planning and establishing legal guidelines.

(iv) Retrieving building footprints for urban planning.

(v) Ecological and environmental flow modeling in important wetland areas, including habitat protection as well as the derivation of water quality and health indicators based on flood inundation parameters (e.g., timing of inundation and amount of water stored in floodplains).

4. Conclusion

There is an obvious need for a better accuracy global DEM for floodplains and coastal areas [17]. In support of this, we presented results of a detailed analysis of the impact better measurement of floodplain topography would have on the prediction of flood hazard and associated socioeconomic risk. We used the Lower Zambezi River reach and the large-scale flood inundation model as developed by Schumann et al. [5] to illustrate our case. The procedure we propose is based on the targeted observation method after Andreadis and Schumann [8] which is essentially a sensitivity analysis of a Local Ensemble Transform Kalman Filter (LETKF) applied to localize the assimilation of observations or measurements. The sensitivity analysis allows one to quantify the exact impact the assimilation has locally as well as globally without the need to rerun any models, which considerably reduces the computational burden and thus appeals to large-scale applications.

For a 1 : 10,000 year flood event in the Lower Zambezi and focusing on the country of Mozambique, we showed that having higher resolution topography measurements available would improve our current large-scale flood inundation prediction capabilities in countries deprived of high quality DEMs by at least 30% and significantly reduce the number of people affected as well as the economic loss associated with high magnitude flooding. Although we showed considerable improvement in flood prediction for a low occurrence scenario, we believe higher accuracy topographic data would also largely improve model predictions for shorter return period events.

Although flood hazard prediction and risk analysis are difficult to perform accurately in areas that only have low resolution data available and despite the uncertainties that may arise from this limitation, we demonstrated the value of the proposed method and believe the procedure to be straightforward and simple enough to be applied to other regions. In doing so, the case for better topographic and hydrodynamic data becomes substantiated, particularly in developing nations where such data are currently often unavailable.

Competing Interests

The authors declare that they have no competing interests.

Acknowledgments

G. J.-P. Schumann and K. M. Andreadis' time was supported by a NASA THP grant (13-THP13-0042). Part of this research was carried out at the Jet Propulsion Laboratory, California Institute of Technology, under a contract with the National Aeronautics and Space Administration (NASA).

References

[1] G. J.-P. Schumann, D. Moller, and F. Mentgen, "High-accuracy elevation data at large scales from airborne single-pass SAR interferometry," *Frontiers in Earth Science*, vol. 3, no. 88, 2016.

[2] G. J.-P. Schumann, P. D. Bates, J. C. Neal, and K. M. Andreadis, "Technology: fight floods on a global scale," *Nature*, vol. 507, p. 169, 2014.

[3] R. Beilfuss and D. D. Santos, "Patterns of hydrological change in the Zambezi Delta, Mozambique," Working Paper 2, US Geological Survey, Program for the Sustainable Management of Cahora Bassa Dam and The Lower Zambezi Valley, 2001.

[4] WMO, "Regional consultation meeting on Zambezi river basin flood forecasting and early warning strategy and WMO Information System (WIS) and WIGOS pilot project," Final Report, WMO and USAID, Maputo, Mozambique, Africa, 2009.

[5] G. J.-P. Schumann, J. C. Neal, N. Voisin et al., "A first large-scale flood inundation forecasting model," *Water Resources Research*, vol. 49, no. 10, pp. 6248–6257, 2013.

[6] P. D. Bates, M. S. Horritt, and T. J. Fewtrell, "A simple inertial formulation of the shallow water equations for efficient two-dimensional flood inundation modelling," *Journal of Hydrology*, vol. 387, no. 1-2, pp. 33–45, 2010.

[7] Li-EDF-KP Joint Venture Consultants (Lahmeyer-Knight Peisold-Electricite de France), *Mepanda Uncua and Cahora Bassa North Project Simulation of Reservoir Operation and Energy Generation on Zambezi River*, Unidade Tecnica de Implentacao de Projectos Hidroelectricos, Maputo, Mozambique, 2000.

[8] K. M. Andreadis and G. J.-P. Schumann, "Estimating the impact of satellite observations on the predictability of large-scale hydraulic models," *Advances in Water Resources*, vol. 73, pp. 44–54, 2014.

[9] B. R. Hunt, E. J. Kostelich, and I. Szunyogh, "Efficient data assimilation for spatiotemporal chaos: a local ensemble transform Kalman filter," *Physica D: Nonlinear Phenomena*, vol. 230, no. 1-2, pp. 112–126, 2007.

[10] J. Liu and E. Kalnay, "Estimating observation impact without adjoint model in an ensemble Kalman filter," *Quarterly Journal of the Royal Meteorological Society*, vol. 134, no. 634, pp. 1327–1335, 2008.

[11] C. C. Sampson, A. M. Smith, P. B. Bates, J. C. Neal, L. Alfieri, and J. E. Freer, "A high-resolution global flood hazard model," *Water Resources Research*, vol. 51, no. 9, pp. 7358–7381, 2015.

[12] J. Neal, G. Schumann, and P. Bates, "A subgrid channel model for simulating river hydraulics and floodplain inundation over large and data sparse areas," *Water Resources Research*, vol. 48, no. 11, Article ID W11506, 2012.

[13] C. N. H. Doll, J.-P. Muller, and J. G. Morley, "Mapping regional economic activity from night-time light satellite imagery," *Ecological Economics*, vol. 57, no. 1, pp. 75–92, 2006.

[14] A. M. Noor, V. A. Alegana, P. W. Gething, A. J. Tatem, and R. W. Snow, "Using remotely sensed night-time light as a proxy for poverty in Africa," *Population Health Metrics*, vol. 6, article 5, 2008.

[15] W. Nordhaus and X. Chen, "A sharper image? Estimates of the precision of nighttime lights as a proxy for economic statistics," *Journal of Economic Geography*, vol. 15, no. 1, pp. 217–246, 2015.

[16] K. M. Andreadis, G. J.-P. Schumann, and T. Pavelsky, "A simple global river bankfull width and depth database," *Water Resources Research*, vol. 49, no. 10, pp. 7164–7168, 2013.

[17] A. L. Simpson, S. Balog, D. K. Moller, B. H. Strauss, and K. Saito, "An urgent case for higher resolution digital elevation models in the world's poorest and most vulnerable countries," *Frontiers in Earth Sciences*, vol. 3, pp. 1–2, 2015.

Hindawi Publishing Corporation
Advances in Meteorology
Volume 2016, Article ID 7159132, 11 pages
http://dx.doi.org/10.1155/2016/7159132

Research Article

A Multimethod Approach towards Assessing Urban Flood Patterns and Its Associated Vulnerabilities in Singapore

Winston T. L. Chow,[1,2] Brendan D. Cheong,[1] and Beatrice H. Ho[1]

[1] *Department of Geography, National University of Singapore, AS2, No. 03-01, 1 Arts Link, Kent Ridge, Singapore 117570*
[2] *Institute of Water Policy, Lee Kuan Yew School of Public Policy, National University of Singapore, 469C Bukit Timah Road, Wing A, Level 2, Oei Tiong Ham Building, Singapore 259772*

Correspondence should be addressed to Winston T. L. Chow; winstonchow@nus.edu.sg

Received 14 December 2015; Revised 5 April 2016; Accepted 23 May 2016

Academic Editor: Huan Wu

We investigated flooding patterns in the urbanised city-state of Singapore through a multimethod approach combining station precipitation data with archival newspaper and governmental records; changes in flash floods frequencies or reported impacts of floods towards Singapore society were documented. We subsequently discussed potential flooding impacts in the context of urban vulnerability, based on future urbanisation and forecasted precipitation projections for Singapore. We find that, despite effective flood management, (i) significant increases in reported flash flood frequency occurred in contemporary (post-2000) relative to preceding (1984–1999) periods, (ii) these flash floods coincide with more localised, "patchy" storm events, (iii) storms in recent years are also more intense and frequent, and (iv) floods result in low human casualties but have high economic costs via insurance damage claims. We assess that Singapore presently has low vulnerability to floods vis-à-vis other regional cities largely due to holistic flood management via consistent and successful infrastructural development, widespread flood monitoring, and effective advisory platforms. We conclude, however, that future vulnerabilities may increase from stresses arising from physical exposure to climate change and from demographic sensitivity via rapid population growth. Anticipating these changes is potentially useful in maintaining the high resilience of Singapore towards this hydrometeorological hazard.

1. Introduction

Since the mid-20th century, the gradual and extensive movement of people from rural (or undeveloped) to urban (developed) areas, combined with the physical consequences of this migration, has been a distinct feature of the Anthropocene epoch [1]. This *urbanisation* process has a remarkable global extent; since 2007, more than 50% of global populations reside in cities, and demographic projections indicate that urbanisation rates in major African and Asian cities over the next decade will continue to accelerate [2]. An obvious consequence is changes towards land use and land cover (LULC), which explicitly manifest through direct human modifications of various terrestrial surfaces (e.g., deforestation of forest biomes and damming of river channels). The clearest illustration of LULC conversion occurs within cities and other large urban agglomerations, where construction of buildings and roads and the activities of human economic activity directly but inadvertently affect climate properties such as near-surface temperature and wind-speed at local or regional spatial scales [3].

Apart from elevated temperatures observed within cities that is the ubiquitous urban heat island (UHI) effect [4], LULC change via urbanisation also alters hydrometeorological processes at both the surface and its overlying atmosphere. For instance, the UHI and increased roughness associated with cities vis-à-vis its rural surroundings, as well as with larger aerosol emissions from urban metabolism processes (i.e., through industrial and vehicular emissions), potentially influencing precipitation characteristics above cities. In several cases, these result in clear variations of frequency, magnitude, and spatial heterogeneity of urban-induced precipitation across city-wide [5] and regional scales [6]. At the surface, removal of vegetation and subsequent replacement

Figure 1: True colour map of Singapore in 2015 with location of Changi Airport meteorological station (the WMO station of record for Singapore) marked (source [36]).

by concrete and asphalt surfaces generally decrease urban soil porosity and permeability. Existing preurban watersheds and drainage networks may also be artificially altered and managed through either canalisation or the implementation of sewerage systems. Consequently, the net result on urban hydrology is that (i) reductions occur for local interception, infiltration, percolation, lag times, and storage through surface depressions within soil and (ii) increases in surface runoff volumes, peak flows, and flow variability ensue [7]. Greater urban sprawl with considerable soil sealing or surface "water-proofing" also corresponds with increases in urban flood risk; during high-intensity precipitation events, discharge and runoff volumes may exceed the capacity of canals and sewer systems, resulting in localised ponding or flash flood events. Further, the reduction in lag time likely reduces the effectiveness of advisories or warnings of flash floods towards populations residing in flood prone areas.

An extreme example of urbanisation can be seen in the equatorial (1°N 104°E) island city-state of Singapore (Figure 1). It is subject to a tropical rainforest Köppen *Af* climate with two distinct monsoon seasons, one in summer (typically June to August, with winds predominantly from South or Southwest) and one in winter (generally November to January, with mostly North-easterly winds) [8]. Rainfall is abundant with no distinct dry seasons (means of total annual precipitation ~2500 mm yr^{-1}; mean annual frequency of ~180 rain-days yr^{-1}). Since its independence in 1965, Singapore has underwent extensive conversion of its natural (i.e., lowland dipterocarp rainforest and coastal mangroves) and agrarian (i.e., small scale subsistence and plantation agriculture) LULC towards a metropolis in which 100% of its population reside in built-up areas. From 1955 to 1998, the proportion of (i) total farm area, (ii) marsh and tidal areas, and (iii) forest surface cover decreased from ~35% to <10% due to conversion to built-up urban surfaces throughout Singapore [4]. This alteration is also reflected in the southward land reclamation of its main island that has resulted in a substantial increase in land surface area by almost 25% since 1960 (Table 1).

Table 1: Change in total land area of Singapore from 1960 to 2014 (source [27]).

Year	Land area (km^2)	Population (millions)
1960	581.5	1.65
1965	581.5	1.89
1970	586.4	2.07
1975	596.8	2.26
1980	617.8	2.41
1985	620.5	2.74
1990	633.0	3.05
1995	647.5	3.52
2000	682.7	4.03
2005	697.9	4.27
2010	712.4	5.08
2014	718.9	5.47

Singapore's extensive urbanisation has been the focus of concerted study into the influence of LULC change on its climate, particularly in terms of UHI [9], and aerosol pollution [10]. Quantitatively, less investigation into its precipitation characteristics in an urban context exists, but past research has revealed some useful insights. For instance, changes

to the surface hydrological cycle from LULC variation was examined by Chatterjea [11]. She assessed how the removal of previous forested land cover in facilitating construction of buildings and roads led to significant increases of sediment and runoff generation at these newly cleared sites, especially with frequent short-duration, high-intensity rainstorms typical of its equatorial climate.

Other studies have utilised Singapore's relatively extensive network of meteorological stations (compared to other low-latitude cities), which enable detailed analysis at fine spatiotemporal resolutions. Mandapaka and Qin [12, 13] obtained 30 years of hourly and daily data over an island-wide network of 49 rain gauges to examine aspects of Singapore's rainfall through probability distributions and spatial correlations of station data, with the twin objectives of understanding the rainfall variability of Singapore over different spatial and temporal resolutions. The relatively good quality of precipitation data also can be utilised for modelling validation studies; Vaid [14] utilised WRF to examine the model's performance when simulating a June 2013 extreme rainfall event in Singapore. The model results indicated that the localised heavy precipitation resulted from interactions of synoptic-scale weather systems (e.g., the summer monsoon) with a well-developed mesoscale convective system (e.g., squall-line development due to regional topography).

Lastly, Beck et al. [15] comprehensively reviewed Singapore's precipitation regime based on data from 30 stations from 1980 to 2010 and found that daily and seasonal variations are affected by changes in the El Niño Southern Oscillation (ENSO) teleconnection. During El Niño years, notable decreases in annual precipitation are likely to occur during the summer (Southwest) monsoon period, as in the case of an extreme El Niño event that took place in 1997. Conversely, during La Niña years, seasonal rainfall tends to increase, with more intense precipitation events occurring in the morning regional squall events versus typical afternoon convection storm events. They also noted a recent and significant trend towards more extremes in rainfall events; these occurred through increases both in the frequency of large storms and in the mean rainfall intensity. This finding concords with a previous study commissioned by a governmental agency, the Ministry of Environment and Water Resources (MEWR), which examined the variability of extreme rainfall in Singapore over the corresponding time period [16].

Of particular interest is the impact of climate change towards projected variations in Singapore's precipitation regime. Globally, a warmer climate unequivocally leads to increased water vapour, which is confirmed by fundamental physical climatology, empirical observational data, and numerical climate model simulations [17]. The increased water vapour leads to more intense precipitation events even if total annual precipitation is slightly reduced [18]. Within Southeast Asia, the extent of assessing changes in regional precipitation is stymied by generally poor spatial resolution of observational stations, but available data indicate that more (less) intense storms occur during the wet winter (dry summer) monsoon season [19]. The basis of future changes in regional precipitation is relatively more robust. Projected medium-term increases in monsoonal precipitation extremes based on the Coupled Model Intercomparison Project Phase 5 (CMIP5) results are very likely in Southeast Asia [20], with 95% of models indicating significant increases in frequencies of heavy monsoonal rainfall events.

Recently, there have been attempts to dynamically downscale selected CMIP5 global simulations with the HadGEM3-RA regional climate model. This is to examine local impacts of climate change centred over Singapore based on the Representative Concentration Pathway (RCP) 8.5 and 4.5 scenarios [21]. While average annual rainfall in Singapore until 2100 will likely be dominated by natural variability under both RCP scenarios, most of the modelling simulations do suggest an increasing trend in the occurrence of both intensity and frequency of heavy precipitation events, as well as an upward (downward) trend in seasonal mean rainfall during the wet winter (dry summer) monsoons [22].

While the potential impacts arising from lowered seasonal precipitation and dry spells/drought in Singapore have been discussed [23], there appears to be little analysis done so far about the changing patterns of flood events in Singapore with respect to urbanisation and associated variations in precipitation patterns. When altered hydrometeorological processes are combined with changes in socioeconomic conditions implicit within Singapore's prodigious urbanisation rate, the resulting impacts on the system's *vulnerability* (i.e., the degree to which the system is susceptible to a particular hazard) become of interest with respect to overall urban sustainability. In particular, there is importance in understanding how the changing vulnerability of urban areas—which is comprised by (i) its physical exposure towards changing precipitation patterns, as well as the city's (ii) sensitivity and (iii) capacity to adapt, derived from its socioeconomic characteristics—develops over space and time [24]. The corollary to understanding the patterns of vulnerability would be enhancing the urban *resilience* to natural hazards (i.e., the capacity of a city to withstand shock or stress arising from extreme hydrometeorological events); for instance, it can be done by adapting towards the danger through sound decision-making [25]. Municipal governments that do not fare well in responding to the implicit risks often have inefficient and ineffective strategies that heighten their population's vulnerability, for example, for flood vulnerability in the Asian city of Taipei [26].

In this context, an account of how Singapore has responded towards past changes in urban floods that is framed through its altered urban vulnerability could potentially be useful exemplars for other cities to consider and potentially apply in the context of a changing urban and global climate. Thus, in this paper we investigate how patterns of flooding in Singapore have varied over time through a novel, multimethod approach. First, we document the history of Singapore's flooding through examining (i) its precipitation data and (ii) archival newspaper and governmental records; in particular, we are interested in documenting if changes are apparent in the frequency of flash floods or in the reported impacts of floods towards Singapore society. Second, in the context of urban vulnerability, we examine and discuss the projected impacts of flooding that may arise based

on future trajectories of urban development in Singapore, in conjunction with forecasted projections of precipitation variations at various spatial scales.

2. Methodology

In documenting the historical extent of flooding in Singapore, we utilised several data sources. First, we obtained hourly climate data from 1956 to 2015 recorded at the meteorological station located at Changi Airport (sited on the eastern end of Singapore) that are provided by the National Climatic Data Center (NCDC). Since January 1984, this station has been designated as the official World Meteorological Organisation (WMO) climate station for Singapore. We subsequently derived precipitation intensity data for analysis of relevant storms that are directly related to reported flood events. Second, we examined archival data from local newspapers and governmental websites pertaining to floods in Singapore. In particular, we examined newspaper reports about floods from the local English daily newspaper of record (*The Straits Times*), which was originally established in 1845 and has articles that are readily accessible through a large digital archive [28].

This large newspaper archive enabled us to search for flood events in Singapore deemed noteworthy enough to be reported for public interest, such as floods resulting in or causing human casualties, property damage, and disruption to traffic due to road inundation, landslides, or fallen trees from storms. While there are potential archival data issues related towards progressive increases in newspaper space that may enable more reports of floods in recent years (i.e., likely underreporting of floods in the past), we opine that this approach enables flood analyses directly relevant towards examining societal vulnerability and resilience to this hazard, as opposed to only examining storms of large intensities in the Changi precipitation data that may not translate to floods with significant societal impact. Nonetheless, we acknowledge this limitation especially in the low reports of floods that are apparent prior to 1965.

We subsequently obtained and collated a total of 262 archived articles from December 1892 until December 2015 using the search term "flood+Singapore." If reported, relevant hydrometeorological information such as (i) location and areal extent of the flood, (ii) tidal information, (iii) flood depth, and (iv) rainfall amounts from these events were recorded; however, derivation of hourly rainfall depth and intensity based on these flood reports was problematic for two reasons. Firstly, articles did not clearly indicate durations of each rainfall or storm event: that is, only total rainfall amounts are reported. Secondly, some of the reported rainfall data were from weather stations that were closer in distance to where the flood impacts occurred, rather than from Changi. Nonetheless, we compared the reported storm magnitude for recent floods that fall within the recorded data range at Changi to ascertain if the precipitation causing the flood was also measured at the WMO station of record. Indications of human injury and property damage mentioned in the database of newspaper reports, as well as if the flood was explicitly described as a "flash flood," were also documented.

To assess the quality of the constructed flood database, we also examined publically available records of recent (post-2000) floods maintained by the Public Utilities Board (PUB) at their website [29]. In Singapore, the PUB is the national water agency under the purview of MEWR that manages the water infrastructure, including storm-water drainage and sewerage treatment. Part of its role is in managing water resources includes (i) planning adequate drainage ahead of new developments in conjunction with relevant stakeholders, (ii) ensuring that developments follow a code of practice that stipulates adequate drainage requirements, for example, minimum platform and crest level for buildings and entrances to underground facilities, (iii) the continual widening, deepening, and maintenance of existing drains and canals, and (iv) implementing a system of island-wide monitoring and flood detection, coupled with the broad dissemination of flood warnings and advisories [30–32]. A holistic integration with other governmental agencies that have relevant impact with LULC change is a strong feature of PUB's water resource management. Through investments totalling >S$2 billion (>USD 1.42 billion), the PUB has considerably reduced flood prone areas in Singapore from about 3,200 ha in the 1970s to about 34 ha in 2015 with intensive efforts in land and drainage management [33]. This significant reduction is remarkable, despite the increased "water-proofing" of the urban surface in Singapore that alters the prevailing hydrometeorological regime, that is, increased frequencies of urban flood episodes.

The PUB also provides a simple, nonmeteorological definition of flash floods, which are localised floods (arising from heavy rainfall) that are constrained within the immediate drainage catchment, and also subsides within an hour [34]. This definition is similar to that proposed by the US National Weather Service, which defines flash floods as "a flood which follows within a few hours (usually less than 6 hours) of heavy or excessive rainfall, dam or levee failure, or the sudden release of water impounded by an ice jam" [35]. The common features implicit in these definitions are that flash floods in Singapore are linked to short-lived but intense storm events, which cause greater storm-water peak flow especially in built-up or low-lying areas, and are especially worsened if these occur during high tide conditions. We hereby use this definition of flash floods in this study.

3. Results

3.1. Hydrometeorological Summary of Singapore Flood History from 1892 to 2015. Through the archival database, a total of 262 flood events spanning from December 1892 until December 2015 were listed (Figure 2). These were separated into flash flood versus nonflash flood categories as explicitly mentioned in either the respective media article or the PUB archive. These floods were a regular occurrence from 1965 to 2015 in which Singapore was an independent state. During this fifty-year period, 212 total flood events were reported in the media archives, with only seven years that were absent of recorded newsworthy flood events. This translated to a mean of about 4.2 reported floods per year. 64 reported floods or

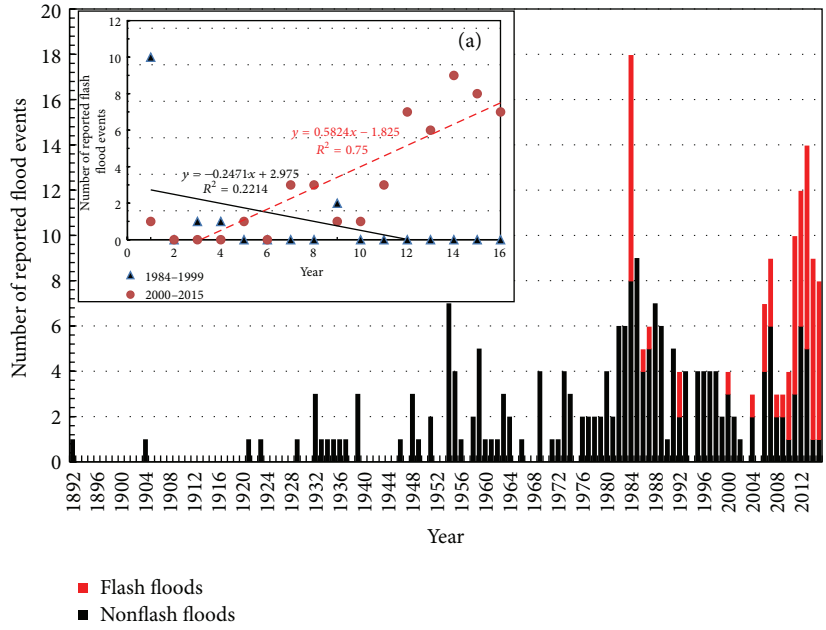

FIGURE 2: Frequency of total number of reported Singapore floods, categorised into flash floods and nonflash floods, listed in *The Straits Times* archive from 1892 to 2015. Insert (a) shows linear trend, depicted by Ordinary Least Squares (OLS), of reported flash floods from 1984 to 1999 (black) and 2000 to 2015 (red dashed) that is also based on the archived flood dataset.

30.2% of all events during these fifty years were defined as flash floods.

A small majority of reported floods in the database (56%) occurred during both monsoon seasons, with 36% of all floods in the winter (NE) monsoon and 20% in the summer (SW) monsoon. Flooding events in the winter monsoon usually arise from prolonged storm events with relatively low precipitation intensities; when reported, durations of these storms range from 2 to 48 h, with mean hourly intensities of ~20.2 mm h^{-1}. In contrast, summer monsoon floods originate from relatively brief storms (2–7 h) with marginally higher mean intensities (~39.3 mm h^{-1}) that usually arise from predawn squall development along the Straits of Malacca west of Singapore. High tide conditions simultaneously occurring during storm events were also explicitly mentioned for 34 floods in the database as a contributing factor towards flooding. The most number of floods (18, of which 10 were classified as flash floods) occurred in 1984, a year in which weak La Niña conditions occurred regionally. Notably, above-average total annual precipitation was observed in Singapore (~2900 mm compared to the 1961–1990 normal of 2150 mm) in 1984.

There appears to be a distinct and recent transition towards more flash floods in Singapore relative to nonflash floods in the data. We analysed two distinct 16-year periods for the frequency of flash floods—a preceding period starting from 1984, which is when the term "flash flood" was first mentioned in *The Straits Times*, until 1999, and a contemporary period from 2000 to 2015. These periods were subject to independent-samples unequal variances t-test to compare if differences were present in the frequency of flash floods being reported. A significant difference of flash flood frequency at the $p = 0.05$ level was discerned in the contemporary ($\overline{u} = 3.13$, $\sigma = 3.20$, 95% CI = 1.42, 4.83) versus the preceding period ($\overline{u} = 0.875$, $\sigma = 2.50$, 95% CI = 0, 2.20). In contrast, there was no significant difference in the means of all flood frequencies in the preceding ($\overline{u} = 5.19$, $\sigma = 4.05$, 95% CI = 3.03, 7.35) and contemporary ($\overline{u} = 5.56$, $\sigma = 4.35$, 95% CI = 3.24, 7.88) periods. An increasing strong linear trend for reported flash flood frequency in the contemporary period is also apparent ($R^2 = 0.75$, Figure 2(a)), especially when compared to the weak decreasing trend from the preceding period.

These results suggest that flash floods—at least those with notable impact in Singapore society that are reported in the local newspaper of record—are becoming a more common occurrence in recent times. Usually, increases in flash flood frequency in the urban context can be attributed towards LULC conversion that result in an earlier storm-water peak, that is, reduced lag time, and increases in surface runoff and discharge relative to infiltration during all precipitation events. This correspondence in more frequent flash floods should also apply to Singapore especially with its rapid LULC conversion and increased population that were documented in Table 1. However, effective urban storm-water drainage management implemented by the PUB that includes extensive canalisation networks of waterways, drains, and reservoirs totalling 8000 km in length [37] appears to be successful in reducing impacts of increased runoff from land cover change, but not so for the impacts of relatively infrequent flood events reported in the archives.

That said, increases in reported flash floods reported in the archives could arise from other causes besides rapid urbanisation. A likely factor could be the long-term variation in precipitation patterns driving these local flooding events. The contemporary increase in flash floods corresponds with

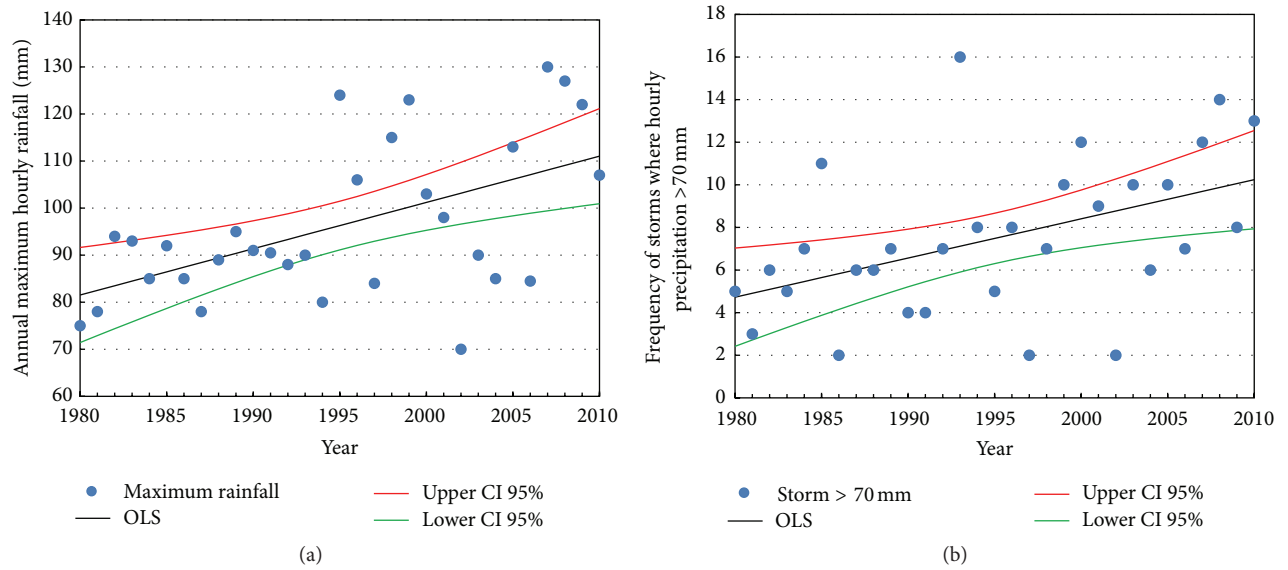

FIGURE 3: (a) Maximum annual hourly rainfall and (b) frequency of large storms, defined as hourly precipitation intensity if >70 mm h^{-1}, that were measured across 28 stations from 1980 to 2010. The mean OLS linear trends and the respective upper and lower 95% confidence intervals are also depicted (source: figures based from data reported in [16]).

previous data analysis done by the MEWR on the changing precipitation dynamics that are observed in Singapore [16]. Specifically, trends of both hourly maximum precipitation and frequency of large storms, defined as hourly total precipitation larger than 70 mm, have been significantly increasing on an annual basis since 1980 by approximately 9.8 mm and 1.8 days per decade, respectively (Figure 3). Attribution of the more frequent, and more intense, rainfall events being recorded island-wide being is not investigated herein, but this trend accords with expected changes in precipitation patterns from increased greenhouse gases at global scales [17].

3.2. Key Aspects of Floods in Singapore. Specific characteristics pertaining to each reported flood in the database can be viewed in the supplemental material (Table S1 in Supplementary Material available online at http://dx.doi.org/10.1155/2016/7159132); however, selected flood events that had notable precipitation intensities and/or had direct impact on Singapore's society through deaths, injuries, infrastructural damage, and transport disruption are listed in chronological order in Table 2. Three aspects of these floods are apparent. First, distinct variations in rainfall intensities reported in the newspaper reports versus those recorded at the Changi meteorological station are often observed; the difference is readily apparent in contemporary flood events post-2000. This result suggests that recent precipitation events—at least those that result in notable flooding episodes, including the June 2013 storm and resulting flood modelled by Vaid [14]—appear to be more localised or "patchy" in spatial extent relative to the entire island; that is, precipitation intensities occurring at Changi do not approach the magnitude reported in the media article.

Based on 171 floods reported in Table S1 after 1984 (when Changi station was deemed as the official station of record), a total of 36 flood events had no recorded rainfall at Changi (13 events after the year 2000). Further, the list of floods post-2000 in Table 2 indicates that measured precipitations at Changi are often considerably less than magnitudes reported in the news archives from rainfall gauges located in close proximity to the flood events. The implication, therefore, is that flood hazard analyses, or planning for flood management in Singapore based solely on meteorological data from the station of record, could result in the critical omission of these isolated storms.

Second, a relatively low number of floods—15 out of 85 contemporary floods post-2000—that occur during increasing or high tide conditions could suggest that extensive investments in flood management by the PUB have been effective. These measures include the inclusion of on-site storm-water detention tanks in building codes for building developers [38], development and construction of urban storm-water diversion canals, for example, the Stamford Diversion Canal that was designed and constructed after a series of floods affecting central Singapore in June 2010 [39], and tidal gates that pump excess storm-water flow out to sea even during high tide conditions, for example, the Marina Barrage in South Singapore [40].

Third, compared to neighbouring Southeast Asian nations, for example, the October-November 2011 Thailand floods where more than 500 deaths occurred [41], flooding impacts in Singapore are relatively minor in terms of human casualties. For instance, seven deaths were reported in the most severe flood from the archives that occurred in 1978, where 512.4 mm of rain fell over a 24 hr period (Per *The Straits Times*, reports from media published in other languages indicate that eight deaths resulted from the 1978 flood). The relatively low death toll from all floods in the archives, especially post-1965, can clearly be attributed to the water management practices of the PUB. This applies to the development of physical infrastructure development not

Table 2: Selected characteristics of notable flood events with significant impact occurring within Singapore. Rainfall, location, and damage are based on reported information from the relevant archived *Straits Times* article. Flash floods as defined in this study are italicised.

Date	Rainfall intensity (Changi airport)[a]	Location[b]	Reported damage and other relevant details
		Pre-1965	
22 March 1936	80.26 mm/40 mins (NA)	Central	(i) Flooding of roads and houses (ii) Traffic jams (iii) Falling trees (iv) Dislocation of telephone system
23 October 1954	101.6 mm/2.5 hours (NA)	Central	(i) Stoppage of airport flights (ii) Marooned/stranded cars
13 November 1963	42.93 mm/3 hours (0.3 mm)	South	(i) Power failure in several places (ii) Traffic jams
		1965–1980	
11 December 1969	467 mm/17 hours (NA)	Island-wide	(i) 5 killed (ii) 3100 people lost their homes (iii) Flood depth up to 2.5 m (iv) S$4.3 million damage (2015 value of S$16 million)
23 September 1971	58.4 mm/2 hours (NA)	Central	(i) Power failure (ii) Landslides (iii) Traffic jams and road accidents (iv) Airport delays
2 December 1978	512 mm/24 hours (NA)	Island-wide	(i) Singapore's "worst" flood on record (ii) 7 deaths, 1000 people evacuated (iii) Flood depth reached 2 m (iv) Disruption of power and telephone lines (v) 50 roads sealed off (vi) S$10 million damages (2015 value of S$22.5 million) (vii) Flooding coinciding with high tide conditions
		1981–1999	
22 August 1983	178.1 mm/2 hours (182.0 mm/3 hours)	East	(i) Flooding of airport car park
2 March 1984	*112.1 mm/12 hours (119.0 mm/3 hours)*	*West and Central*	(i) Massive traffic jams (ii) Landslides and fish farms affected (iii) Blackouts throughout the island (iv) University exams delayed
18 January 1989	94.9 mm/8 hours (No rain reported)	Central	(i) Traffic jams and stranded people
25 February 1997	98 mm/1 hour (27.0 mm/3 hours)	East	(i) Blackouts, flooded houses, and damaged belongings
12 July 1998	*165 mm/3.5 hours (34.0 mm/3 hours)*	*East*	(i) *Shops damaged*
6 January 1999	NA (10.9 mm/3 hours)	South	(i) Business goods damaged
22 December 1999	NA (12.9 mm/24 hours)	South and Central	(i) Shops flooded (ii) Businesses disrupted (iii) Flooding coinciding with high tide conditions
		2000–2015	
6 April 2000	166 mm/1.5 hours (3.7 mm/24 hrs)	Central	(i) 2 deaths (ii) "1-in-100 year storm"
16 June 2010	*100 mm/3 hours (38 mm/6 hours)*	*Central*	(i) *Flood depth 0.3 m* (ii) *Traffic jam* (iii) *Shops damaged*
25 June 2010	*100 mm/1 hour (26 mm/3 hours)*	*Central*	(i) *Traffic congestion* (ii) *Insurance claims of S$23 million (2015 value of S$25.3 million)*
5 May 2012	*68.6 mm/0.5 hours (0.2 mm/3 hours)*	*Central and North*	(i) *Flood depth 0.25 m*
5 September 2013	*102.8 mm/1.5 hours (25.2 mm/6 hours)*	*West*	(i) *Part of major highway shut down* (ii) *Traffic jam* (iii) *Flood depth 0.5 m* (iv) *Flooding coinciding with high tide conditions*
29 July 2014	*49.4 mm/30 mins (29 mm/6 hours)*	*Central*	(i) *Traffic jam*

[a]When applicable, precipitation data in parenthesis are reported from the WMO meteorological station of record at Changi airport.
[b]Specific locations in parenthesis are categorised into specific sectors of Singapore (north, south, east, west, and central).

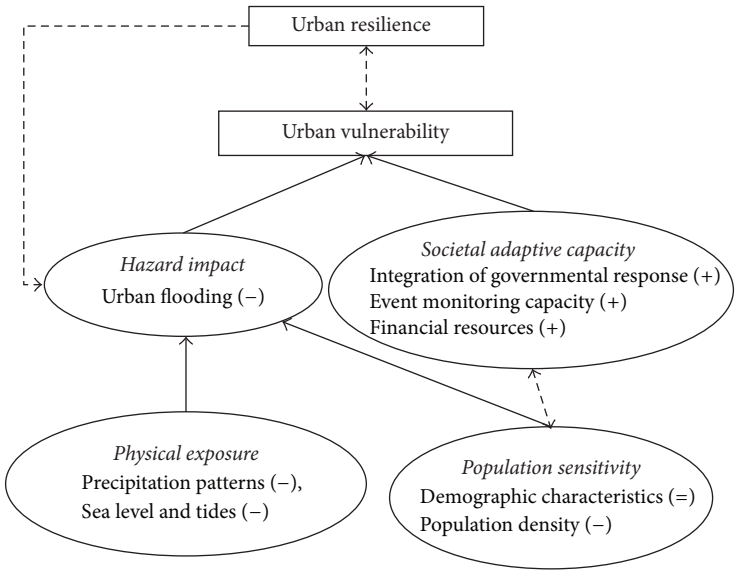

Figure 4: Framework of Singapore's urban vulnerability to flooding based on previous conceptual frameworks in [17, 25]. The ovals are component factors of overall vulnerability with relevant physical and social attributes italicised. The impacts of such attributes towards overall vulnerability are positive (+), negative (−), or neutral (=). Solid lines indicate direct connections between components with the direction being indicated by the arrowhead, while dashed connections indicate potential feedbacks. Lastly, the state of vulnerability directly affects resilience to flooding, which feedbacks on the magnitude of the flood hazard impact.

only through extensive canalisation within flood prone areas and rapid flood detection instrumentation and monitoring, but also through advisories widely broadcasted across media platforms that (i) warn the public of flash floods and (ii) also advise on the relevant course of individual action [42]. Instead, the flood impacts are greater towards water damage to property and transport disruption due to inundation of surface roads. This was most evident in a series of floods occurring in 2010 that took place in the central areas of Singapore Island in which most of the commercial district is located. While no human injuries were reported, there was substantial property damage to 100 shops and 48 vehicles along roads flooded by the storm that resulted in insurance claims totalling S$23 (USD 16.3) million in 2010 (S$25.3 (USD 18) million in 2015) [43].

4. Discussion: Future Vulnerabilities of Urban Flooding in Singapore

The archival analysis strongly suggests that PUB's integrated approach to floodwater management in Singapore has largely been successfully applied over the past 50 years. Despite the rapid LULC change in a city exposed to frequent and intense storm events, flooding hazards have largely been minimised in impact through effective adaptation techniques, especially with low reported loss of life. In the context of urban vulnerability analysis (Figure 4), notwithstanding the higher physical exposure (e.g. changing precipitation patterns) and increasing sensitivity (e.g., from greater population densities) leading to potentially large impacts, there is considerably strong adaptive capacity from the actions of PUB that have considerably reduced the urban vulnerability of Singapore towards flood hazards. The net result is a resilient system in Singapore that minimises the impacts and risks associated with present-day flooding, especially with respect to historical conditions.

However, the pattern of vulnerability suggested in Figure 4 may superficially be implied as static and should not be considered as such. With increasing greenhouse gases emissions resulting in the intensification of the hydrological cycle, there should be concern of how altered precipitation regimes in Southeast Asia, such as those modelled and described by [22], will alter the existing urban vulnerability to floods. Apart from the direct influence of increased greenhouse gas forcing on regional precipitation, a further complication is that recent research indicates that frequencies of extreme ENSO [44] and Indian Ocean Dipole events [45] are likely to be altered up to 2100. These teleconnections have considerable historical influence on the variability of regional rainfall patterns [8] and may exacerbate conditions that favour intense precipitation leading to flooding. The increased uncertainty brought about by these physical exposure factors should be considered into future assessments of flood vulnerability and resilience.

Another important consideration should be focused on sea level rise (SLR) and its impact on floods in Singapore. Wong [46] analysed local impacts from an abnormal high tide event that took place in February 1974 on low-lying areas in Singapore as an analogue for 1 m global SLR conditions; he indicated the importance of tidal gates to minimise tidal inflow from reducing the effectiveness of storm-water drainage channels. While these explicit adaptation measures to improve Singapore's resilience to urban flooding have been developed in accordance with IPCC AR5 SLR projections, for example, reclaimed land being 2.25 m above highest tide level in Singapore [47], recent post-AR5 research suggests

that this physical exposure factor may be magnified. Analyses of potential acceleration of melting continental ice sheets, for example, in West Antarctica [48, 49], raise the likelihood of future SLR being higher than the conservative IPCC [17] estimates, with subsequent negative impacts on urban flood vulnerability.

Apart from physical exposure factors, changes in future population growth in Singapore will impinge on its sensitivity towards flood hazards. Urbanisation rates are not expected to diminish in rate over the next few decades. Extensive municipal planning has been put into place for the medium term, both in terms of LULC use up until 2030 [50] and towards preparing population growth in that same timeframe for a projected maximum of 6.9 million [51]. The net result of which is likely to be substantial increases in population density, as well as in areas prone to flash flooding events that will require substantial investments towards flood management. The sensitivity of population towards hydrometeorological hazards would, in all likelihood, be negatively affected.

The corollary to these factors would be that present net positives in adaptive capacity towards urban flooding must be maintained, if not improved, to ensure that the low vulnerability/high resilience vis-à-vis Singapore's flood context persists in the future. The approach done by the PUB, such as with foresight of continual investments in drainage improvement, combined with regular infrastructural maintenance, has largely succeeded and would probably be required at larger scales in the future. Anticipating the impacts based on the vulnerability framework in this paper may be a good step towards this end; based on the complicated and uncertainty of the factors raised above, however, it is uncertain to which extent an intelligent urban design and urban management—even successfully applied in Singapore—can buffer these negative effects of flooding.

5. Conclusions

This study examines historical flood hazard impacts upon a major city-state in Singapore through a combination of archival records and meteorological station data analysis. The combined methodology enables additional insights into flood impacts that are precluded by studies that only examine meteorological data. The key results indicate that, in Singapore's case, the patterns of flooding have been altered over time; the incidence of flash floods relative to nonflash floods in the archival data appears to be increasing in recent years, as noted by the meteorological data analysed by MEWR [16], but the impacts of flash floods appear to be attenuated by the integrated, and hitherto effective, flood management from the PUB that increases the adaptive capacity of Singapore's vulnerability to this hazard.

The steps taken in Singapore that result in the low vulnerabilities, and increased resilience, to flood hazards over the past 50 years could be examined as a case study by other rapidly urbanising cities or city-states. In particular, the holistic integration of decision-making and effective water resource management simultaneously minimises the risk and maximises the resilience towards floods. That said, altered regional hydrometeorological conditions brought upon by climate change and future alterations to Singapore's demographic composition may result in the need for further anticipatory measures towards maintaining the city-state's resilience to floods.

Competing Interests

The authors declare that they have no competing interests.

Acknowledgments

A major impetus for this paper stemmed from discussions between the authors with Dr. Alan Ziegler and Dr. Robert Wasson from NUS and Ms. Claire Kennedy (AON Benfield) during the Future Floods Workshop organised by the Faculty of Arts and Social Sciences Environment Cluster (NUS) and AON Benfield in February 2015. The authors sincerely thank these individuals for their suggestions. WTLC's research is supported by the NUS through research Grant R-109-000-162-133.

References

[1] P. J. Crutzen, "The Anthropocene," in *Earth System Science in the Anthropocene*, E. Ehlers and T. Krafft, Eds., Springer, Berlin, Germany, 2006.

[2] United Nations, Department of Economic and Social Affairs, Population Division, World Urbanization Prospects: The 2014 Revision, Highlights (ST/ESA/SER.A/352), http://esa.un.org/unpd/wup/highlights/wup2014-highlights.pdf.

[3] T. R. Oke, *Boundary Layer Climates*, Methuen, New York, NY, USA, 1987.

[4] W. T. L. Chow and M. Roth, "Temporal dynamics of the urban heat island of Singapore," *International Journal of Climatology*, vol. 26, no. 15, pp. 2243–2260, 2006.

[5] J. M. Shepherd, "A Review of current investigations of urban-induced rainfall and recommendations for the future," *Earth Interact*, vol. 9, no. 12, pp. 1–27, 2005.

[6] M. Georgescu, P. E. Morefield, B. G. Bierwagen, and C. P. Weaver, "Urban adaptation can roll back warming of emerging megapolitan regions," *Proceedings of the National Academy of Sciences of the United States of America*, vol. 111, no. 8, pp. 2909–2914, 2014.

[7] S. E. Brun and L. E. Band, "Simulating runoff behavior in an urbanizing watershed," *Computers, Environment and Urban Systems*, vol. 24, no. 1, pp. 5–22, 2000.

[8] M. Fong, *The Weather and Climate of Singapore*, Meteorological Services Singapore, Singapore, 2012.

[9] M. Roth and W. T. L. Chow, "A historical review and assessment of urban heat island research in Singapore," *Singapore Journal of Tropical Geography*, vol. 33, no. 3, pp. 381–397, 2012.

[10] E. Velasco and M. Roth, "Review of Singapore's air quality and greenhouse gas emissions: current situation and opportunities," *Journal of the Air & Waste Management Association*, vol. 62, no. 6, pp. 625–641, 2012.

[11] K. Chatterjea, "The impact of tropical rainstorms on sediment and runoff generation from bare and grass-covered surfaces: a plot study from Singapore," *Land Degradation and Development*, vol. 9, no. 2, pp. 143–157, 1998.

[12] P. V. Mandapaka and X. Qin, "Analysis and characterization of probability distribution and small-scale spatial variability of rainfall in singapore using a dense gauge network," *Journal of Applied Meteorology and Climatology*, vol. 52, no. 12, pp. 2781–2796, 2013.

[13] P. V. Mandapaka and X. Qin, "A large sample investigation of temporal scale-invariance in rainfall over the tropical urban island of Singapore," *Theoretical and Applied Climatology*, vol. 122, no. 3-4, pp. 685–697, 2014.

[14] B. H. Vaid, "Numerical simulations and analysis of June 16, 2010 heavy rainfall event over Singapore using the WRFV3 model," *International Journal of Atmospheric Sciences*, vol. 2013, Article ID 825395, 8 pages, 2013.

[15] F. Beck, A. Bárdossy, J. Seidel, T. Müller, E. Fernandez Sanchis, and A. Hauser, "Statistical analysis of sub-daily precipitation extremes in Singapore," *Journal of Hydrology: Regional Studies*, vol. 3, pp. 337–358, 2015.

[16] MEWR (Ministry of the Environment and Water Resources), *Report on Key Conclusions and Recommendations of the Expert Panel on Drainage Design and Flood Protection Measures*, 2012, http://www.pub.gov.sg/managingflashfloods/floodResilience-Plan/Documents/fullReport.pdf.

[17] IPCC (Intergovernmental Panel on Climate Change), "Summary for policymakers," in *Climate Change 2013: The Physical Science Basis. Contribution of Working Group I to the Fifth Assessment Report of the Intergovernmental Panel on Climate Change*, T. F. Stocker, D. Qin, G.-K. Plattner et al., Eds., Cambridge University Press, Cambridge, UK, 2013.

[18] K. E. Trenberth, "Framing the way to relate climate extremes to climate change," *Climatic Change*, vol. 115, no. 2, pp. 283–290, 2012.

[19] J. H. Christensen, K. K. Krishna, E. Aldrian et al., "Climate phenomena and their relevance for future regional climate change," in *Climate Change 2013: The Physical Science Basis. Contribution of Working Group I to the Fifth Assessment Report of the Intergovernmental Panel on Climate Change*, T. F. Stocker, D. Qin, G.-K. Plattner et al., Eds., Cambridge University Press, Cambridge, 2013.

[20] Y. Hijioka, E. Lin, J. J. Pereira et al., "Asia," in *Climate Change 2014: Impacts, Adaptation, and Vulnerability. Part B: Regional Aspects. Contribution of Working Group II to the Fifth Assessment Report of the Intergovernmental Panel on Climate Change*, V. R. Barros, C. B. Field, D. J. Dokken et al., Eds., pp. 1327–1370, Cambridge University Press, Cambridge, UK, 2014.

[21] C. Marzin, A. Hines, J. Murphy, C. Gordon, and R. Jones, "Chapter 1 executive sumamry," in *Singapore's Second National Climate Change Study—Phase 1*, C. Marzin, R. Rahmat, D. Bernie et al., Eds., 2015, http://ccrs.weather.gov.sg/publications-second-National-Climate-Change-Study-Science-Reports.

[22] R. Jones, G. Redmond, T. Janes et al., "Climate change projections," in *Singapore's Second National Climate Change Study—Phase 1*, C. Marzin, R. Rahmat, D. Bernie et al., Eds., chapter 5, 2015, http://ccrs.weather.gov.sg/publications-second-National-Climate-Change-Study-Science-Reports.

[23] A. D. Ziegler, J. P. Terry, G. J. H. Oliver et al., "Increasing Singapore's resilience to drought," *Hydrological Processes*, vol. 28, no. 15, pp. 4543–4548, 2014.

[24] W. T. L. Chow, W.-C. Chuang, and P. Gober, "Vulnerability to extreme heat in metropolitan phoenix: spatial, temporal, and demographic dimensions," *The Professional Geographer*, vol. 64, no. 2, pp. 286–302, 2012.

[25] P. Romero Lankao and H. Qin, "Conceptualizing urban vulnerability to global climate and environmental change," *Current Opinion in Environmental Sustainability*, vol. 3, no. 3, pp. 142–149, 2011.

[26] L. Chang, K. C. Seto, and S. Huang, "Chapter 11: climate change, urban flood vulnerability, and responsibility in Taipei," in *Urbanization and Sustainability*, C. Boone and M. Fragkias, Eds., pp. 179–198, Springer, Berlin, Germany, 2013.

[27] Department of Statistics Singapore, *Population and Population Structure*, 2015, http://www.singstat.gov.sg/statistics/browse-by-theme/population-and-population-structure.

[28] National Library Board, NewspaperSG, 2015, http://eresources.nlb.gov.sg/newspapers/default.aspx.

[29] PUB, "Recent Flash Floods," 2015, http://www.pub.gov.sg/managingflashfloods/Pages/recent.aspx.

[30] C. Tortajada and Y. K. Joshi, "Water demand management in Singapore: involving the public," *Water Resources Management*, vol. 27, no. 8, pp. 2729–2746, 2013.

[31] C. Tortajada, Y. Joshi, and A. Biswas, *The Singapore Water Story*, Routledge/Taylor & Francis, New York, NY, USA, 2013.

[32] PUB, "Stormwater Management Strategies," 2015, http://www.pub.gov.sg/managingflashfloods/fms/Pages/default.aspx.

[33] PUB, "The Past and the Present," 2015, http://www.pub.gov.sg/managingflashfloods/Pages/PastPresent.aspx.

[34] PUB, "Frequently Asked Questions," 2015, http://www.pub.gov.sg/managingflashfloods/faqs/Pages/default.aspx?Print2=yes.

[35] National Oceanic and Atmospheric Administration (NOAA), *Glossary of Hydrologic Terms*, 2014, http://www.nws.noaa.gov/om/hod/SHManual/SHMan014_glossary.htm.

[36] Google Earth, 2015, https://www.google.com/earth/.

[37] Public Utilities Board (PUB), *Strengthening Singapore's Flood Resilience*, 2013, http://www.pub.gov.sg/managingflashfloods/FMS/Documents/FloodManagementSg.pdf.

[38] PUB, "On-Site Stormwater Detention Tank Systems," 2014, http://www.pub.gov.sg/managingflashfloods/FMS/Documents/detentionTank.pdf.

[39] J. Cheam, *Forging a Greener Tomorrow, Singapore's Environmental Journey from Slum to Eco-City*, Straits Times Press, Singapore, 2012.

[40] W. H. Moh and P. L. Su, "Marina Barrage—a unique 3-in-1 project in Singapore," *Structural Engineering International*, vol. 19, no. 1, pp. 17–21, 2009.

[41] A. D. Ziegler, H. S. Lim, C. Tantasarin, N. R. Jachowski, and R. Wasson, "Floods, false hope, and the future," *Hydrological Processes*, vol. 26, no. 11, pp. 1748–1750, 2012.

[42] PUB, Flash Flood Advisory October 2014, http://www.pub.gov.sg/managingflashfloods/SafetyAdvisory/Documents/Flash-FloodAdvisory2014.pdf.

[43] C. Kennedy, "Flooding in Singapore: an overview," Proceedings of Future Floods: An Exploration of a Cross-Disciplinary Approach to Flood Risk Forecasting, FASS Environment Research Cluster, the Institute of Water Policy (Lee Kuan Yew School of Public Policy) and AON Benfield Pte. Ltd, https://blog.nus.edu.sg/environmentcluster/files/2015/03/FUTURE-FLOODS-NUS-Workshop-Claire-Kennedy-11cg2j1.pdf.

[44] W. Cai, S. Borlace, M. Lengaigne et al., "Increasing frequency of extreme El Niño events due to greenhouse warming," *Nature Climate Change*, vol. 4, no. 2, pp. 111–116, 2014.

[45] W. Cai, A. Santoso, G. Wang et al., "Increased frequency of extreme Indian ocean dipole events due to greenhouse warming," *Nature*, vol. 510, no. 7504, pp. 254–258, 2014.

[46] P. P. Wong, "Impact of a sea level rise on the coasts of Singapore: preliminary observations," *Journal of Southeast Asian Earth Sciences*, vol. 7, no. 1, pp. 65–70, 1992.

[47] National Climate Change Secretariat (NCCS), *Singapore's Approach on Adaptation*, 2012, https://www.nccs.gov.sg/nccs-2012/singapores-approach-on-adaptation.html.

[48] E. Rignot, J. Mouginot, M. Morlighem, H. Seroussi, and B. Scheuchl, "Widespread, rapid grounding line retreat of Pine Island, Thwaites, Smith, and Kohler glaciers, West Antarctica, from 1992 to 2011," *Geophysical Research Letters*, vol. 41, no. 10, pp. 3502–3509, 2014.

[49] I. Joughin, B. E. Smith, and B. Medley, "Marine ice sheet collapse potentially under way for the Thwaites Glacier Basin, West Antarctica," *Science*, vol. 344, no. 6185, pp. 735–738, 2014.

[50] URA (Urban Redevelopment Authority), *Master Plan 2014*, 2014, https://www.ura.gov.sg/uol/master-plan.aspx?p1=View-Master-Plan&p2=master-plan-2014.

[51] National Population and Talent Division (NPTD), *A Sustainable Population for a Dynamic Singapore: Population White Paper*, 2013, http://population.sg/whitepaper/.

Hindawi Publishing Corporation
Advances in Meteorology
Volume 2016, Article ID 9437401, 9 pages
http://dx.doi.org/10.1155/2016/9437401

Research Article

Accuracy Improvement of Discharge Measurement with Modification of Distance Made Good Heading

Jongkook Lee,[1] Hongjoon Shin,[2] Jeonghwan Ahn,[2] and Changsam Jeong[2]

[1]*Disaster Information Analysis Center, National Disaster Management Institute, Seoul 04212, Republic of Korea*
[2]*Department of Civil and Environment, Induk University, Seoul 01878, Republic of Korea*

Correspondence should be addressed to Changsam Jeong; csjeong@induk.ac.kr

Received 6 November 2015; Accepted 10 January 2016

Academic Editor: Huan Wu

Remote control boats equipped with an Acoustic Doppler Current Profiler (ADCP) are widely accepted and have been welcomed by many hydrologists for water discharge, velocity profile, and bathymetry measurements. The advantages of this technique include high productivity, fast measurements, operator safety, and high accuracy. However, there are concerns about controlling and operating a remote boat to achieve measurement goals, especially during extreme events such as floods. When performing river discharge measurements, the main error source stems from the boat path. Due to the rapid flow in a flood condition, the boat path is not regular and this can cause errors in discharge measurements. Therefore, improvement of discharge measurements requires modification of boat path. As a result, the measurement errors in flood flow conditions are 12.3–21.8% before the modification of boat path, but 1.2–3.7% after the DMG modification of boat path. And it is considered that the modified discharges are very close to the observed discharge in the flood flow conditions. In this study, through the distance made good (DMG) modification of the boat path, a comprehensive discharge measurement with high accuracy can be achieved.

1. Introduction

Considering the steadily increasing water demand in Korea, accurate river discharge information is important for sustainable water resources management such as flood control, hydraulic structure design, and hydroenvironment management. Efforts have been made to accurately collect river discharge information by performing systematic measurements and introducing emerging technologies [1]. However, it is not easy to measure the river discharge accurately and efficiently. Existing river discharge measurement methods that are most commonly deployed in Korea to date are the floating rod method and current meters. Quick and convenient measurement is the advantage of these methods, but there is a drawback that the uncertainty of velocity and cross section area increases due to the unknown flow route when the floating rod does not flow along the assumed straight line. However, in recent years, the Acoustic Doppler Current Profiler (ADCP), which can probe velocity and bottom changes simultaneously, has been increasingly adopted as an acceptable tool in Korea and is now regarded as the preferred method [2]. Because this method measures the change of flow velocity and depth of cross section continuously, this method has an advantage of detailed consideration for the change.

The ADCP was first developed to log ship speed on the ocean. It was subsequently introduced as a method to measure water discharge in the late 1980s. By the 1990s, the use of ADCP equipment gradually increased due to the improvement of accuracy of river measurements and the riverbed tracking function.

The United States Geological Survey (USGS) used the actual measurement results at 12 hydrological stations to examine the application of an ADCP to water discharge measurements and demonstrated that there was more than a 5% error by comparing the existing Price AA current meter and the stage-discharge relationship [3]. Mueller [4] evaluated various ADCP models using discharge measurements in the field and analyzed the bias caused with the riverbed tracking function. Oberg [5] examined the existing method and suggested a technique that is able to calculate the

deviation of a riverbed tracking function using a differential global positioning system (DGPS). Gartner and Ganju [6] conducted a study to clarify the measurement error of the current velocity near the water surface, which might be physically disturbed by the ADCP's housing with the small blanking distance, as compared with acoustic Doppler velocimetry (ADV). González-Castro et al. [7] noted that the current velocity in the downstream direction had a large bias in representing the time-averaged current velocity and stated that this bias could be reduced by spatial leveling as they compared data of the instantaneous current velocity measured by a mobile ADCP with the measurement result of a fixed ADCP. Adler and Nicodemus [8] developed a method in which the data measured by the ADCP was conducted through postprocessing to calculate an average velocity vector, whereas Muste et al. [9] conducted a study that calculated the velocity vector after postprocessing result measured by the ADCP. Muste et al. [9, 10] presented that a turbulent flow could be calculated when an ADCP was deployed at a fixed position and the suggested postprocessing procedure was utilized. In recent years, there have been attempts to measure the bed load movement and concentration of a suspended load using the backscatter intensity of an ADCP [11–13]. Parsons et al. [14] demonstrated that ADCPs have become multipurpose instruments, demonstrating considerable promise for an improved process-based understanding of geophysical processes in a wide range of hydrological environments [15–24].

In this study, we improve the discharge measurement using remote-controlled boat with ADCP. However, there is a measurement error due to irregular boat path in flood flow. Therefore, the development of a method to reduce this measurement error will enable the river discharge to be measured more accurately and efficiently and we focused on the method to determine an optimal cross section of an arbitrary path due to a remote-controlled operation in a flood condition. For this, the distance made good (DMG) line by the east-north-up (ENU) coordinate system was used to resolve these issues.

2. Background

2.1. Acoustic Doppler Current Profiler (ADCP). An ADCP transmits, receives, and processes ultrasonic waves reflected from neutrally buoyant particles inside a small volume and gates them into a specific depth and then produces velocity profiles. An ADCP measures the instantaneous current velocity; this approach is different from that of a general current meter, which only measures point velocity. Therefore, there is a difference between the velocity data obtained from an ADCP and the time-averaged velocity data obtained from continuous measurement over dozens of seconds. Figure 1 illustrates a typical ADCP. There are four independently working acoustic beams with each beam angled 20–30° from the vertical axis of the transducer assembly [25].

River discharge can be measured by an ADCP mounted on a moving boat. The ADCP autonomously identifies the direction of the boat and the current velocities using a built-in compass. It calculates the discharge by combining the distance moved over a time interval, the shape of a cross section, and the current velocity. The ADCP is able to measure discharge of large rivers. The ADCP calculates discharge using (1). When using ADCP data to measure discharge, the integral in (1) is replaced by a summation, and the elements dz and dL are replaced by Δz and ΔL, which are the depth and horizontal resolutions of the ADCP measurements, respectively. The depth resolution Δz corresponds to the range interval. The horizontal resolution ΔL depends on the boat speed and is equal to the distance traveled by the boat during the time interval [26]. Consider

$$Q = \iint n(L) \cdot U(z, L)\, dz\, dL, \tag{1}$$

where Q is the discharge, L is the position along an arbitrary line across the river, n is the horizontal unit vector normal to the line at L, U is the velocity vector, and z is the water depth.

An ADCP extracts the current velocity elements used in a discharge calculation by subtracting the boat velocity, which is calculated by river bed tracking from the measured velocity and changing from the progress direction of the boat to an element at a right angle. Therefore, when the ADCP movement is faster than the actual flow, errors can easily occur when measuring the current velocity. In particular, the error is known to increase when the current velocity is slow [25]. Therefore, the ADCP movement should not exceed three times the current velocity, and ADCP should be employed at a velocity slower than the current velocity to obtain the most optimal data [27].

2.2. Instrument Setup. A remote-controlled boat equipped with an ADCP and RTK (real-time kinematic) GPS (global positioning system) was used to measure the bottom geometry, velocity profile, and river discharge simultaneously. This remote-controlled boat is propelled by twin DC (direct current) brushless motors with a 2.4 GHz RC controller, providing control up to 1 km and operating for 3 hours with a 12 V 30 A DC battery (see more details in Table 1).

Table 1: Specification of remote-controlled boat.

Length	1.35 m
Width	0.48 m
Height	0.25 m
Weight	18.5 kg
Engines	Twin DC brushless motors up to 8000 rpm
Propellers	5.59 pitch 4 blades
Hooks	Five stainless steel hooks
Grab handles	Two plastic grab handles
Mounting plates	One PCM box acyle mounting plate
Transducer holder	130 mm diameter holder
Remote controller and receiver	Hitec Optic 6 2.4 GHz 6Ch RC set
Motor controller	180 amp RC motor controller

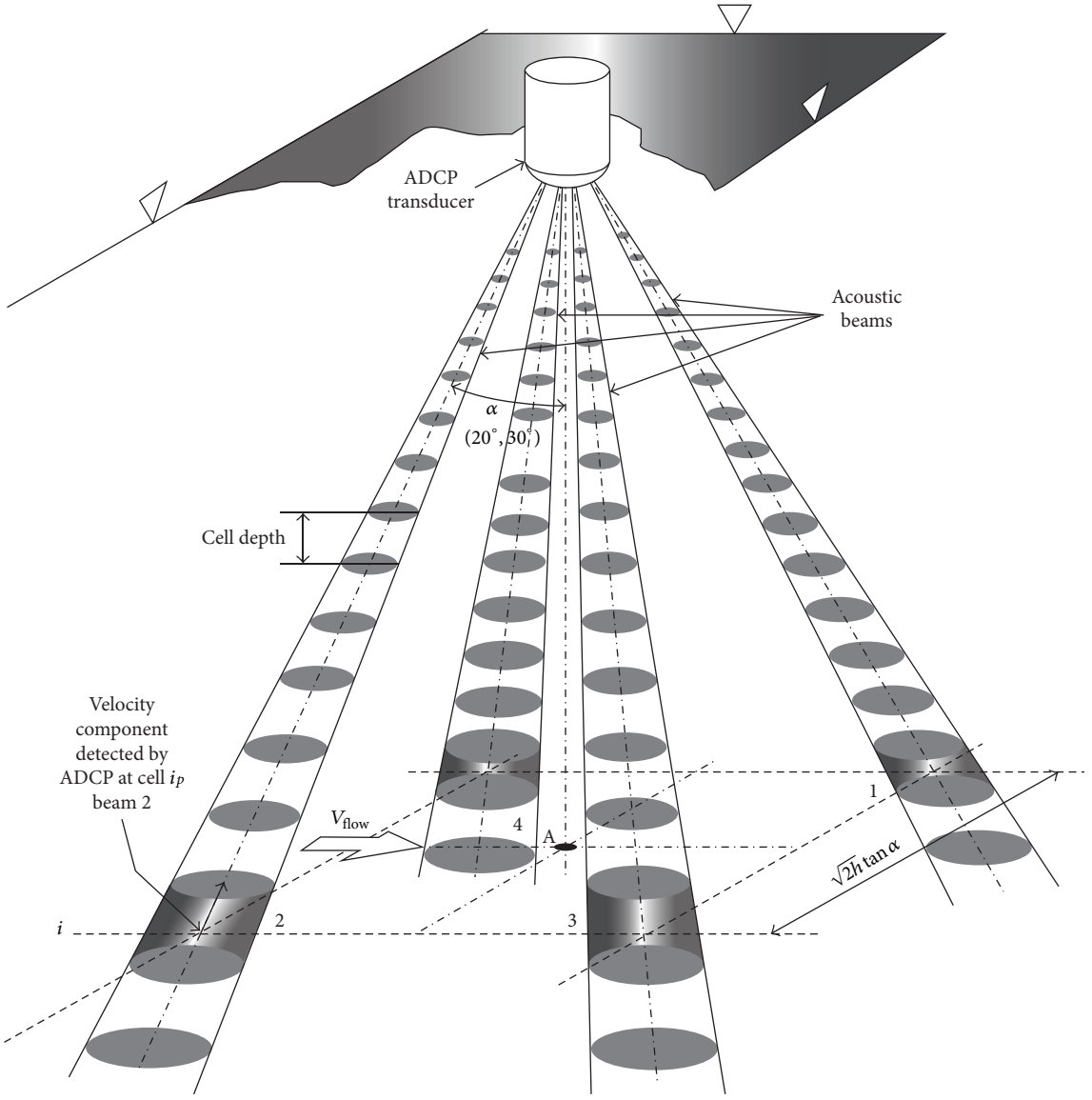

Figure 1: ADCP measurement diagram [9].

The positional information of the remote-controlled boat is produced in three ways: bottom tracking, DGPS (differential GPS), and RTK GPS. The bottom tracking is the preferred method when there is no bed load movement. The accuracy of DGPS and RTK GPS is 1-2 m and 2-3 cm, respectively. Three different types of positional information play important roles in reducing the error in the bathymetry measurement.

2.3. Distance Made Good (DMG). A rhumb line is an arc crossing all meridians of longitude at the same angle as shown in Figure 2(a), and that is a path with constant bearing as measured relative to true or magnetic north. On a Mercator projection map, a rhumb line is a straight line as shown in Figure 2(b). Distance made good is the distance between two points on the Earth along a rhumb line connecting the two points.

3. Measurement and Analysis

3.1. Site Characteristics. To evaluate the compatibility and accuracy of the moving boat method in normal and flood flow conditions, discharge measurements were performed at Mokgye site in Korea (Table 2, Figure 3). This site has a well-defined rating curve because of the upstream Chungju regulation dam release. Figure 4 illustrates the flood discharge data from the Chungju regulation dam and the water levels of the Mokgye site from June 28, 2011, to June 30, 2011. As shown in the figure, the Mokgye site is directly influenced by the Chungju regulation dam, and there are very limited or no tributary inflows between the Mokgye site and the Chungju regulation dam, with the controlled discharge data from the dam securing the rating discharge of this site. Table 2 shows the hydrological characteristics of the Mokgye site.

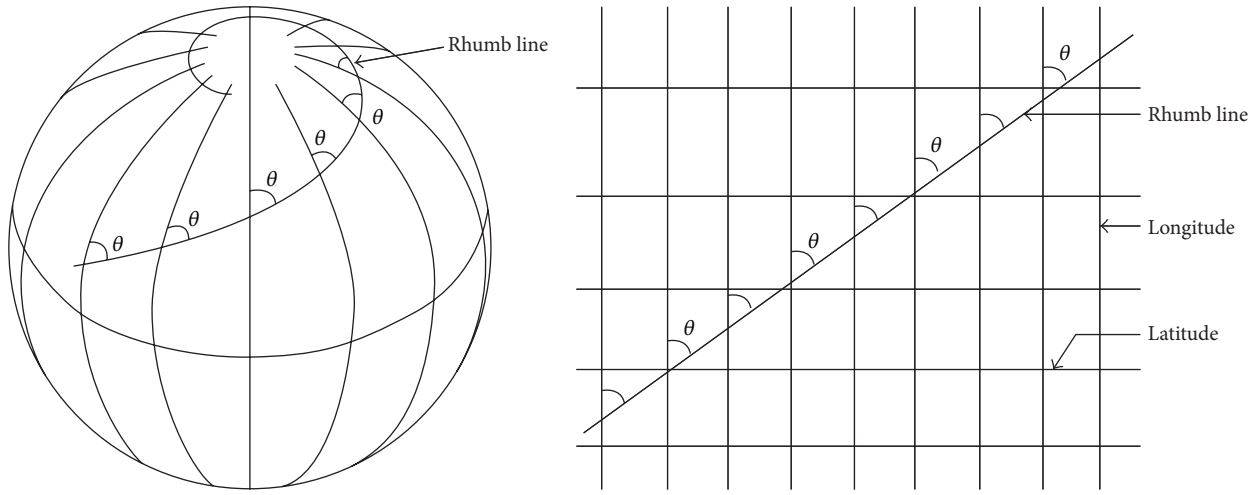

(a) Rhumb line (b) Rhumb line on Mercator projection map

Figure 2: Rhumb line and distance made good.

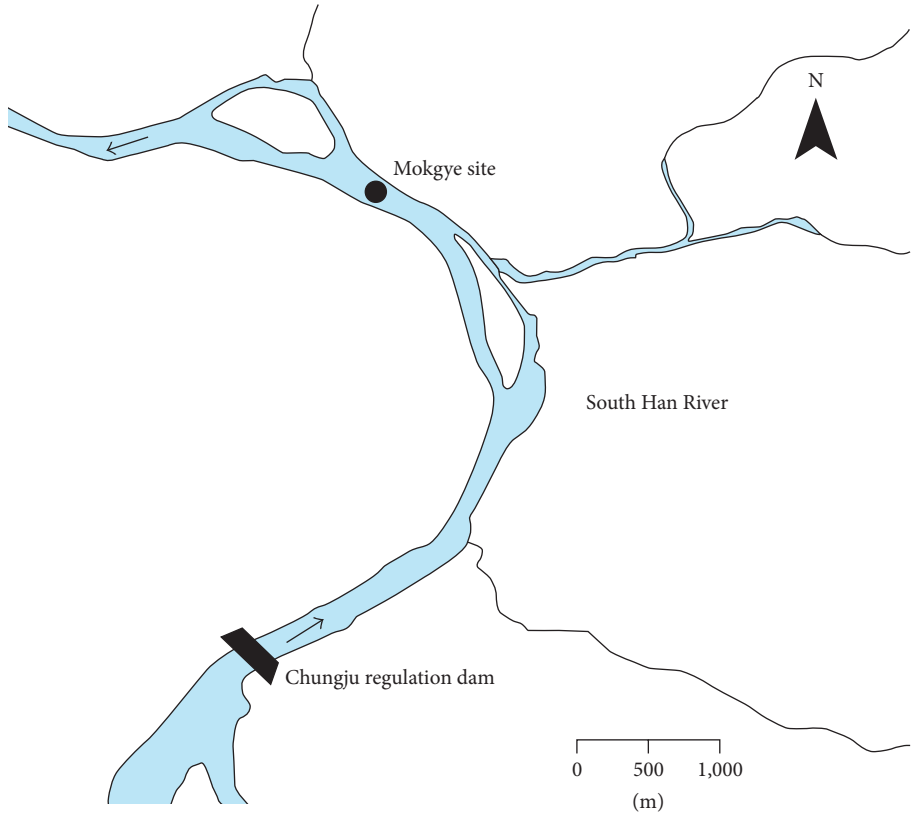

Figure 3: Study area (Mokgye, Korea).

3.2. Measurements under Normal and Flood Flow Conditions. In this study, field measurements for two events (event 1: May 18, 2012; event 2: June 28, 2011) were performed to assess discharge in normal and flood flow conditions. The measurements were repeated five and two times, respectively. Table 3 provides the actual observed water level and discharge at the Mokgye site, and the maximum water levels and discharges for events 1 and 2 are el. 52.87 m and el. 54.86 m and 127.63 m^3/s and 2,020.62 m^3/s, respectively.

Under flood flow conditions, the maximum flow speed reached 4 m/s, and the boat meandered along the path as its maximum speed was 2 m/s. Despite these unfavorable conditions, the remote-controlled boat measured flood discharge successfully, and the discharges were 1,771.13 m^3/s

Table 2: Mokgye site characteristics.

Site name		Mokgye	
Longitude	127-52-52	Latitude	37-04-34
River width (m)	330.00	Elevation (el. m)	52.337
Ann. avg. temperature (°C)	11.2	Bottom slope	300.00
Ann. max. temperature (°C)	17.7	Ann. avg. rainfall (mm)	1212.7
Ann. min. temperature (°C)	5.9	Ann. avg. rainfall duration (hr)	672.6
Ann. avg. evaporation (mm)	1043.9	Ann. avg. humidity (%)	71.9

Table 3: Time series of hydrologic events used in this study.

Event number 1 (normal flow condition)			Event number 2 (flood flow condition)		
May 18, 2012	Obs. flow (m^3/s)	Obs. HWL (el. m)	June 28, 2011	Obs. flow (m^3/s)	Obs. HWL (el. m)
12:00	127.63	52.87	16:30	1899.39	54.75
12:10	127.63	52.87	16:40	1998.44	54.84
12:20	127.63	52.87	16:50	1976.32	54.82
12:30	127.63	52.87	17:00	1976.32	54.82
12:40	127.63	52.87	17:10	1976.32	54.82
12:50	127.63	52.87	17:20	2020.62	54.86
13:00	127.63	52.87	17:30	1976.32	54.82
13:10	127.63	52.87	17:40	1954.27	54.80
13:20	127.63	52.87	17:50	1954.27	54.80
13:30	127.63	52.87	18:00	1943.26	54.79

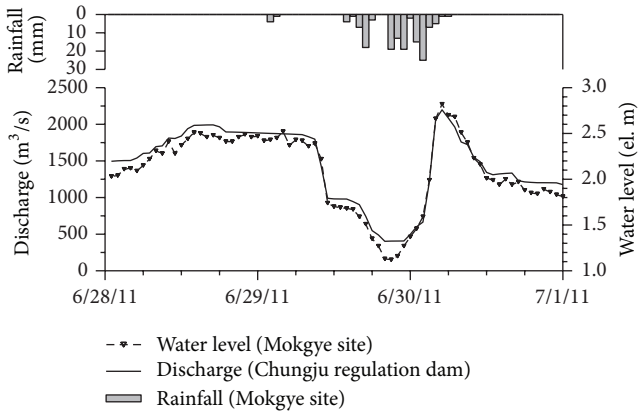

Figure 4: Discharge data from Chungju regulation dam and water levels at the Mokgye site.

and 1,545.01 m^3/s as shown in Table 4. Under normal flow conditions, the measured discharges were in the range of 122.92–129.83 m^3/s.

3.3. Analysis

3.3.1. Operational Challenge for the Measurements. The USGS provides guidelines to measure the average river sectional discharge by four consecutive measurements with the same water level condition in a moving boat [25]. However, for remote-controlled ADCP measurements there is an operational challenge for the flood discharge measurements. It is maintaining the boat track to match the desired cross section under fast flow conditions [28, 29]. The problem can be solved by adopting the DMG line by the east-north-up (ENU) coordinate velocity projections on the track line under normal flow conditions [28]. However, under flood flow conditions, the DMG heading of a moving boat cannot easily be fixed because the actual measured cross section changes constantly. Therefore, the DMG heading cannot be determined physically during the measurement. DMG heading is determined based on the postprocessed measured path from the data set. The RiverSurveyor Live program can only provide the starting edge and ending edge setup for the DMG calculations. However, in the moving boat method, particularly under flood flow conditions, the starting and ending points are not clear because the user cannot fix the cross section due to the reasons provided above. The boat movement changes continuously from a straight line because there is no sufficient amount of thrust to maintain a high-speed flow. The changing streamline does not match a straight DMG line that corresponds to the conventional tag line idea. The straight DMG line should be processed after the measurement to obtain the optimum DMG heading.

3.3.2. Evaluation and Modification. The differences between the first measurement and the rating for events 1 and 2 are presented in Table 5. Under flood flow conditions, the differences were 249.49 (12.35%) and 431.31 m^3/s (21.82%) for Cases 6 and 7, respectively. Under normal flow conditions, however, the differences were relatively very small in the 0.89–4.71 m^3/s (0.70–3.69%) range. Consequently, the measured discharges

Table 4: Discharge measurements in this study.

Number	Measurement Site	Period	Flow condition	Max. measured flow (m^3/s)
1	Mokgye	12:10~12:19 May 18, 2012	Normal	126.20
2		12:20~12:26 May 18, 2012	Normal	126.74
3		12:27~12:33 May 18, 2012	Normal	124.84
4		12:34~12:39 May 18, 2012	Normal	122.92
5		12:40~12:54 May 18, 2012	Normal	129.83
6		17:13~17:20 June 28, 2011	Flood	1771.13
7		17:21~17:29 June 28, 2011	Flood	1545.01

Table 5: Comparison of maximum measured and observed discharge.

Case	Flow condition	Max. measured discharge (m^3/s)	Max. observed discharge (m^3/s)	Difference (m^3/s)	Difference (%)
1	Normal	126.20	127.63	1.43	1.12
2	Normal	126.74	127.63	0.89	0.70
3	Normal	124.84	127.63	2.79	2.19
4	Normal	122.92	127.63	4.71	3.69
5	Normal	129.83	127.63	2.20	1.72
6	Flood	1771.13	2020.62	249.49	12.35
7	Flood	1545.01	1976.32	431.31	21.82

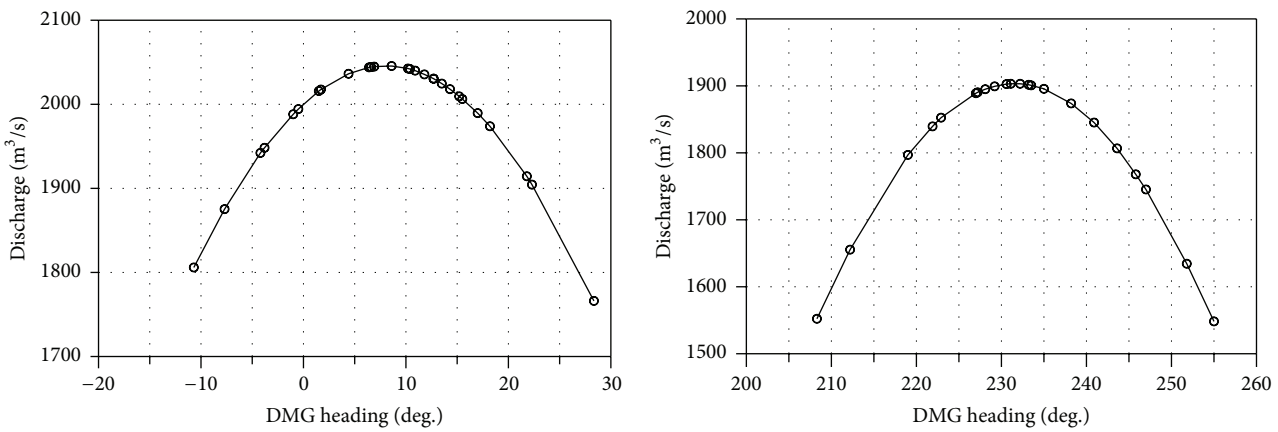

(a) Case 6 (b) Case 7

Figure 5: Discharge estimation using DMG heading modification.

under normal flow conditions were very close to observed (rating) discharge while there were relatively large differences under flood flow conditions.

As previously discussed, main source of errors is from the DMG heading judgment because the boat was allowed to drift downstream. So as to maintain the cross section alignment until the end point, the boat sailed to the upstream direction for some distance. To resolve this issue, the DMG line must be modified. In steady and straight flows, the cross section is simply the shortest path between the two banks. The flow streamline meets the cross section line perpendicularly, and the DMG line should be the cross section line. As unsteady and nonuniform flows occur frequently in meandering rivers, the cross section can be changed depending on the streamline changes, and therefore, the cross section line changes as the water level changes. Thus, the DMG line should be a line that produces the largest discharge under the possible cross sections because the flow vectors should remain perpendicular to the DMG line.

Following this assumption, the DMG headings of the data sets in flood flow cases were modified to find the maximum discharge via trial and error. For this, the repetition calculation is applied to get the maximum discharge by changing the DMG heading direction at discharge measuring section. The discharge is recalculated by changing arbitrarily the heading direction, and it is repeated until the maximum discharge is found. As a result, the maximum discharges for flood flow condition were calculated at 8.6 and 231.0 (deg.) of the heading direction, and therefore, these heading lines were chosen for the river cross section. Figure 5 illustrates the

Table 6: Discharge estimation results according to DMG heading modification.

Case	Flow condition	Max. measured discharge (m^3/s)	Max. observed discharge (m^3/s)	Modification	
				Max. discharge (m^3/s)	DMG heading (degree, °)
6	Flood	1771.13	2020.62	2045.58	8.6
7	Flood	1545.01	1976.32	1903.07	231.0

Table 7: Comparison of modified and observed discharges.

Case	Flow condition	Discharge (m^3/s)			Difference (m^3/s, %)			
		Measured	Modified	Observed	Measured and observed		Modified and observed	
6	Flood	1771.13	2045.58	2020.62	249.5	12.3%	24.9	1.2%
7	Flood	1545.01	1903.07	1976.32	431.3	21.8%	73.2	3.7%

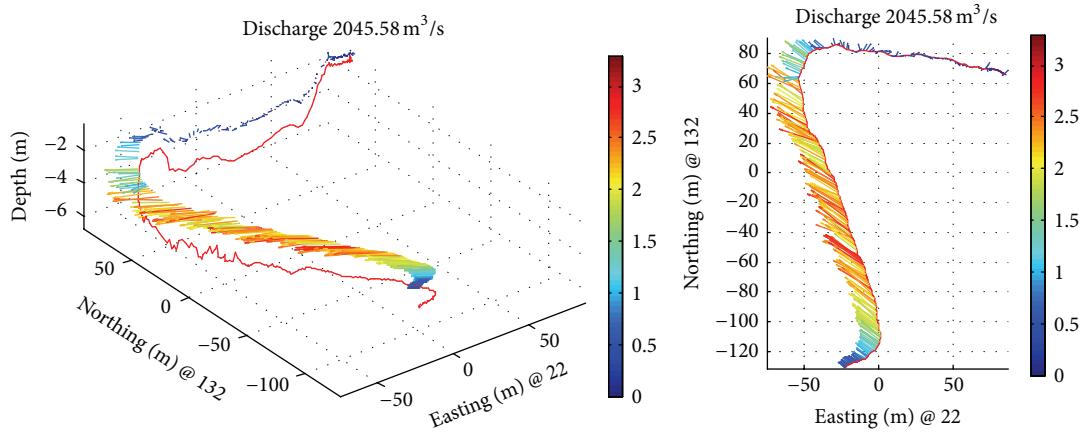

(a) Three-dimensional velocity profile (b) Two-dimensional velocity profile

Figure 6: Vertically averaged velocity profile and discharge (Case 6).

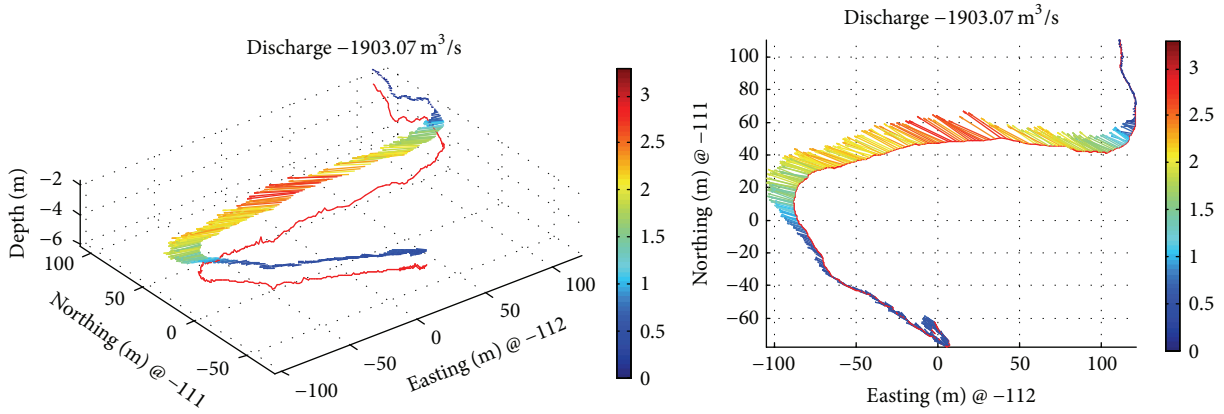

(a) Three-dimensional velocity profile (b) Two-dimensional velocity profile

Figure 7: Vertically averaged velocity profile and discharge (Case 7).

discharge modification using the DMG heading modification for Cases 6 and 7. As shown in Table 6, the modified discharges were estimated by setting the DMG heading to reflect the actual cross-sectional flow direction.

3.3.3. Results and Discussions. The modified discharge estimates according to the above aspects are shown in Table 7 and the differences are 24.9–73.2 m^3/s (1.2–3.7%). Table 7 demonstrated that the differences decrease by 11.1–18.1% in flood flow conditions. Figures 6 and 7 illustrate the final vertically averaged velocity profile with the final discharge for the river cross section of two cases. In Figures 6 and 7, the units of the x- and y-axes are transformed to display the position in universal transverse Mercator (UTM) coordinates, and the z-axis is the water depth. The red line is the river bed along the

boat's route, the black dotted line is the DMG line, and the color scale legends are the vertically averaged velocity in the flow direction.

4. Conclusion

In this study, the river velocity profiles and discharge under normal and flood flow conditions were measured by a remotely control boat with an ADCP and RTK GPS. The advantages of this technique include high productivity, fast measurements, operator safety, and high accuracy. However, there are concerns about controlling and operating a remote boat to achieve measurement goals, especially during extreme events such as floods. The raw estimates of discharge show more than a 10% difference compared with well-established rating tables. When performing river discharge measurements, the main error source has been identified as the boat path. Due to the rapid flow in a flood condition, the boat path is not regular and this can cause a measurement error of discharge. To resolve the differences, DMG heading modifications were established. The DMG heading modification uses a line that produces the largest discharge under the cross section where the flow vectors should remain perpendicular to the DMG line. As a result, the modified discharges are very close to the observed discharge in the flood flow conditions. With these modifications, a comprehensive discharge measurement with high accuracy is achieved.

Conflict of Interests

The authors declare that there is no conflict of interests regarding the publication of this paper.

Acknowledgment

This research was supported by a grant [MPSS-NH-2015-77] through the Natural Hazard Mitigation Research Group funded by Ministry of Public Safety and Security of Korean government.

References

[1] J. Lee, "Innovative approach to certify flood discharge amount in rivers," in *Proceedings of the 4th Hydrometry Symposium of Korea, Hydrological Survey Center*, pp. 80–86, 2010.

[2] C. J. Lee, W. Kim, C. Y. Kim, and D. G. Kim, "Velocity and discharge measurement using ADCP," *Journal of Korea Water Resources Association*, vol. 38, no. 10, pp. 811–824, 2005.

[3] S. E. Morlock, "Evaluation of acoustic Doppler current profiler measurements of river discharge," USGS Water Resources Investigations Report 95-4218, 1996.

[4] D. S. Mueller, "Field assessment of acoustic Doppler based discharge measurements," in *Proceedings of the ASCE-IAHR Joint Conference on Hydraulic Measurements & Experimental Methods*, Estes Park, Colo, USA, July-August 2002.

[5] K. Oberg, "In search of easy-to-use methods for calibrating ADCP's for velocity and discharge measurements," in *Proceedings of the ASCE-IAHR Joint Conference on Hydraulic Measurements & Experimental Methods*, Estes Park, Colo, USA, July-August 2002.

[6] J. W. Gartner and N. K. Ganju, "A preliminary evaluation of near-transducer velocities collected with low-blank acoustic Doppler current profiler," in *Proceedings of the Hydraulic Measurements and Experimental Methods, ASCE-IAHR Joint Conference*, Estes Park, Colo, USA, August 2002.

[7] J. A. González-Castro, M. Ansar, and O. Kellman, "Comparison of discharge estimates from ADCP transect data with estimates from fixed ADCP mean velocity data," in *Proceedings of the ASCE-IAHR Joint Conference on Hydraulic Measurements & Experimental Methods*, pp. 1–10, Reston, Va, USA, July-August 2002.

[8] M. Adler and U. Nicodemus, "A new computer model for the evaluation of data from acoustic doppler current profilers (ADCP)," *Physics and Chemistry of the Earth, Part C: Solar, Terrestrial & Planetary Science*, vol. 26, no. 10–12, pp. 711–715, 2001.

[9] M. Muste, K. Yu, and M. Spasojevic, "Practical aspects of ADCP data use for quantification of mean river flow characteristics; part I: moving-vessel measurements," *Flow Measurement and Instrumentation*, vol. 15, no. 1, pp. 1–16, 2004.

[10] M. Muste, K. Yu, T. Pratt, and D. Abraham, "Practical aspects of ADCP data use for quantification of mean river flow characteristics; part II: fixed-vessel measurements," *Flow Measurement and Instrumentation*, vol. 15, no. 1, pp. 17–28, 2004.

[11] C. D. Rennie, R. G. Millar, and M. A. Church, "Measurement of bed load velocity using an acoustic Doppler current profiler," *Journal of Hydraulic Engineering*, vol. 128, no. 5, pp. 473–483, 2002.

[12] R. R. Holmes Jr. and M. H. Garcia, "Velocity and sediment concentration measurements over bedforms in sand-bed rivers," in *Proceedings of the Hydraulic Measurements and Experimental Methods, ASCE-IAHR Joint Conference*, Estes Park, Colo, USA, August 2002.

[13] E. A. Nystrom and W. Gary, "ADCP measurement of suspended sediment in the tidal Hudson River," in *Peoceedings of the USGS Surface Water Conference*, New York, NY, USA, 2003.

[14] D. R. Parsons, P. R. Jackson, J. A. Czuba et al., "Velocity Mapping Toolbox (VMT): a processing and visualization suite for moving-vessel ADCP measurements," *Earth Surface Processes and Landforms*, vol. 38, no. 11, pp. 1244–1260, 2013.

[15] J. L. Best, R. A. Kostaschuk, J. Peakall, P. V. Villard, and M. Franklin, "Whole flow field dynamics and velocity pulsing within natural sediment-laden underflows," *Geology*, vol. 33, no. 10, pp. 765–768, 2005.

[16] D. R. Parsons, J. L. Best, O. Orfeo, R. J. Hardy, R. A. Kostaschuk, and S. N. Lane, "Morphology and flow fields of three-dimensional dunes, Rio Paraná, Argentina: results from simultaneous multibeam echo sounding and acoustic Doppler current profiling," *Journal of Geophysical Research: Earth Surface*, vol. 110, no. 4, 2005.

[17] C. M. García, K. Oberg, and M. H. García, "ADCP measurements of gravity currents in the Chicago River, Illinois," *Journal of Hydraulic Engineering*, vol. 133, no. 12, pp. 1356–1366, 2007.

[18] J. R. French, H. Burningham, and T. Benson, "Tidal and meteorological forcing of suspended sediment flux in a muddy mesotidal estuary," *Estuaries and Coasts*, vol. 31, no. 5, pp. 843–859, 2008.

[19] P. R. Jackson, C. M. García, K. A. Oberg, K. K. Johnson, and M. H. García, "Density currents in the Chicago River: characterization, effects on water quality, and potential sources," *Science of the Total Environment*, vol. 401, no. 1–3, pp. 130–143, 2008.

[20] S. N. Lane, D. R. Parsons, J. L. Best, O. Orfeo, R. A. Kostaschuk, and R. J. Hardy, "Causes of rapid mixing at a junction of two large rivers: Rio Paraná and Rio Paraguay Argentina," *Journal of Geophysical Research*, vol. 113, no. 2, 2008.

[21] A. Bartholomä, A. Kubicki, T. H. Badewien, and B. W. Flemming, "Suspended sediment transport in the German Wadden Sea-seasonal variations and extreme events," *Ocean Dynamics*, vol. 59, no. 2, pp. 213–225, 2009.

[22] R. A. Kostaschuk, D. Shugar, J. L. Best et al., "Suspended sediment transport and deposition over a dune: Rio Parana, Argentina," *Earth Surface Processes and Landforms*, vol. 34, no. 12, pp. 1605–1611, 2009.

[23] D. H. Shugar, R. Kostaschuk, J. L. Best et al., "On the relationship between flow and suspended sediment transport over the crest of a sand dune, Río Paraná, Argentina," *Sedimentology*, vol. 57, no. 1, pp. 252–272, 2010.

[24] S. A. Wright and M. Kaplinski, "Flow structures and sandbar dynamics in a canyon river during a controlled flood, Colorado River, Arizona," *Journal of Geophysical Research*, vol. 116, no. 1, 2011.

[25] M. R. Simpson, "Discharge measurements using a broad-band acoustic Doppler current profiler," Open-File Report 01-1, USGS, 2001.

[26] R. L. Gordon, "Acoustic measurement of river discharge," *Journal of Hydraulic Engineering*, vol. 115, no. 7, pp. 925–936, 1989.

[27] RD Instrument, *WinRiver User's Guide International Version*, RD Instrument, San Diego, Calif, USA, 2003.

[28] J. Lee and J. Kim, "Keeping discharge measurement accuracy of the moving boat method compared with the tagline method," in *Proceedings of the 5th Hydrometry Symposium of Korea Proceeding*, pp. 225–230, Hydrological Survey Center, 2011.

[29] N. Everard, *ADCP v Current Meter. Comparison of Gauged Flows*, Environment Agency, 2011.